ADVANCED ANALYSIS AND DESIGN OF POLYMER SHEET EXTRUSION

A Dissertation presented to
the Faculty of the Graduate School
University of Missouri - Columbia

In Partial Fulfillment
of the Requirements for the Degree

Doctor of Philosophy

---

by
QI WANG

Dr. Douglas E. Smith, Dissertation Supervisor

DECEMBER 2007

The undersigned, appointed by the Dean of the Graduate School, have examined the dissertation entitled

ADVANCED ANALYSIS AND DESIGN OF POLYMER SHEET EXTRUSION

Presented by Qi Wang, a candidate for the degree of Doctor of Philosophy, and hereby certify that in their opinion it is worthy of acceptance.

_____
Dr. Douglas E. Smith

_____
Dr. Sunggyu "KB" Lee

_____
Dr. P. Frank Pai

_____
Dr. Yuyi Lin

_____
Dr. Yuwen Zhang

To my mother Peng Rumin and my dear family

ACKNOWLEDGEMENTS

This thesis is the successful end of my long journey in obtaining my PhD degree in Mechanical Engineering. Fortunately I have not travelled in a vacuum in this journey. There are many people who made this journey easier with words of encouragement and more intellectually challenging by offering different kinds of help to expand my knowledge and research ideas.

First, I am deeply indebted to my advisor, Dr. Douglas E. Smith whose constant help, stimulating suggestions and constant encouragement helped me in all phases of my research and thesis writing. I have been involved in Dr. Smith's project since 2001 when I started my Master program at Colorado School of Mines. During all these years, I have known Dr. Smith as the most admirable and respectful person. His enthusiasm and integral view on research and his mission for providing only high-quality work have made a deep impression on me. I owe him lots of gratitude for having shown me this way of research. I am really glad that I have come to know him in my life.

I would like to thank my thesis committee members Dr. Sunggyu "KB" Lee, Dr. Yuyi Lin, Dr. P. Frank Pai and Dr. Yuwen Zhang for their suggestions and constructive criticisms. I would also like to express my sincere appreciation for my committee members for monitoring my work and taking effort in reading and providing me with valuable comments on my thesis. A special thanks goes to Dr. Sunggyu "KB" Lee for his responsive and warmhearted help even after he moved out of the Columbia campus.

I wish to acknowledge National Science Foundation for its financial support (grant number DMI-0094011 and DMI-0327732) for this research. The funding makes this research possible. Additionally, I am thankful to my work partner, and friend, David Jack, whom I have known for more than five years and who has always been a kind, most helpful and trustful friend. His friendship helped me survive through many hard

times and made this journey a memorable experience. I was lucky to have such a good friend and partner at work. I also wish to thank Dr. Gary L. Solbrekken for his help in my studies of fluid flow analysis.

Finally I would like to express my deepest gratitude to my mother and family. They have been a constant source of love, understanding and support for me. I am indebted to my father, ZhiYuan Wang, for his care and love. As a typical father in a Chinese family, he worked industriously to support the family and spared no effort to provide the best possible environment for me to grow up and attend school. He had never complained in spite of all the hardships in his life. Although he is no longer with us, he is forever remembered. I cannot ask for more from my mother, Peng RuMin, as she is simply perfect. I have no suitable word that can fully describe her everlasting love to me. Mother, I love you. It is you and our family who accompanied me throughout this endeavor.

Again, this thesis would have been simply impossible without all of those who love and care about me.

Qi Wang

Columbia, Missouri

September 25, 2007

TABLE OF CONTENTS

LIST OF TABLES

LIST OF FIGURES

ix

ADVANCED ANALYSIS AND DESIGN OF POLYMER SHEET EXTRUSION

Qi Wang

Dr. Douglas E. Smith, Dissertation Supervisor

ABSTRACT

A manufacturing process design methodology is presented which can be used to improve the production of polymer components manufactured via the extrusion. The design methodology employs polymer process modeling, design sensitivity analysis, and numerical optimization. Specifically, this research investigates the optimization-based design methodology of polymer extrusion including the analysis of Generalized Newtonian Fluid (GNF) models, the adjustable features of die designs under multiple operating conditions, fluid-structure interaction, and non-isothermal analysis for fully-coupled nonlinear steady-state temperature and pressure systems. The main objective of this research is to develop the design methodologies of polymer extrusion and their applicability in efficiently modeling and simulating polymer processing and industrial die designs.

An example of industrial extrusion die and various polymers (LDPE, PP, LLDPE) are provided to exemplify the polymer processing design methodology. From the result of this research, it is shown that the proposed methodologies can be effectively used to design polymer extrusion dies in which the die cavity geometry is computed to minimize the pressure drop while delivering a uniform exit velocity and a uniform temperature.

CHAPTER 1

INTRODUCTION

1.1 Motivation

Polymer extrusion has been widely embraced in industry as a useful manufacturing method for converting polymeric raw materials into finished products. In this process, the molten stream of polymer flowing through dies or into cold molds is cooled to form the solid-product shape. The field of polymer processing has been traditionally and consistently analyzed in terms of the prevailing processing methods, that is, extrusion, injection molding, blow molding, calendering, mixing and dispersion, rotational molding, and so on. Among them, extrusion is the most popular tool since a vast array of thermoplastics are processed by means of extrusion. In the process of extrusion, a polymer melt is pushed through the die that continuously shapes the melt into a desired form. This process renders the die design to be of high importance.

A well-designed extrusion die can deliver a polymer melt through the die uniformly. However, it is difficult to design and optimize the die shapes due to the complexity of flow distributions with regard to die geometry, temperature, shear history, and viscoelastic effects. Traditional design methods of extrusion dies are based on experimental trial-and-error procedures, relying essentially on the designer experience and usually being very time, material and equipment consuming [1,2]. Thanks to the development of software packages for the mathematical modeling of the flow of polymer melts, this trial-and-error procedure is being progressively transformed from

an empirical to a numerical based operation.

To design extrusion dies with a numerical based methodology, an appropriate simulation method is required for polymer melt flow analysis. Both non-Newtonian and shear-thinning properties of polymer melts in particular, as well as the non-isothermal nature of the flow, significantly affect the melt extrusion process. Moreover, the non-Newtonian and non-isothermal effects interact and reinforce each other [3]. Thus it is important to choose a flow model which accurately predicts the flow condition during the polymer extrusion process.

The applications of the finite element method along with an optimization algorithm have been used to design polymer extrusion dies [4–7]. In these approaches, numerical simulations are used to analyze isothermal flow of polymer melts, and optimization is used to compute the die cavity geometry capable of giving a near-uniform exit velocity. Once design variables and performance measures are defined, the minimum of the cost function may be determined through optimization algorithm to systematically search for the optimal design parameters. Additionally, design sensitivity is calculated to quantify the relationships between the design variables and performance measures [5–7]. Sensitivity analysis and optimization bring a new look at design problem and can lead to more realistic and accurate results. Application of these numerical techniques to die design are possible, even though rheological behavior of polymer melt complicates the calculation. In this research, the design optimization problem is solved by combining polymer process modeling, numerical optimization, and design sensitivity analysis. Simulations that are employed in the optimization

2

design process are based on the generalized Hele-Shaw flow model to provide a means for including die cavity geometries with arbitrary in-plane features.

Most sheet extrusion dies include adjustable features such as a choker bar or flexible lips to improve the quality of the final product by altering the melt flow within the die cavity, especially when variability (e.g., temperature or material properties) in operating conditions is encountered. Furthermore, the extrusion of very viscous polymers at high flow rate through dies with thin internal flow channels can result in high internal pressures. As a result, high pressures acting on the surfaces of the channel may significantly distort the die body. The distortion of the die body can have a significant effect on the flow distribution in the die and the melt velocity over the die exit. The die designs that neglect die body deformation, therefore, may not perform as desired.

Polymer melt temperature variation in extrusion dies can, in principle, be important, through its influence on viscosity, and hence on pressure drop and flow distribution [8]. This research attempts to provide an efficient method to analyze the melt flow heat transfer problem. The finite element simulation of the coupled pressure and temperature problem is developed based on Hele-shaw flow approximation and energy equation. The resulting computer simulations can provide detailed temperature fields of polymer melt in the die cavity, which may help the engineer with the design process and gain a better understanding of the thermal effect of polymer melt.

1.2   Background Overview

The analysis and design of the polymer extrusion process used to produce thin sheets and films have received much attention over the last few decades. While significant advances have been made, complex constitutive relations and demanding performance criteria continue to present a challenge to the successful design and operation of a sheeting die. Of particular interest is the design of a die cavity geometry having a minimum inlet pressure while delivering a thin layer of polymer melt with a uniform velocity over the entire width of the die exit.

A proper design of an extrusion die is of critical importance to ensure the manufacture of high-quality products. There have been many technical articles dealing with the design and operation of various extrusion dies. Among them, the most widely used designs are those of the coat-hanger die, T-type die and fishtail die [9–14]. The common idea behind these efforts is to design a die which can deliver uniform polymer melt flow at the die exit. In these approaches, dies with uniform exit velocity distributions are obtained, however, pressure drop is not considered. In addition, the ability of the die to accommodate variations in material properties is not considered.

Flow characteristics for traditional dies have been approximated using closed-form, one-dimensional flow analysis [14]. The approaches are based on one-dimensional or two-dimensional lubrication approximation [12], i.e. the mass and momentum conservation equations are employed to obtain average flow rates inside the die. The

work by Wang [15] presented a three-dimensional method for flow distribution in coat-hanger dies where the velocity and pressure fields could be completely determined. Huang et al. [16] concentrated on a comprehensive analysis of polymer melt flow in a coat-hanger die by means of three-dimensional (3D) computational fluid dynamics (CFD) techniques, they then compared the results with the analytical design method and concluded that the expense of running a full 3D analysis is not justified when compared to the simple analytical method. Indeed, the three-dimensional method is more realistic than two-dimensional lubrication approach, but it requires significant computational effort, and requires a trial-and-error procedure to select a proper die geometry. Wen and Liu [17] extended these approaches by combining one and two-dimensional lubrication approximation, and three-dimensional simulation so that the detailed flow field inside the extrusion dies can be determined and the overall flow uniformity can be adjusted to a satisfactory level.

In the design of extrusion dies, flow material properties are also considered. Pan and Wu [13] tried to make die design available to slowly reacting materials, they used the conventional lubrication approximation on die design to simulate the motion of slowly reacting materials in the die. But this research is still held at the stage of one-dimensional lubrication approximation analysis on die design. Lo [18] developed an efficient method for the design of streamlined extrusion dies based on the prescribed strain rate variation, Lo considered strain rate variation as an important factor to extrusion process when materials flow through the die, however, this work was limited to providing a prediction of die shape, it did not resolve die design problems.

Most of the previous work in die design has employed power-law fluid model or Newtonian fluid model for its simplicity [9,11,12,18]. Although the power-law model is well-known and widely used in engineering work, it does not always provide accurate computation of viscosity, particularly when shear rates are low. Other researchers have used Cross model to simulate extrusion flow [19, 20]. Liu et al. [12] reviewed die design methods for Newtonian and power-law fluids and extend die design to accommodate the Ellis and modified Bingham fluid models. The resulting closed-form die design equations provide a computationally efficient approach for defining sheeting die cavity geometries, but assume a constant wall shear rate and are limited to a finite set of geometric configurations. In addition, the generalized Hele-Shaw approximation model is commonly applied to the compression and injection molding process [9, 21], and this model is also widely used in the extrusion die designs to represent the fluid flow [17, 22].

The flow of polymer melt in sheeting dies has also been simulated using three-dimensional flow equations and numerical approaches such as the finite element method to solve for the pressure, velocities, and temperatures in the polymer melt [23–25]. Various Generalized Newtonian Fluid (GNF) models (see e.g., Tadmor and Gogos [3] or Bird, et al., [26]) have been included in these simulations which have been shown to compare well with experimental results by Dooley [23]. These simulations have assumed isothermal flow, which is justified in part by the work of Pittman and Sander [8]. Also considered are coextrusion [24], wall slip [25], and die swell [27].

6

A three-dimensional temperature formulation, combined with the generalized Hele-Shaw flow model has been used by Arpin et al. [28], and provided temperature profiles across the slit gap. Simplifying assumptions such as constant temperature and unidirectional fully-developed flow that serve as a basis for the one-dimensional techniques described above are avoided. Instead, a complete description of the melt flow is obtained for arbitrary die cavity geometries that are not restricted to simple T, fish-tail, or coat-hanger shapes.

Sensitivity analysis and optimization have brought opportunity for the development of new approaches for extrusion die design. Traditional design methods focus on the optimal design of die shape, and computation of design parameters [29]. To employ mathematical programming methods in design problems, one needs to calculate the design sensitivities or the performance measures with respect to design variables [22, 30]. Maniatty and Chen [31] determined the sensitivity of the process power requirement and of the internal state variable to the process geometry, and applied numerical algorithm for computing shape sensitivity parameters in steady-state metal forming process. Mihelič and Štok [32] used the Lagrange incremental elastic-plastic finite element formulation in modeling the material flow and considered the optimization approach in an extrusion process. Ulysse [30] used analytical sensitivities and a mathematical programming technique to determine optimal bearing length to achieve a uniform die exit flow. He also included temperature predictions and introduced thermal effects in the analytical sensitivity formulations. Other approaches solve optimization problems to generate die cavities which produce a desired

net shape including the effect of die swell [33].

Smith [22] presented a general numerical approach for the sensitivity analysis of non-linear steady-state systems, and approximated flow model for a generalized Hele-Shaw flow. Other researchers presented the problems of die shape design through the use of sensitivity field calculation [29]. These problems are posed as an optimization problem with respect to a finite number of algebraic design parameters [29]. Design parameters in these approaches included inlet gate location, part wall thickness, cooling channel location, and other process related parameters such as melt temperature, mold temperature, and cooling channel temperature. For example, the work by Zhao and Wright [34] used cubic spline curves to represent the shape of two-dimensional dies. The control points or coefficients were considered as design variables.

The finite difference method is perhaps the simplest approach to evaluate design sensitivity analysis [35]. It may, however, suffer from round-off and truncation errors. Alternatively, numerically efficient and accurate ways to compute sensitivity derivatives include the direct differentiation method and adjoint variable method [22, 29, 30, 34].

Recently, numerical optimization methods have been combined with three-dimensional melt flow simulations which provide a powerful technique for designing die cavities [2, 36]. Na and Lee [37] applied optimization solution of the inverse formulation, in conjunction with a 3D flow simulation using the finite element method, to achieve optimum geometry design of coat-hanger dies. Application of design response analysis combined with a zero-order optimization algorithm to coat-hanger

die design was also performed by Wang [38]. This type of design methodology allows for a more general definition of the die cavity and may include other important performance metrics such as die pressure drop. Unfortunately, the computational effort required to obtain the more accurate three-dimensional solutions can be excessive when used in an iterative design procedure, particularly when applied to detailed industrial designs.

Two-dimensional (often referred to as $2\frac{1}{2}$ D) simulations provide a computationally efficient alternative to three-dimensional methods while avoiding many of the simplifying assumptions and geometric restrictions of existing one-dimensional design equations (see e.g., [17, 22, 39–41]). Sartor [39] was perhaps the first to combine numerical optimization with a two-dimensional flow network analysis to iteratively solve the die design problem using a power-law fluid model. Smith, et al., [22, 40, 41] developed a finite element simulation based on the Hele-Shaw flow approximation [21] similar to that used in injection molding simulations [42] to compute optimal die cavity geometries. Constraints were defined to measure the die's exit velocity variation and design sensitivity expressions were developed which greatly reduce the computational effort required in the design optimization calculations. Unfortunately, these designs were also limited to isothermal Newtonian and power-law fluids. Non-isothermal flows in coat-hanger dies have been investigated in some studies [28, 43, 44]. Sander and Pittman [45] and Gifford [46] also performed die body deflection analysis coupled with the melt flow analysis.

In the field of optimization for die design, most approaches only address a single

material or one operating condition. Since extrusion dies are very expensive to build, it will be more economical to construct dies that process multiple materials or operating conditions. Smith [41] is the first to apply the optimal die design to multiple operating conditions where die geometries that apply to multiple materials are computed simultaneously. In addition, Smith and Wang [5] recently extended the earlier optimization approaches to include various generalized Newtonian fluid models including the Carreau-Yasuda fluid model, and they addressed variability in die design by including an adjustable choker bar in the melt flow analysis and design [6]. In both of their articles, constraint functions were defined to measure the die's exit velocity variation, and design sensitivity expressions were developed that greatly reduced the computational effort required in the design optimization calculation.

Polymer sheeting die design methodologies are presented in this research which integrates finite element flow simulations, numerical optimization, and design sensitivity analysis to compute die cavity geometries capable of meeting various demanding performance criteria. The main objective of this research is to develop the design methodologies of polymer extrusion and their applicability in efficiently modeling and simulating polymer processing and die designs.

1.3   Research Objective

This research is intended to enhance polymer processing analysis by incorporating it into a design methodology based on numerical analysis, optimization, and design sensitivity analysis. The principal objectives of this thesis are to formulate

efficient and accurate design sensitivity analysis methods for polymer processing, to develop polymer processing analysis methods that best facilitate the sensitivity analysis methodology, and to combine these analyses with nonlinear programming to optimize the polymer processes. More specifically, this research investigates the optimization-based design methodology of polymer extrusion including the analysis of Generalized Newtonian Fluid (GNF) models, the adjustable features of die designs under multiple operating conditions, fluid-structure interaction, and coupled Hele-Shaw approximation and energy equation for non-isothermal analysis.

To realize these objectives, polymer melt flow computations and design sensitivity analyses are performed using the generalized Hele-Shaw flow approximation with power-law, Carreau-Yasuda, Cross, Ellis, and Bingham fluid models. The effect of the adjustable features of die cavity is incorporated in the design approach to improve the quality of the final product. The coupling effects between polymer melt fluid analysis and 3D finite element simulation for die structure are incorporated into the die design optimization to compute the optimal die cavity geometry. Additionally, temperature dependent constitutive fluid models are considered in this research to make die designs more realistic. Non-isothermal purely-viscous fluids through thin, slowly-varying thickness cavities are analyzed in which the lubrication approximation may be applied. The non-isothermal condition coupled with Hele-Shaw flow approximation is also incorporated in the design methodology by solving incompressible and steady-state energy equations. Industrial relevant examples will be presented to demonstrate the effectiveness of the proposed methodologies.

The research fulfilling these goals is presented in the next four chapters. In each chapter, analysis and design sensitivity analysis methods for polymer processes are presented followed by example optimizations of particular processes.

In chapter 2, the generalized Hele-Shaw flow approximation and various generalized Newtonian fluid models are described where numerical methods such as the finite element method and Newton-Raphson method are used to calculate the pressure solution, flow viscosity, and flow conductance. The design methodology given in this chapter is applied to polymer sheeting die design and addresses the need for developing dies capable of performing well under multiple operating conditions. The adjustable features of the die cavity can be modified in an optimal manner consistent with the overall design objectives [4–6].

Chapter 3 presents an optimization-based design methodology that integrates a simulation of the polymer melt flow and extrusion die cavity deformation to compute a die cavity geometry capable of giving a near-uniform exit flow rate. In this approach, the flow analysis, which is simplified with the Hele-Shaw approximation, is coupled to a 3D finite element structural simulation for the die deformation. In addition, shape optimization of a polymer sheeting die is performed by the incorporation of the coupled analyses in our constrained optimization algorithm [7, 47, 48].

The final technical developments appear in chapter 4 where the non-isothermal flow analysis is investigated by incorporating the fully-coupled system equations, both 2.5D Hele-Shaw approximation and 3D energy equation, into the design sensitivity analysis for polymer process optimization. To reflect the non-isothermal influence on

the rheological behavior of polymer melt, the temperature-shifting function [44] is introduced to represent the polymer melt viscosity equation. A coupled computational algorithm to determine the temperature filed of polymer melt in the die cavity is presented which uses the pressure and velocity fields from the the Hele-Shaw fluid flow analysis. The SUPG finite element method [49] and the adjoint method [50] are developed in a manner which facilitates design sensitivity analysis. The design sensitivity analysis is particularized for this fully-coupled system where detailed derivations are given to illustrate the computational procedures.

Finally, conclusions and recommendations are made in chapter 5. The major accomplishments of this thesis are summarized, and future research to enhance the current design methodology is proposed.

CHAPTER 2

OPTIMAL DESIGN OF DIES WITH ADJUSTABLE FEATURES

It is common for materials processing operations to have adjustable features that may be used to improve the quality of the final product when variability in operating conditions is encountered. This chapter considers the polymer sheeting die design problem where variability in operating temperature or material properties, for example, requires that the die be designed to perform well under multiple operating conditions. An optimization procedure is presented where the design variables parametrize both stationary and adjustable model variables. In this approach, adjustable features of the die cavity are modified in an optimal manner consistent with the overall design objectives. The computational design approach incorporates finite element simulations based on the Generalized Hele-Shaw approximation to evaluate the die's performance measures, and includes a gradient-based optimization algorithm and analytical design sensitivities to update the die's geometry. Examples are provided to illustrate the design methodology where die cavities are designed to accommodate multiple materials, multiple flow rates, and various temperatures. This research demonstrates that improved tooling designs may be computed with an optimization-based process design approach that incorporates the effect of adjustable features.

2.1   Background

Polymer extrusion is an important manufacturing process used to produce a vast array of commercial plastic products. For example, flat polymer sheets, plastic tubes, window channels, and other complex shapes of fixed cross section are produced by this continuous forming process. A primary objective in the design of a polymer extrusion die is to determine the optimal flow channel geometry that forms a desired cross section from a continuous molten polymer stream. To ensure that the desired cross section is obtained, sheeting dies are designed to deliver a uniform flow rate across the die exit. Most sheet extrusion dies include adjustable features such as a choker bar or flexible die lips which provide a means to accommodate process variations by altering the melt flow within the die cavity. Analysis and numerical simulations have been performed to evaluate the melt flow within a sheeting die, and design methods have been employed to compute optimal die cavity geometries. Unfortunately, a die design method that anticipates the use of adjustable features when computing the optimal die cavity geometry has received little attention.

While applicable to a single operating condition, the previous die design approaches do not consider the possibility of variations that may occur during the polymer extrusion process. Deviations in temperature or humidity during the manufacturing process, for example, may alter the flow characteristics in the die which can cause undesirable results in the final product. Similar effects are seen due to variations in the incoming polymer materials. Since it is not practical to build an individual sheeting die for each production variation, adjustable features such as choker bars and

adjustable die lips are included in sheeting dies to better accommodate changes in the melt properties (see e.g., Michaeli [14]). Wu et al. [51] provided design equations based on one-dimensional flow to prescribe various choker bar shapes for a single die cavity, and Bates et al. [52] optimized restrictor geometries for single operating conditions. Otherwise, little effort has been made to incorporate the effect of the adjustable features when designing sheeting dies under multiple operating conditions.

This research presents a simulation-based optimal design approach similar to that given by Smith et al. [22]. In this study, however, the objective is to determine a single sheeting die cavity geometry that will best accommodate multiple operating conditions that may exist due to variations in temperature, material, and/or flow rate. To realize this objective, a simulation-based approach is presented below that incorporates nonlinear finite element analysis which models the non-Newtonian flow of polymer melt within an extrusion die cavity. The method uses numerical optimization where design sensitivities are evaluated with the adjoint variable method.

2.2   Polymer Sheeting Die Design Approach

As in other manufacturing processes, polymer extrusion dies are designed such that adjustments can be made during their operation to improve the quality of the final product. A sheet extrusion die cavity typically consists of a region where the geometry is fixed once the die is machined, as illustrated in figure 2.1. In addition, there is a region or regions in the die that can be adjusted by the operator to accommodate variability during production. A choker bar and/or flexible die lips are used to provide

a means to adjust the flow of polymer melt as required to maintain a uniform exit flow rate for the sheet being produced.
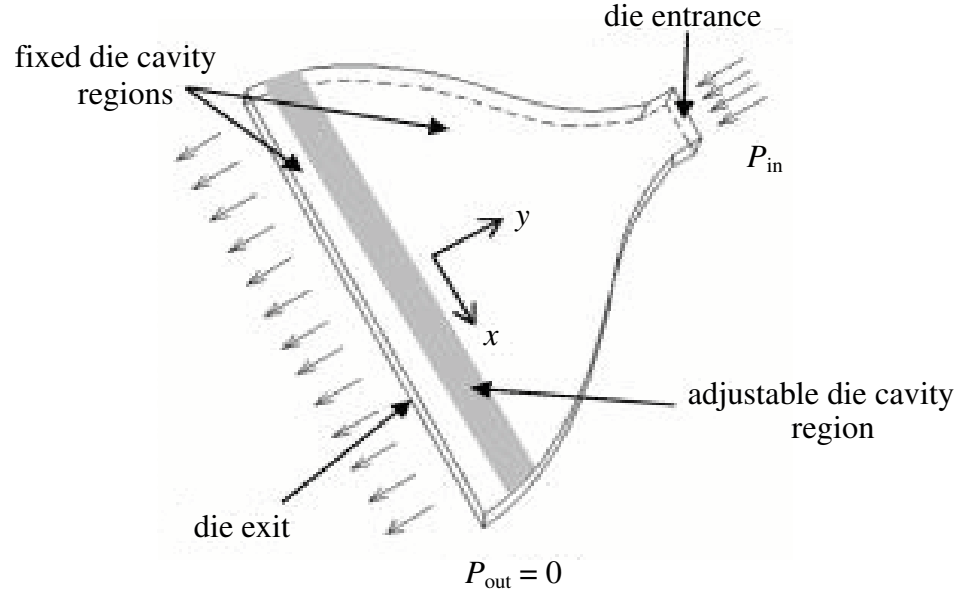
Figure 2.1: Coat hanger die geometry with fixed and adjustable (i.e., choker bar) regions

This chapter considers an optimization-based approach to design polymer extrusion dies where the die cavity geometry is computed to give improved performance. In this approach, two types of model variables are employed in the die geometry parametrization, both of which are defined by design variables in the optimization problem:

- Stationary model variables: These variables define the geometry of an extrusion die that is fixed once the die is machined. It is assumed that these model variables, and the corresponding die geometry, cannot be adjusted to accommodate manufacturing variability. In the die design example, stationary model

variables describe the fixed die cavity regions in figure 2.1.

- Adjustable model variables: These variables define regions in the die or machine settings that can be adjusted during production by an operator or, perhaps, an automatic control device, to improve the quality of the final product. It is assumed that these design variables are adjusted in an optimal manner to accommodate manufacturing variability. In the die design example, adjustable variables describe the choker bar settings and inlet pressure for each flow condition as shown in figure 2.1.

The design approach described below is developed to compute a die cavity geometry for a single polymer sheeting die, given that there is a region of the die that can be adjusted to accommodate variability during production. An optimization problem is defined consisting of an objective function and constraints that are based on multiple isothermal melt flow simulations in terms of the design variable vector $\boldsymbol{\phi}$ as

$$
\begin{array}{ll}
\text{Determine} & \boldsymbol{\phi} \\[2mm]
\text{To minimize} & f(\boldsymbol{\phi}) = \sum_{q=1}^{N_f} P_{in}^q \\[2mm]
\text{Subject to} & g_1^q(\boldsymbol{\phi}) = \frac{1}{L} \int_{l_{exit}} \left(\frac{\bar{v}^q(\boldsymbol{\phi})}{v_a^q(\boldsymbol{\phi})} - 1 \right)^2 dx \le \varepsilon_1^q \\[3mm]
& g_2^q(\boldsymbol{\phi}) = \left(\frac{v_a^q(\boldsymbol{\phi})}{v_p^q} - 1 \right)^2 \le \varepsilon_2^q \\[3mm]
& \phi_i^L \le \phi_i \le \phi_i^U
\end{array}
\tag{2.1}
$$

The non-linear constrained optimization is to minimize the sum of the inlet pressures P_{in}^q, $q = 1, 2 \ldots N_f$ where N_f is the number of operating or flow conditions considered in the design problem. This cost function represents the sum of the pressure drops through the die (cf. figure 2.1) since P_{out} is fixed at 0 for each flow condition. The constraint functions g_1^q and g_2^q, $q = 1, 2 \ldots N_f$, are, respectively, a measure of the exit velocity variation and die flow rate for the qth flow conditions. In the above, $\bar{v}^q$ is the y component of the gap-wise average velocity (see figure 2.1) and v_a^q is the qth average exit velocity computed from

$$v_a^q(\boldsymbol{\phi}) = \frac{1}{L} \int_{l_{exit}} \bar{v}^q(\boldsymbol{\phi}) \, dx \tag{2.2}$$

A zero value of g_1^q indicates that the computed exit velocity $\bar{v}^q(\boldsymbol{\phi})$ equals the qth average exit velocity v_a^q over the entire width of the exit, i.e., the exit velocity is everywhere uniform. In a similar manner, a zero value of g_2^q indicates that the qth average exit velocity v_a^q equals the prescribed gap-wise average exit velocity v_p^q, i.e., the die is delivering the desired flow rate. The small tolerances ε_1^q and ε_2^q are included on the exit velocity variation and the exit flow rate condition, respectively, so that the criteria for satisfying these two constraints for each flow condition q can be adjusted independently.

In the optimization problem above, $\boldsymbol{\phi}$ is the design variable vector with real components ϕ_i, $i = 1, 2 \ldots N$, limited by upper and lower bounds ϕ_i^U and ϕ_i^L, respectively, where N is the total number of design variables. N_s stationary design variables ϕ_j^s, $j = 1, 2 \ldots N_s$, are included in $\boldsymbol{\phi}$ which describe the geometry of the fixed die cavity region shown in figure 2.1. In addition, N_q adjustable model variables are defined,

and associated with each of the N_f flow conditions which are defined in terms of the design variables ϕ_k^q, $k = 1, 2 \ldots N_q$. These include parameters that define the choker bar position and die inlet pressures P_{in}^q in our die design examples. Therefore, the total number of design variables in $\boldsymbol{\phi}$ is $N = N_s + N_f N_q$.

The solution to the design optimization problem in equation 2.1 gives a single sheet extrusion die geometry that yields a uniform exit velocity with a prescribed flow rate over a range of operating conditions. This formulation assumes that an operator, or perhaps an automatic control device, may make adjustments for each flow condition considered in order to facilitate the optimal die flow operation. Note that the design calculations considered in this chapter address flow within the die itself, and do not take into account downstream effects such as die swell which are known to change the shape of the polymer stream once it exits the die cavity. A different approach will be given in chapter 3 to handle die lip expansion caused by extrusion pressure.

2.3 Polymer Melt Flow Modeling and Simulation

To optimize the die cavity geometry of a sheeting die such as that appearing in figure 2.1, a die flow simulation is required. The Hele-Shaw flow model [21] is developed from the principles of conservation of mass, momentum and energy, where assumptions are made to reduce computational time and data requirements. The polymer melt is modelled as a Generalized Newtonian Fluid, and therefore is assumed to be inelastic and incompressible. In addition, inertial, body and surface tension forces in the fluid

are assumed to be negligible. Moreover, the pressure does not vary significantly in the direction normal to the plane of flow, and the velocity in the direction normal to the plane of flow is negligible compared with the in-plane velocities (see e.g., figure 2.1). The die cavity thickness is assumed to be small compared to its in-plane dimensions and has little in-plane variation and all flow conditions are assumed to be symmetric with respect to the cavity mid-plane. This model is widely employed in injection and compression molding [21], and has also been applied to sheet extrusion dies [17, 22, 39, 41, 52, 53].

2.3.1   Governing Equations

Based on these assumptions, the mass and momentum conservation equations reduce to a single differential equation [21]

$$\boldsymbol{\nabla} \cdot S \, \boldsymbol{\nabla} P = 0 \tag{2.3}$$

where P is the pressure field over the flow cavity domain Ω in two-dimensions, and $\boldsymbol{\nabla}$ is the gradient operator in the x-y plane. The boundary conditions in the plane of flow are $P = P^p$ on $\partial \Omega^p$ and $S(\boldsymbol{\nabla} P \cdot \mathbf{n}) = q^p$ on $\partial \Omega^q$, where q^p is the prescribed flow rate. Hence, the boundary of the flow domain $\partial \Omega$ is divided into two complimentary sub-domains: $\partial \Omega^p$ and $\partial \Omega^q$. S is the flow conductance defined as an integral through the cavity thickness as [21]

$$S = \int_0^h \frac{z^2}{\eta(\dot{\gamma}(z))} \, dz \tag{2.4}$$

where the integration is performed from the die cavity mid-plane ($z = 0$) to its top surface ($z = h$). In equation 2.4, the viscosity η is a function of the strain rate

magnitude $\dot{\gamma}$ which is computed in this analysis at a distance z from the flow domain midplane as

$$\dot{\gamma} = \frac{z}{\eta} \|\boldsymbol{\nabla}P\| \tag{2.5}$$

where $\|\boldsymbol{\nabla}P\|$ is the magnitude of the pressure gradient in the plane of flow.

A residual R for the boundary value problem described in equation 2.3 is obtained via the method of weighted residuals (see e.g., [54]) in the usual manner as [53]

$$R(P) = \int_{\Omega} \boldsymbol{\nabla}w \cdot S(P)\boldsymbol{\nabla}P \, da - \int_{\partial\Omega^q} w \, q^P ds \tag{2.6}$$

where w is an arbitrary weighting function. The pressure field P that satisfies equation 2.6 is the solution to equation 2.3 if w vanishes on $\partial\Omega^p$, and P satisfies the boundary conditions on $\partial\Omega^p$ [22]. When non-Newtonian fluids are considered, S in equation 2.4 becomes a function of the pressure field, and equation 2.6 is non-linear in P, requiring iterative methods to compute a solution. In this research, the non-linear residual 2.6 is solved via the Newton-Raphson method since it exhibits terminal quadrature convergence and is conducive to the design sensitivity analysis to follow. The tangent operator $\frac{\partial R}{\partial P}$ operating on the increment $[\Delta P]$ is obtained by differentiating equation 2.6 with respect to P as

$$\frac{\partial R(P)}{\partial P}[\Delta P] = \int_{\Omega} \boldsymbol{\nabla}w \cdot \left[S(P)\boldsymbol{\nabla}[\Delta P] + \frac{\partial S(P)}{\partial P}[\Delta P]\boldsymbol{\nabla}P \right] da \tag{2.7}$$

where we have assumed that q^P in equation 2.6 is not a function of the pressure P. Note that equations 2.6 and 2.7 may include any Generalized Newtonian Fluid model in which the material model enters the computations through S and $\frac{\partial S}{\partial P}$.

22

2.3.2 Model Solution

The isoparametric finite element method (see e.g. [54]) is used to discretize the above equations when the two-dimensional flow domain Ω in equations 2.6 and 2.7 is divided into multiple finite element domains. The die cavity half-height h enters the calculations through the integral in equation 2.4. In the finite element analysis, the melt pressure field P and residual R in equation 2.6 become the nodal pressure vector $\mathbf{P}$ and residual vector $\mathbf{R}$, respectively (see e.g. [22,53]). In a similar manner, the tangent operator $\frac{\partial R}{\partial P}$ in equation 2.7 becomes the tangent matrix $\frac{\partial \mathbf{R}}{\partial \mathbf{P}}$. Once the residual $\mathbf{R}$ and tangent matrix $\frac{\partial \mathbf{R}}{\partial \mathbf{P}}$ are computed, the nodal pressures can be evaluated using Newton-Raphson iteration as

$$\frac{\partial \mathbf{R}(\mathbf{P}_i)}{\partial \mathbf{P}}[\Delta \mathbf{P}] = -\mathbf{R}(\mathbf{P}_i) \tag{2.8}$$

where nodal pressures are updated as $\mathbf{P}_{i+1} = \mathbf{P}_i + \Delta \mathbf{P}$. Iterations are repeated until convergence is reached. Once the pressure solution is computed, the gap-wise average velocity vector $\bar{\mathbf{v}}$ is evaluated from

$$\bar{\mathbf{v}} = -\frac{S}{h}\boldsymbol{\nabla}P \tag{2.9}$$

2.3.3 Generalized Newtonian Fluids

The Generalized Newtonian Fluid (GNF) model is widely used to represent the purely viscous non-Newtonian behavior of polymer melt flow (see e.g., [3,26]) where the shear stress tensor $\boldsymbol{\tau}$ is proportional to the strain-rate tensor $\dot{\boldsymbol{\gamma}}$ as

$$\boldsymbol{\tau} = \eta(\dot{\gamma})\dot{\boldsymbol{\gamma}} \tag{2.10}$$

Expressions for several GNF models are given in table 2.1, where model parameters are described in the literature (see e.g., [3, 42]).

- **Power-law fluid model**

When an isothermal power-law fluid model is employed, the viscosity $\eta = m\dot{\gamma}^{n-1}$ from table 2.1 may be substituted into equation 2.5 to obtain an explicit expression for η as a function of z. This result may be combined with equation 2.4 to evaluate the flow conductance S as [22]

$$S(P) = \frac{h^{\frac{1}{n}+2}}{m^{\frac{1}{n}}\left(\frac{1}{n}+2\right)}\|\boldsymbol{\nabla}P\|^{\frac{1}{n}-1} \tag{2.11}$$

Consequently, the term $\frac{\partial S}{\partial P}$ acting on the increment $[\Delta P]$ in the tangent operator $\frac{\partial R}{\partial P}$ in equation 2.7 is obtained by differentiating equation 2.11 with respect to P as [22]

$$\frac{\partial S}{\partial P}[\Delta P] = \frac{S(\frac{1}{n}-1)}{\|\boldsymbol{\nabla}P\|^2}\boldsymbol{\nabla}P \cdot \boldsymbol{\nabla}[\Delta P] \tag{2.12}$$

where we note that an analytical expression for $S(P)$ and $\frac{\partial S}{\partial P}$ are possible since m and n are independent of z for homogeneous isothermal flow. Note that equations 2.11 and 2.12 reduce to $S = \frac{h^3}{3\mu}$ and $\frac{\partial S}{\partial P} = 0$, respectively, for a Newtonian fluid with viscosity μ.

- **Ellis fluid model**

Since the power-law fluid model does not capture the near-constant viscosity at low strain rates, other more realistic GNF models such as the Ellis, Carreau-Yasuda, and Cross models are often used. These more complicated models can be used to

provide a better representation of the entire viscosity curve, combing a near-constant viscosity for low shear rates, a power-law at high shear rates, and a smooth transition in between. Figure 2.2 shows shear stress-viscosity curve for the Ellis model. The viscosity function of an isothermal Ellis fluid is given as (see table 2.1)

$$\eta = \frac{\eta_0}{1 + \left(\frac{\tau}{\tau_{1/2}}\right)^{\alpha-1}} \tag{2.13}$$

where η_0 is the zero shear viscosity, $\tau_{1/2}$ is the value of shear stress at $\eta = \eta_0/2$ and $(\alpha - 1)$ is the slope of the curve $log[(\eta_0/\eta) - 1]$ verse $log(\tau/\tau_{1/2})$ [55]. The flow conductance S for Ellis fluid can be obtained by substituting equation 2.13 into equation 2.4 as

$$S(P) = \frac{h^3}{3\eta_0} + \frac{h^{\alpha+2}}{\eta_0\,\tau_{1/2}^{\alpha-1}} \left(\frac{1}{\alpha+2}\right) \|\boldsymbol{\nabla}P\|^{\alpha-1} \tag{2.14}$$

The derivative $\frac{\partial S}{\partial P}$ in equation 2.7 is obtained by differentiating equation 2.14 with respect to P as

$$\frac{\partial S}{\partial P}[\Delta P] = \left(\frac{\alpha-1}{\alpha+2}\right) \frac{\tau_{1/2}^{1-\alpha}}{\eta_0} \frac{h^{\alpha+2}}{\|\boldsymbol{\nabla}P\|^{3-\alpha}} \boldsymbol{\nabla}P \cdot \boldsymbol{\nabla}[\Delta P] \tag{2.15}$$

- **Carreau-Yasuda, Cross, and Bingham fluid model**

When Carreau-Yasuda, Cross, and Bingham fluid models are employed, the simplicity of the analytical expression described above is lost since the viscosity η cannot be written as a function of $\|\nabla P\|$ in the generalized Hele-Shaw analysis. As a result, an analytical expression for the flow conductance S in 2.4 does not exist. Therefore,
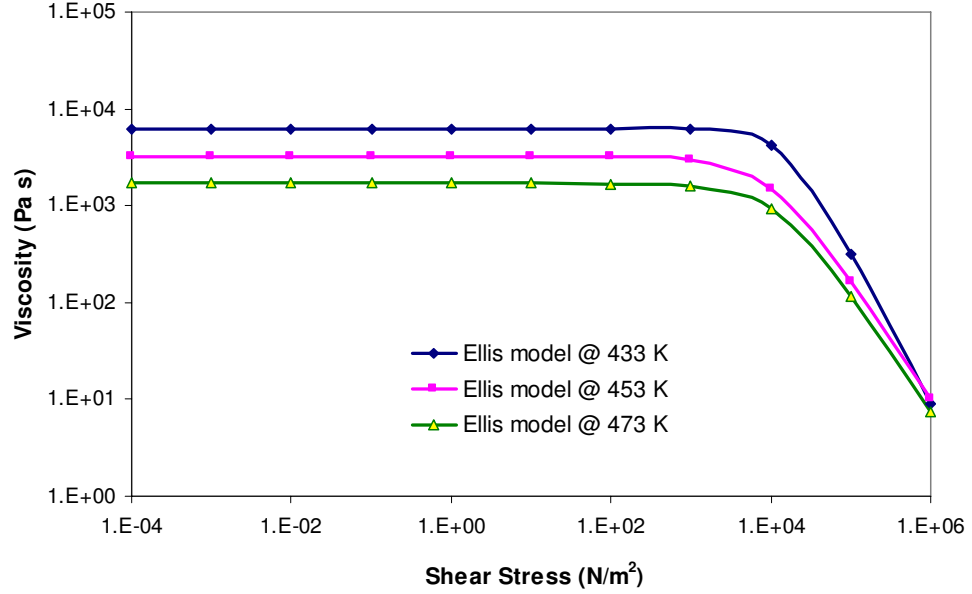
Figure 2.2: Viscosity versus shear stress and temperature for low density polyethylene (LDPE)

Gauss Quadrature (see e.g., [54]) is employed to numerically integrate equation 2.4 as

$$S = \sum_{i=1}^{NG} c_i \frac{z_i}{\eta(z_i)^2} \qquad (2.16)$$

where NG is the number of integration points ($NG = 8$ in this analysis), c_i are Gauss weighting factors, and the viscosity η is evaluated at selected z_i locations using equation 2.5 and the selected GNF viscosity formula from table 2.1.

Similarly, an analytical expression for the derivative $\frac{\partial S}{\partial P}$ in equation 2.7, such as that shown in equation 2.12 for the power-law fluid, does not exist for the Carreau-Yasuda, Cross, and Bingham fluid models. Since the domain of integration in equation

26

2.4 does not depend on P, we may differentiate its integrand to give

$$\frac{\partial S}{\partial P}[\Delta P] = -\int_0^h \frac{z^2}{\eta^2} \frac{\partial \eta}{\partial P}[\Delta P]\,dz \tag{2.17}$$

The viscosity derivative $\frac{\partial \eta}{\partial P}$ is evaluated by differentiating equation 2.5 and the selected viscosity formula in table 2.1 with respect to the pressure P, which yields

$$\frac{\partial \eta}{\partial P}[\Delta P] = \beta \frac{\boldsymbol{\nabla} P \cdot \boldsymbol{\nabla}[\Delta P]}{\|\boldsymbol{\nabla} P\|^2} \tag{2.18}$$

where the viscosity derivative factor β is defined for each of the GNF models considered in this study in table 2.2.

To numerically evaluate the integrals in equations 2.4 and 2.17, the viscosity η must be evaluated at selected z locations in a manner similar to that shown in equation 2.16. Unfortunately, when equation 2.5 is substituted into any of the viscosity equations given in table 2.1, a nonlinear equation in η is obtained which must be solved numerically via an iterative procedure such as the Newton-Raphson method. To illustrate the resulting viscosity calculation procedure, we consider the Carreau-Yasuda viscosity model given in table 2.1 as an example. A residual expression $r(\eta)$ based on the viscosity η as well as its first derivative $r'(\eta) = \frac{dr(\eta)}{d\eta}$ are defined, respectively, as

$$r(\eta) = \frac{\eta - \eta_\infty}{\eta_0} - (1 - \frac{\eta_\infty}{\eta_0})[1 + (\lambda \dot{\gamma})^a]^{\frac{(n-1)}{a}} \tag{2.19}$$

$$r'(\eta) = \frac{1}{\eta_0} + \frac{(n-1)(\eta - \eta_\infty)(\lambda \dot{\gamma})^a}{\eta\,\eta_0\,(1 + (\lambda \dot{\gamma})^a)} \tag{2.20}$$

where $\dot{\gamma}$ is computed for a given ∇P at each height z from equation 2.5. It is desired that $r(\eta) = 0$, so that at iteration i, the viscosity is updated via the Newton-Raphson method as $\eta_{i+1} = \eta_i - \frac{r(\eta_i)}{r'(\eta_i)}$ where iterations continue until convergence is achieved.

Table 2.1: Viscosity expressions for common generalized Newtonian fluids

Fluid model	Viscosity η
Power-law [3]	$m\,\dot{\gamma}^{n-1}$
Carreau-Yasuda* [3]	$\eta_\infty + (\eta_0 - \eta_\infty)[1 + (\lambda\,\dot{\gamma})^a]^{(n-1)/a}$
Ellis [3]	$\dfrac{\eta_0}{1+\left(\frac{\tau}{\tau_{1/2}}\right)^{\alpha-1}}$
Cross [42]	$\dfrac{\eta_0}{1+\left(\frac{\eta_0\,\dot{\gamma}}{\tau^*}\right)^{1-n}}$
Bingham [3]	$\begin{cases} \infty & \text{for} \quad \tau < \tau_y \\ \mu_0 + \frac{\tau_y}{\dot{\gamma}} & \text{for} \quad \tau \geq \tau_y \end{cases}$

$*$Reduce to the Carreau fluid model for $a = 2$ and $\eta_\infty = 0$

Table 2.2: Expressions for β for common generalized Newtonian fluids

Fluid model	β in equation 2.18 and 2.38
Power-law [3]	$\frac{n-1}{n}\,\eta$
Carreau-Yasuda [3]	$\dfrac{(n-1)\,(\lambda\,\dot{\gamma})^a\,(\eta-\eta_\infty)}{\eta+(\lambda\,\dot{\gamma})^a\,(\eta_\infty+n(\eta-\eta_\infty))}\,\eta$
Ellis [3]	$-\left[(\alpha-1)\left(\frac{\tau}{\tau_{1/2}}\right)^{\alpha-1}\right]\frac{\eta^2}{\eta_0}$
Cross [42]	$-\dfrac{\eta^2\,(1-n)\left(\frac{\eta_0\,\dot{\gamma}}{\tau^*}\right)^{1-n}}{\eta\,(1-n)\left(\frac{\eta_0\,\dot{\gamma}}{\tau^*}\right)^{1-n}-\eta_0}$
Bingham [3]	$-\frac{\tau_y\,\eta}{\mu_0\,\dot{\gamma}}\quad\text{for}\quad\tau\geq\tau_y$

Once the viscosity η is computed at all of the specified z locations, the flow conductance S and its derivative $\frac{\partial S}{\partial P}$ may be obtained via numerical integration of equations 2.4 and 2.17, respectively. The residual R and tangent operator $\frac{\partial R}{\partial P}$ can then be evaluated from equations 2.6 and 2.7, respectively.

2.4 Design Sensitivity Analysis (DSA)

Gradient-based optimization methods (see e.g., [56]) are commonly used to solve design problems such as that given in equation 2.1. In these problems, a significant advantage is derived from the efficient computation of the design sensitivities. Design sensitivities are simply the derivatives of the performance measures (such as the objective function or a constraint) with respect to the design parameters. Design sensitivities quantify the first-order effect of an input parameter on a desired response. In this work, a design sensitivity of interest is the derivative of the exit velocity constraint g_1 and g_2 with respect to a parameter that describes the shape of the die cavity. Design sensitivities are often used in "what if" studies, and serve as a key input for numerical optimization algorithms [56].

Computing design sensitivities of the cost and constraint functions with respect to design variables is relatively straight forward when the functions are explicit in ϕ (such as the objective function f in equation 2.1). In our design approach, however, the constraints are dependent on the pressure field obtained through a nonlinear finite element solution which is implicit in ϕ through equation 2.3. Design sensitivities are often evaluated by the finite difference method which are easily computed once a

simulation procedure is defined for evaluating the performance measures of interest. Unfortunately, finite difference derivatives have been shown to be inaccurate, inefficient, and unacceptable [57] for nonlinear problems such as that described in this work. Indeed, if the finite difference perturbation is too small then round-off errors result, and if it is too large then truncation errors occur. Also, N additional nonlinear finite element analyses are required, one for each design derivative, which can be computationally prohibitive. The accuracy may be improved with higher order finite difference formulas, but these are rarely used in design problems due to the increased computational expense.

2.4.1   The Adjoint Variable Method

This study computes the design sensitivities using the *adjoint variable method* (see e.g., [57,58]) which provides a more efficient and accurate means for obtaining gradients when compared to finite difference approaches. To compute design sensitivities for the sheeting die design problem with the adjoint variable method, a general implicit cost or constraint function is expressed as

$$F(\boldsymbol{\phi}) = G(\mathbf{P}^q(\boldsymbol{\phi}), \boldsymbol{\phi}), \quad q = 1, 2, \ldots N_f \tag{2.21}$$

where $\mathbf{P}^q$ is the vector of nodal pressures in the finite element analysis of the qth operating condition. In addition, the residual vector evaluated from equation 2.6 may be written for the qth flow condition following discretization as

$$\mathbf{R}^q(\mathbf{P}^q(\boldsymbol{\phi}), \boldsymbol{\phi}) = 0 \tag{2.22}$$

30

Lagrange multipliers $\boldsymbol{\lambda}^q$ are introduced for each flow condition which are used to define an augmented function $\hat{F}$ from equations 2.21 and 2.22 as

$$\hat{F}(\boldsymbol{\phi}) = G(\mathbf{P}^q(\boldsymbol{\phi}), \boldsymbol{\phi}) - \sum_{q=1}^{N_f} \boldsymbol{\lambda}^q \cdot \mathbf{R}^q(\mathbf{P}^q(\boldsymbol{\phi}), \boldsymbol{\phi}) \tag{2.23}$$

where we note that the qth residual $\mathbf{R}^q$ includes only the qth pressure solution vector $\mathbf{P}^q$. Note that $\hat{F}(\boldsymbol{\phi}) = F(\boldsymbol{\phi})$ since all designs $\boldsymbol{\phi}$ must satisfy the descritized residual equations $\mathbf{R}^q = 0$ for all $q = 1, 2 \ldots N_f$ in equation 2.22. Differentiation of $\hat{F}$ with respect to the ith design variable ϕ_i and some rearranging gives

$$\frac{d\hat{F}}{d\phi_i} = \frac{\partial G}{\partial \phi_i} - \sum_{q=1}^{N_f} \boldsymbol{\lambda}^q \cdot \frac{\partial \mathbf{R}^q}{\partial \phi_i} + \sum_{q=1}^{N_f} \left\{ \left[\frac{\partial G}{\partial \mathbf{P}^q} - \boldsymbol{\lambda}^q \cdot \frac{\partial \mathbf{R}^q}{\partial \mathbf{P}^q} \right] \frac{d\mathbf{P}^q}{d\phi_i} \right\} \tag{2.24}$$

where we note that $\frac{dF}{d\phi_i} = \frac{d\hat{F}}{d\phi_i}$ since $\mathbf{R}^q = 0$ for all flow conditions q. Additional analyses for computing the implicit response derivatives $\frac{d\mathbf{P}^q}{d\phi_i}$ in equation 2.24 are avoided by defining each adjoint vector $\boldsymbol{\lambda}^q$ to eliminate the coefficients of the $\frac{d\mathbf{P}^q}{d\phi_i}$. The resulting adjoint problems are

$$\left[\frac{\partial \mathbf{R}^q}{\partial \mathbf{P}^q} \right]^T \boldsymbol{\lambda}^q = \left\{ \frac{\partial G}{\partial \mathbf{P}^q} \right\}^T \quad q = 1, 2, \ldots N_f \tag{2.25}$$

where $\frac{\partial G}{\partial \mathbf{P}^q}$ is the qth adjoint load and $()^T$ indicates matrix transpose. Note that the original analysis is nonlinear, whereas the adjoint analysis is linear. Once the $\boldsymbol{\lambda}^q$ are evaluated, the unknown implicit response derivatives $\frac{d\mathbf{P}^q}{d\phi_i}$ are eliminated from equation 2.24 which reduces to

$$\frac{d\hat{F}}{d\phi_i} = \frac{\partial G}{\partial \phi_i} - \sum_{q=1}^{N_f} \boldsymbol{\lambda}^q \cdot \frac{\partial \mathbf{R}^q}{\partial \phi_i} \tag{2.26}$$

In the above, $\frac{\partial G}{\partial \mathbf{P}^q}$ is the adjoint load associated with the performance measure of interest. The adjoint variable method is computationally efficient since it only

requires the evaluation of one linear adjoint problem defined by equation 2.25 for each implicit objective and constraint function. Furthermore, it employs the transpose of the tangent matrix $\left[\frac{\partial \mathbf{R}^q}{\partial \mathbf{P}^q}\right]^T$ from equation 2.8 used in the Newton-Raphson iteration for the pressure solution, which significantly reduces the computational effort.

Since the constraints g_1^q and g_2^q in equation 2.1 are not explicitly dependent on the design variables considered in this study, $\frac{\partial G}{\partial \phi_i} = 0$ for all $\phi_i, i = 1 \ldots N$. However, these constraints do depend on $\boldsymbol{\phi}$ through the pressure solution. Therefore, g_1^q and g_2^q are differentiated with respect to the pressure vector $\mathbf{P}$ to, respectively, obtain the right-hand-side of equation 2.25 as

$$\frac{\partial g_1^q}{\partial \mathbf{P}} = \frac{1}{L} \int_{l_{exit}} 2\left(\frac{\bar{v}^q}{v_a^q} - 1\right)\left[\frac{\partial \bar{v}^q}{\partial \mathbf{P}}\frac{1}{v_a^q} - \frac{\bar{v}^q}{(v_a^q)^2}\frac{\partial v_a^q}{\partial \mathbf{P}}\right] dx \qquad (2.27)$$

$$\frac{\partial g_2^q}{\partial \mathbf{P}} = 2\left(\frac{v_a^q}{v_p^q} - 1\right)\left(\frac{1}{v_p^q}\frac{\partial v_a^q}{\partial \mathbf{P}}\right) \qquad (2.28)$$

It should be noted that the integral of equation 2.27 is defined over the entire length along the die exit. The derivatives $\frac{\partial \bar{v}^q}{\partial P}$ and $\frac{\partial v_a^q}{\partial P}$ are, respectively, computed by differentiating equation 2.9 as

$$\frac{\partial \bar{v}^q}{\partial P}[\Delta P] = \frac{1}{h}\left[\frac{\partial S}{\partial P}[\Delta P]\|\boldsymbol{\nabla}P\| + \frac{S}{\|\boldsymbol{\nabla}P\|}\boldsymbol{\nabla}P \cdot \boldsymbol{\nabla}[\Delta P]\right] \qquad (2.29)$$

and equation 2.2 as

$$\frac{\partial v_a^q}{\partial P}[\Delta P] = \frac{1}{L} \int_{l_{exit}} \frac{\partial \bar{v}^q}{\partial P}[\Delta P] \, dx \qquad (2.30)$$

Following finite element discretization, $\frac{\partial \bar{v}^q}{\partial \mathbf{P}}$ and $\frac{\partial v_a^q}{\partial \mathbf{P}}$ are obtained from equations 2.29 and 2.30, respectively. By substituting $\frac{\partial \bar{v}^q}{\partial \mathbf{P}}$ and $\frac{\partial v_a^q}{\partial \mathbf{P}}$ in equations 2.27 and 2.28, the derivatives $\frac{\partial g_1^q}{\partial \mathbf{P}}$ and $\frac{\partial g_2^q}{\partial \mathbf{P}}$ are obtained.

To compute the design derivatives $\frac{\partial \mathbf{R}^q}{\partial \phi_i}$ in equation 2.26, the pressure and height design variables are considered separately. In the case of $\phi_i = P_{in}^q$, the design derivative $\frac{\partial \mathbf{R}^q}{\partial \phi_i}$ is computed using the tangent matrix $\frac{\partial \mathbf{R}^q}{\partial \mathbf{P}^q}$ as

$$\frac{\partial \mathbf{R}^q}{\partial P_{in}^q} = \frac{\partial \mathbf{R}^q}{\partial \mathbf{P}^q} \frac{\partial \mathbf{P}^q}{\partial P_{in}^q} \tag{2.31}$$

where $\frac{\partial \mathbf{P}^q}{\partial P_{in}^q}$ is a zero vector with unity in the components associated with P_{in}^q, $q = 1, 2, \ldots N_f$ where N_f is the number of operating or flow conditions considered in the design problem. Therefore, only those nodes associated with inlet pressure P_{in}^q need to be considered when computing equation 2.31. Note that $\frac{\partial \mathbf{R}}{\partial P_{in}}$ is identical for any Generalized Newtonian Fluid model.

When ϕ_i defines a cavity half-height, equation 2.6 is differentiated with respect to ϕ_i as

$$\frac{\partial R^q}{\partial \phi_i} = \int_\Omega \boldsymbol{\nabla} w \cdot \frac{\partial S}{\partial \phi_i} \boldsymbol{\nabla} P \, da \tag{2.32}$$

which may be evaluated with the finite element method to obtain an expression for $\frac{\partial \mathbf{R}^q}{\partial \phi_i}$. Here we assume q^P in equation 2.6 is not a function of the half-height parameter. Note that the evaluation of $\frac{\partial R}{\partial \phi_i}$ in equation 2.32 applies to any viscosity model described in table 2.1 as described below.

Once the terms $\frac{\partial g_1^q}{\partial \mathbf{P}}$, $\frac{\partial g_2^q}{\partial \mathbf{P}}$, and $\frac{\partial \mathbf{R}^q}{\partial \phi_i}$ are computed, the adjoint variable vector $\boldsymbol{\lambda}^q$ is obtained with equation 2.25 and the design sensitivity $\frac{D\hat{F}}{D\phi_i}$ follows from equation 2.26. In these computations, we must evaluate $\frac{\partial S}{\partial \mathbf{P}}$ and $\frac{\partial S}{\partial \phi_i}$ which depend on the fluid viscosity model. The finite element expression $\frac{\partial S}{\partial \mathbf{P}}$ can be derived from equation 2.17. In the ensuing section, we evaluate $\frac{\partial S}{\partial \phi_i}$ for various GNF models, i.e., power-law,

Carreau-Yasuda, Ellis, Cross, and Bingham fluid.

2.4.2 DSA for Generalized Newtonian Fluids

- **Power-law fluid model**

For an isothermal power-law fluid, the flow conductance S in equation 2.11 is an explicit function of the half-height $h(\boldsymbol{\phi})$ so that the design derivative $\frac{\partial S}{\partial \phi_i}$ in equation 2.32 may be computed from

$$\frac{\partial S}{\partial \phi_i} = \frac{(\frac{1}{n} + 2)S}{h}\frac{\partial h}{\partial \phi_i} \tag{2.33}$$

where S from equation 2.11 is employed to simplify the final expression. Note that equation 2.33 reduces to $\frac{\partial S}{\partial \phi_i} = \frac{3S}{h}\frac{\partial h}{\partial \phi_i}$ for a Newtonian fluid.

In the examples to follow, we define the cavity half-height $h(x, y)$ over each element as $h(x, y) = \mathbf{N}\overset{n}{\mathbf{h}}$ where $\mathbf{N}$ contains the element interpolation functions and $\overset{n}{\mathbf{h}}$ is the nodal half-height vector. When a nodal half-height h^J is defined by the design variable ϕ_i, the height sensitivity $\frac{\partial h}{\partial \phi_i}$ with respect to that nodal half-height design variable at node J, i.e., $\phi_i = h^J$, is

$$\frac{\partial h}{\partial \phi_i} = \mathbf{N}\frac{\partial \overset{n}{\mathbf{h}}}{\partial h^J} = \sum_{I=1}^{n_e} N^I \delta_{IJ} = N^J \tag{2.34}$$

where N^I is the I-th component of the interpolation function matrix $\mathbf{N}$ and δ_{IJ} is the Kronecker delta ($\delta_{IJ} = 1$ for $I = J$ and $\delta_{IJ} = 0$ for $I \neq J$). Here we only consider n_e elements that contain the J-th node.

- **Ellis fluid model**

In a similar manner, we compute the design derivative $\frac{\partial S}{\partial \phi_i}$ for Ellis fluid model as

$$\frac{\partial S}{\partial \phi_i} = \frac{h^2}{\eta_0} \frac{\partial h}{\partial \phi_i} + \frac{h^{\alpha+1}}{\eta_0 \, \tau_{1/2}^{\alpha-1}} \frac{1}{\|\boldsymbol{\nabla} P\|^{1-\alpha}} \frac{\partial h}{\partial \phi_i} \qquad (2.35)$$

where $\frac{\partial h}{\partial \phi_i}$ is given in equation 2.34.

- **Carreau-Yasuda, Cross, and Bingham fluid model**

When any of the other GNF models, i.e., Carreau-Yasuda, Cross, and Bingham fluid model, are employed, the derivative $\frac{\partial S}{\partial \phi_i}$ cannot be obtained analytically since an explicit expression for S does not exist. Therefore, the flow conductance sensitivity must be calculated numerically. The flow conductance S of equation 2.4 may be rewritten to express its dependence on $\boldsymbol{\phi}$ as

$$S(\boldsymbol{\phi}) = \int_0^{h(\boldsymbol{\phi})} \frac{z(\boldsymbol{\phi})^2}{\eta(\boldsymbol{\phi})} \, dz \qquad (2.36)$$

Since the upper integration limit is a function of $\boldsymbol{\phi}$, we employ the domain parametrization method from [59] to the fixed domain $r \in [-1, 1]$ using $z = \frac{h}{2}(r + 1)$ to compute $\frac{\partial S}{\partial \phi_i}$. The design derivative of S is obtained from equation 2.36 following mathematical manipulation as

$$\frac{\partial S}{\partial \phi_i} = \frac{3h}{4} \frac{\partial h}{\partial \phi_i} S - \frac{h^2}{4} \int_0^h \frac{\partial \eta}{\partial \phi_i} \frac{z^2}{\eta^2} \, dz \qquad (2.37)$$

where the integral is evaluated with Gauss Quadrature to be consistent with the numerical procedure described for equation 2.16 when evaluating S in equation 2.4. Differentiating the viscosity η with respect to the design variable ϕ_i for a Generalized Newtonian Fluid yields

$$\frac{\partial \eta}{\partial \phi_i} = \beta \frac{1}{h} \frac{\partial h}{\partial \phi_i} \qquad (2.38)$$

35

where the viscosity derivative factor β for each Generalized Newtonian Fluid is given in table 2.2. Note that β is identical to that used in equation 2.18 when computing $\frac{\partial \eta}{\partial P}$.

Therefore, $\frac{\partial \mathbf{R}^q}{\partial \phi_i}$ for a Generalized Newtonian Fluid is computed from the discretization of equation 2.32 using equations 2.37 and 2.38. The design sensitivity of g_1^q and g_2^q in equation 2.1 then follows from equation 2.26 using equations 2.27 and 2.28, respectively.

2.5   Example Sheeting Die Designs

To illustrate the polymer sheeting die design methodology described above, a single sheeting cavity die with adjustable features is determined to accommodate the flow of polymer melt at multiple operating conditions. The specific die geometry used in this study is shown in figure 2.3 which is symmetric about the die's centerline (i.e., $x = 0$), and is similar to that presented by Gifford [25]. It consists of four main regions: the manifold, preland, secondary manifold, and land. The purpose of the manifold is to distribute the polymer melt uniformly across the die, and the preland and secondary manifold act as a resistance to flow which promotes velocity uniformity at the die exit while raising the pressure drop through the die. The land defines the thickness of the polymer melt immediately exiting the die.

The inlet and outlet die half-heights in figure 2.3 are fixed at 19.05 mm and 2.0 mm, respectively. The total inlet and exit widths are 101.6 mm and 1016 mm, respectively, making the die exit aspect ratio 254 : 1. The overall die length (in the

36
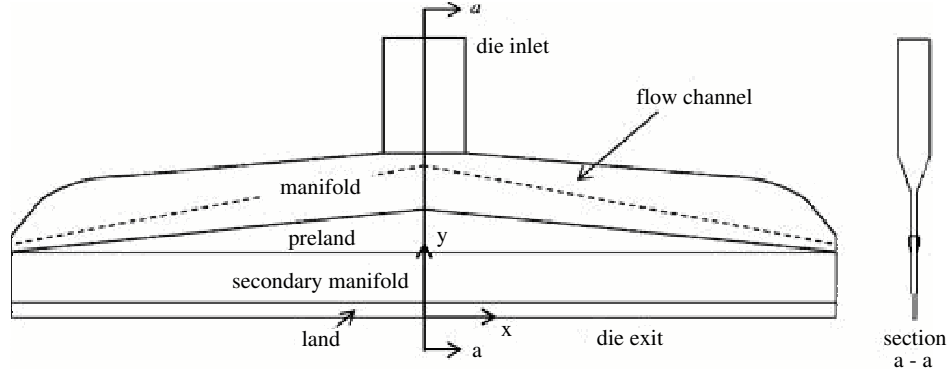
Figure 2.3: Coat hanger die cavity geometry

y direction in figure 2.3), is 330 mm which includes the 137 mm long inlet channel. The land, secondary manifold, and preland lengths along the die centerline are 25.4 mm, 50.8 mm, and 50.8 mm, respectively. The centerline length of the preland is 25.4 mm. There is a flow channel along the top of the die in the manifold region which has a uniform half-height in the y direction and a centerline length of 15.2 mm. The manifold also includes a region with a centerline length of 50.8 mm with a half-height that decreases linearly in the y direction between the flow channel and the die preland. Additional dimensions that define our die cavity geometry appear in table 2.1 of Gifford [25]. For illustrative purposes, the die geometry in figure 2.3 represents the entire flow domain, however, all of the calculations to follow are performed with a half-symmetry model in $x \geq 0$ (not shown) having 976 nodes and 1369 elements.

In this design problem, the half-height in the preland and manifold areas shown in figure 2.3 are defined by $N_s = 4$ stationary design variables. The half-height in the preland area is defined in terms of the design ϕ as the quadratic function of x given

as

$$h(x) = \phi_1^s + (\phi_2^s - \phi_1^s) \left(\frac{x}{L}\right)^2 \tag{2.39}$$

where $L = 508$ mm is the die half-width. Note that the design variables ϕ_1^s and ϕ_2^s in equation 2.39 are the preland half-height at $x = 0$ and $x = L$, respectively. In addition, the die cavity half-height in the manifold flow channel along the top of the die is defined by the Lagrange interpolating polynomial in x as

$$h(x) = \frac{(x - L/2)(x - L)}{L^2/2} h_0 + \frac{(x)(x - L)}{-L^2/4} \phi_3^s + \frac{(x)(x - L/2)}{L^2/2} \phi_4^s \tag{2.40}$$

where $h_0 = 19.05$ mm is the flow channel half-height at the die cavity centerline. Note that equation 2.40 is written such that ϕ_3^s and ϕ_4^s are the flow channel half-heights at $x = L/2$ and $x = L$, respectively. All stationary half-heights are bound by $1.0 \leq \phi_j^s \leq 19.05$ mm, $j = 1, 2, \ldots N_s$, which restricts the die gap to be less than that of the inlet channel.

Each of the flow conditions in the die design problem described above has $N_q = 4$ adjustable model variables for all flow conditions q that are included in the design variable vector $\boldsymbol{\phi}$. The inlet pressure for each flow condition is defined by the design as $P_{in}^q = \phi_1^q$. Inlet pressure design variables for all designs considered in this study are bounded by $1.0 \leq P_{in}^q \leq 20.0$ MPa. In addition, the secondary manifold region in figure 2.3 is treated as a choker bar where the die cavity half-height $h(x, y)$ can be adjusted independently for each flow condition. To accomplish this in the optimization problem, the die cavity half-height h^q in the secondary manifold for the qth flow

condition is defined as

$$h^q(x) = \phi_2^q + (-7.0\,\phi_2^q + 8.0\,\phi_3^q - \phi_4^q)\left(\frac{x}{L}\right)^2$$
$$+ (6.0\,\phi_2^q - 8.0\,\phi_3^q + 2.0\,\phi_4^q)\left(\frac{x}{L}\right)^3 \qquad (2.41)$$

which describes a cubic polynomial in x in terms of the design parameters ϕ_k^q, $k = 1, 2, \ldots N_q$ where $\frac{dh^q}{dx(0)} = 0$ is imposed. In equation 2.41, the design variables ϕ_2^q, ϕ_3^q, and ϕ_4^q are the die cavity half-height at $x = 0$, $x = L/2$, and $x = L$, respectively. All adjustable half-height design variables are bound by $0.0001 \leq \phi_k^q \leq 5.0$ mm, $k = 1, 2, \ldots N_q$, in the die optimizations below.

Example calculations that illustrate the usefulness of the die design approach are provided below. While studies exist such that experimentally validate polymer processing simulation methods similar to those described above (see e.g., Hieber and Shen [21] and Dooley [23]), testing to support our die design methodology is not included in this work. Experiments to illustrate the accuracy of the computed die cavities given below would increase confidence in these results, but are beyond the scope of the current study. The examples below use the Ellis model, however, other GNF models appearing in table 2.1 could have been included with little additional effort (see e.g., [5–7]).

2.5.1 Multi-Temperature Die Design

The first example considers the optimal design of the sheeting die shown in figure 2.3 using the design parametrization described above. The design optimization is performed to solve equation 2.1 for the flow of LDPE at three temperatures, 473K,

Table 2.3: Ellis material properties for Low Density Polyethylene (LDPE) and Polypropylene (PP)

Polymer melt	Temperature (K)	α	$\tau_{1/2}\left(\frac{N}{m^2}\right)$	$\eta_0\left(\frac{N \cdot s}{m^2}\right)$
LDPE	473	2.23	12000	1700
LDPE	453	2.22	9060	3200
LDPE	433	2.56	15200	6300
PP	473	2.49	7170	2500
PP	463	2.50	7190	3200
PP	453	2.72	9570	4210

453K, and 433K, such that $N_f = 3$. Material properties for the Ellis fluid model used in this example are given in table 2.3. The resulting optimization problem contains $N = 16$ design variables and a total of six constraints. The prescribed gap-wise average velocity is $v_p^q = 500$ mm/s and constraint tolerances are defined as $\varepsilon_1^q = 0.0001$ and $\varepsilon_2^q = 0.00005$ for all flow conditions $q = 1, 2, 3$.

New designs are computed using the Design Optimization Tools (DOT) modified method of feasible directions algorithm [60] in ten optimization iterations, requiring 40 functions and ten design sensitivity evaluations. The latter are obtained via the adjoint variable method using equations 2.25 and 2.26. Design variables and performance measures given in equation 2.1 appear in tables 2.4 and 2.5 which show the initial and optimal design values. Die cavity half-heights over the flow domain appear in figure 2.4.

Values of the objective function appearing in table 2.4 show that the optimization reduced the average pressure drop through the die, as expected. Upon comparing values of the stationary model variables given in table 2.4, it can be seen that the

Table 2.4: Objective function and stationary model variable values for LDPE multiple operating condition optimization

Die design	Initial	Optimal
Objective function f	7.5	7.381
Preland half-height at $x = 0$, ϕ_1^s (mm)	3.048	2.865
Preland half-height at $x = L$, ϕ_2^s (mm)	3.048	3.043
Manifold half-height at $x = L/2$, ϕ_3^s (mm)	12.05	13.04
Manifold half-height at $x = L$, ϕ_4^s (mm)	5.080	5.219
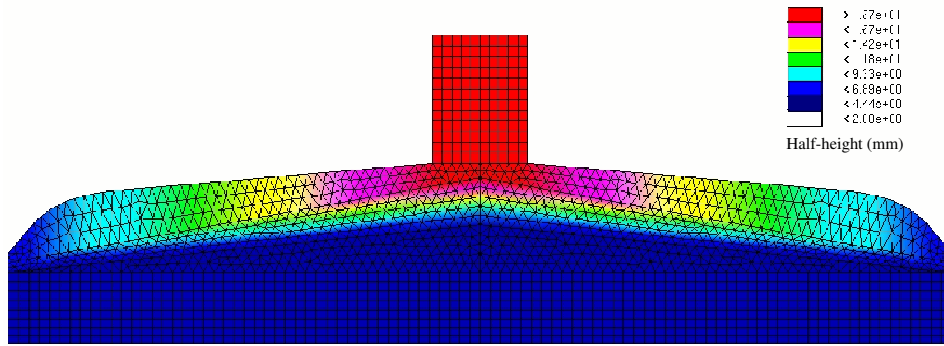
Figure 2.4: Initial die cavity half-heights for multiple operating condition optimizations

reduction in pressure drops were accomplished, in part, by increasing the cross section of the flow channel in the manifold and decreasing the gap thickness in the preland. Changes in the adjustable model variables also contributed to the improved performance as summarized in table 2.5. For example, the die entrance pressures are adjusted for each flow condition so that the desired die flow rate is achieved. Note that as the melt temperature decreases, the viscosity increases, and so does the required die entrance pressure. Table 2.5 also shows that the cavity thickness in the secondary manifold (i.e., that defined by the choker bar design variables) decreases slightly near the die center, and increases near the die's outer edge. In all cases, the

Table 2.5: Adjustable model variables and exit velocity constraint values for LDPE multiple operating condition optimization

Flow condition q	1		2		3	
melt temperature	473K		453K		433K	
Die design	Initial	Optimal	Initial	Optimal	Initial	Optimal
		Design variables				
$\phi_1^q = P_{in}^q$ (MPa)	7.5	6.147	7.5	7.021	7.5	8.976
ϕ_2^q (mm)	2.0	1.920	2.0	1.969	2.0	2.053
ϕ_3^q (mm)	2.0	1.899	2.0	1.959	2.0	2.074
ϕ_4^q (mm)	2.0	2.020	2.0	2.086	2.0	2.303
		Constraints				
$g_1^q \times 10^4$	59.9	0.166	64.0	0.224	120	0.653
$g_2^q \times 10^4$	4140	0.311	304	0.207	1790	0.500
		Exit velocities (mm/s)				
Average	821.7	502.8	587.2	502.3	288.3	496.5
Minimum	684.3	500.3	485.9	497.3	221.6	487.4
Maximum	880.9	506.4	631.1	504.9	318.9	501.4

optimization procedure reduces the exit velocity variations and die flow rate deviations as measured by g_1^q and g_2^q, respectively, in equation 2.1 to within the prescribed tolerances ε_1^q and ε_2^q. For example, $g_1^{(2)}$ is reduced by 99.65% (from 64.0×10^{-4} to 0.224×10^{-4}) and $g_2^{(1)}$ is reduced by 99.9925% (from 4140×10^{-4} to 0.311×10^{-4}) in the optimization. The uniformity in exit velocity for all of the flow conditions is further evidenced by the reduction in the difference between the maximum and minimum exit velocities given in table 2.5. Note also that the optimal average exit velocity changes significantly for all of the flow conditions which achieve results that are near the prescribed flow rate $v_p^q = 500$ mm/s for all $q = 1, 2, 3$.

Die half-heights are presented in figure 2.4 for the initial die cavity design which illustrates the decrease in half-height from the die entrance to its exit as described above. Changes in the die cavity half-heights during the optimization are illustrated

in figure 2.5 for flow condition $q = 2$ (i.e., LDPE at 453K). The flow channel in the manifold region of the optimal design is slightly elevated over that in the initial design and the preland decreases in height near the die center. Note that half-height changes are also seen in the choker bar region, however, this particular plot reflects the adjustable model variables associated with the $q = 2$ flow condition only. The choker bar heights for the optimal design are different for the other flow conditions, as described below. To better quantify the change to the die cavity geometry, manifold, and preland heights are plotted for the initial and optimal designs in figure 2.6.
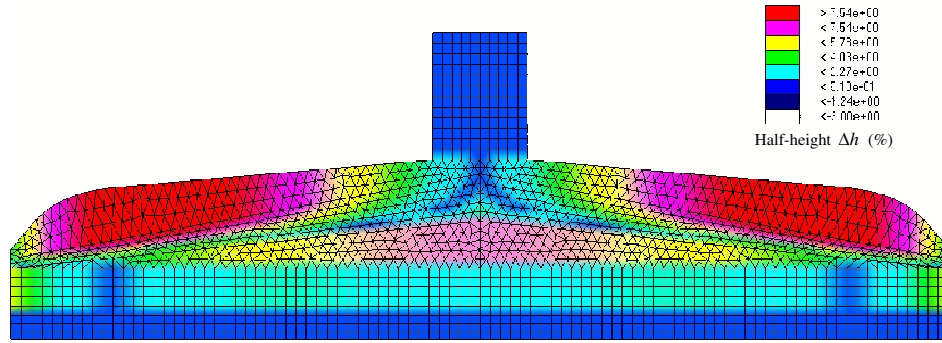
Figure 2.5: Percent change in die cavity half-height between initial and optimal designs for LDPE multiple operating temperature optimization [half-height shown for $q = 2$ (i.e., LDPE at 453K)]

Half-heights in the secondary manifold (i.e., choker bar) that are defined by the adjustable model variables are shown for each flow condition in figure 2.7. Note that a greater restriction is placed on the higher temperature, lower viscosity material to retard its flow. These choker bar half-height plots also illustrate that a uniform exit velocity for the intermediate temperature flow (i.e., 453K) is achieved with a choker bar shape that increases the half-height near the center of the die. Die exit

43

Table 2.6: Melt flow conditions for multiple temperature, material, and flow rate die design

q	1	2	3	4	5	6	7	8
v_p^q (mm/s)	300	300	300	300	700	700	700	700
Material	LDPE	LDPE	PP	PP	LDPE	LDPE	PP	PP
Temperature (K)	473	433	463	453	473	433	463	453

velocities are plotted for the initial and optimal designs in figure 2.8. Note that the exit velocities for the initial design are far from the desired average, and exhibits a significantly higher velocity along the centerline of the die than at its edge. As expected, the lower temperature material exits with the lowest velocity. The optimal results are much improved, and illustrate how well all of the flow conditions are able to meet the desired exit velocity over the entire width of the die.

2.5.2 Multi-Material, Temperature, and Flow Rate Die Design

This example considers the design of a sheeting die that performs well using multiple materials, temperatures, and flow rates. Both LDPE and PP (see e.g., table 2.3) are considered where the $N_f = 8$ flow conditions are defined in table 2.6. The resulting optimization problem contains $N = 36$ (i.e., $N_s = 4$ and $N_q = 4$) design variables and a total of 16 constraints, two for each of the N_f flow conditions. Constraint tolerances in equation 2.1 are defined as $\varepsilon_1^q = 0.0001$ and $\varepsilon_2^q = 0.00005$ for all of the flow conditions.

In this example, new designs are computed using the DOT modified method of feasible directions algorithm [60] in 12 optimization iterations, requiring 46 function

Table 2.7: Objective function and stationary model variable values for LDPE and PP multiple temperature and flow rate die optimization

Die design	Initial	Optimal
Objective function f	5.000	5.363
Preland half-height at $x = 0$, ϕ_1^s (mm)	3.048	3.242
Preland half-height at $x = L$, ϕ_2^s (mm)	3.048	3.123
Manifold half-height at $x = L/2$, ϕ_3^s (mm)	12.05	15.95
Manifold half-height at $x = L$, ϕ_4^s (mm)	5.080	5.500

and 12 gradient evaluations. Design variables and performance measures given in equation 2.1 appear in tables 2.7 and 2.8 which show the initial and optimal design variable values. Half-height and exit velocity plots are omitted in this example for conciseness.

Overall, the inlet pressures are increased from initial values of $P = 5.0$ MPa, $q = 1, 2, \ldots 8$ as shown in table 2.7 to accommodate the exit velocity constraints. The stationary variables that describe the cavity half-heights, also given in table 2.7, show that the optimization increases the half-height in both the flow channel (manifold) and the preland regions. The preland half-height is nearly uniform across the die width, increasing slightly toward the outer edge of the die. Note that a uniform preland is more typical in industrial applications and that this half-height distribution is in contrast to the previous example which resulted in a significant decrease in the preland height near the die center. Table 2.8 gives values for the adjustable model variables, constraints g_1^q and g_2^q in equation 2.1, and exit velocities for all of the flow conditions considered in this example. Note that the initial values of the adjustable model variables are the same as those used in the previous die design example which are given

45

Table 2.8: Adjustable model variable, constraint and exit velocity values for LDPE and PP multiple temperature and flow rate die optimization (ini=initial and opt=optimal)

| Flow condition q	1	2	3	4	5	6	7	8
Design variables (optimal design)								
$\phi_1^q = P_{in}^q$ (MPa)	4.196	6.395	3.622	4.071	5.871	8.467	4.883	5.398
ϕ_2^q (mm)	2.083	2.281	2.004	2.038	2.250	2.489	2.121	2.150
ϕ_3^q (mm)	2.066	2.279	2.001	2.039	2.240	2.494	2.122	2.154
ϕ_4^q (mm)	2.130	2.407	2.116	2.161	2.290	2.679	2.227	2.313
Constraints								
$g_1^q \times 10^4$ (ini)	49.0	97.5	118.0	165.0	49.0	97.5	118.0	165.0
(opt)	0.546	0.688	0.584	0.608	0.844	0.867	0.733	0.495
$g_2^q \times 10^4$ (ini)	312.0	4.05E3	7.24E3	1.34E3	2.46E3	7.13E3	427.0	1.72E3
(opt)	0.211	0.287	0.422	0.597	0.163	0.0496	0.348	0.0399
Exit velocities (mm/s)								
Average (ini)	353.0	109.1	555.3	409.6	353.0	109.1	555.3	409.6
(opt)	302.0	299.4	301.7	302.3	697.2	699.6	697.1	704.7
Minimum (ini)	299.2	86.1	427.7	299.4	299.2	86.1	427.7	299.4
(opt)	298.8	287.2	299.2	295.6	675.3	668.9	670.3	676.4
Maximum (ini)	375.7	119.4	613.6	461.6	375.7	119.4	613.6	461.6
(opt)	304.3	303.2	304.0	304.8	705.9	707.2	705.4	713.9

in table 2.3. In all flow conditions, the exit velocity constraints are reduced to values below the imposed acceptable tolerance in the design optimizations. For example, table 2.8 shows that $g_1^{(2)}$ is reduced by 99.3% (from 97.5×10^{-4} to 0.688×10^{-4}) and $g_2^{(2)}$ is reduced by 99.99% (from 4050×10^{-4} to 0.287×10^{-4}) in the optimization. Further evidence of the success of the optimization may be seen upon inspection of the exit velocities in table 2.8. For example, the average exit velocity approaches 300 mm/s for $q = 1, 2, 3, 4$, and 700 mm/s for $q = 5, 6, 7, 8$. Minimum and maximum exit velocities are also given which indicate the uniformity of exit flow for all flow conditions in the optimal design.

2.6 Summary

This chapter presents an optimization problem and solution procedure that may be used for materials processing design problems where adjustable parameters are employed to accommodate manufacturing variations. The practical application of this approach requires that the design engineer identify specific design variables that may be defined as part of the process or tooling specification, and those that may be modified during production to accommodate variability in process inputs. The example given here requires a finite element model be developed to evaluate the flow of polymer melt in a sheet extrusion die where model inputs are defined by design variables. Adjustments to the model are then prescribed by an optimization algorithm which solves the user defined design problem.

The design methodology given here is applied to polymer sheeting die design and

addresses the need for developing dies capable of performing well under multiple operating conditions. Various Generalized Newtonian Fluid models are included in the flow simulations and sensitivity analyses required for the optimization calculations. A viscosity derivative factor is derived which facilitates both the Newton-Raphson iteration procedure and our design sensitivity computations. The adjoint variable method is employed to compute design sensitivities for our numerical optimizations. The results show that a single sheeting die cavity geometry can be obtained that has improved performance when processing different materials operating over a range of melt flow temperatures, and melt flow rates.
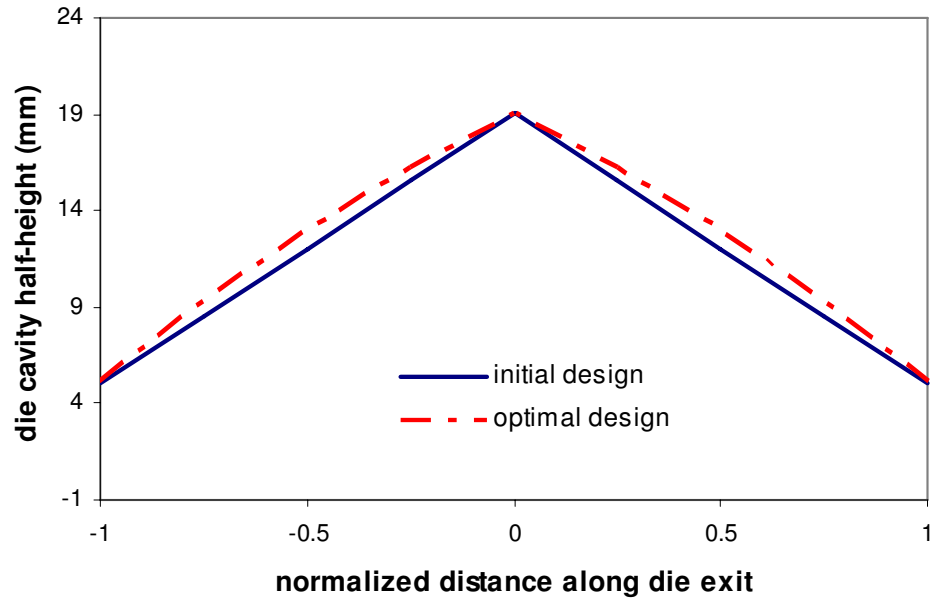
(a) flow channel half-height
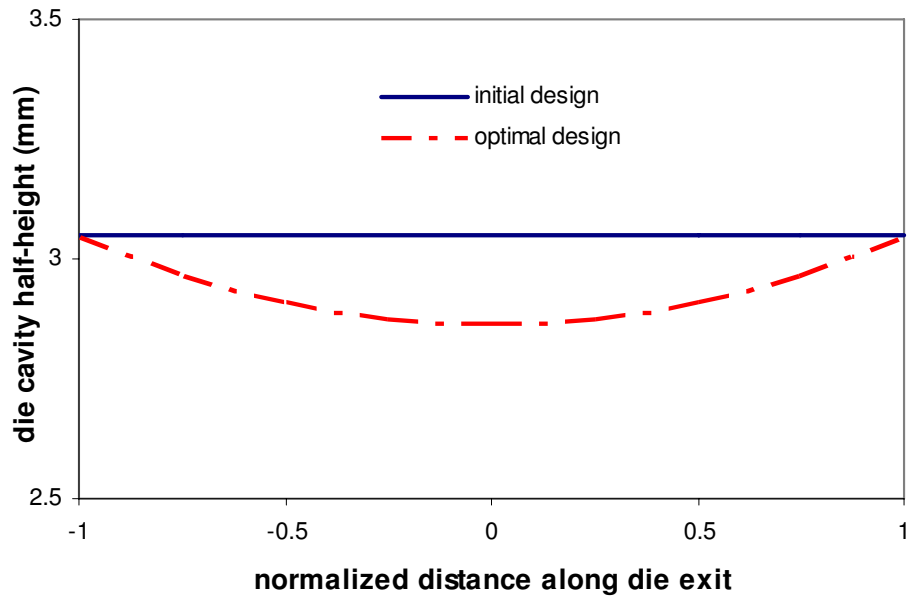
(b) preland half-height

Figure 2.6: Die cavity half-height in the manifold flow channel and the preland for LDPE multiple operating temperature optimization
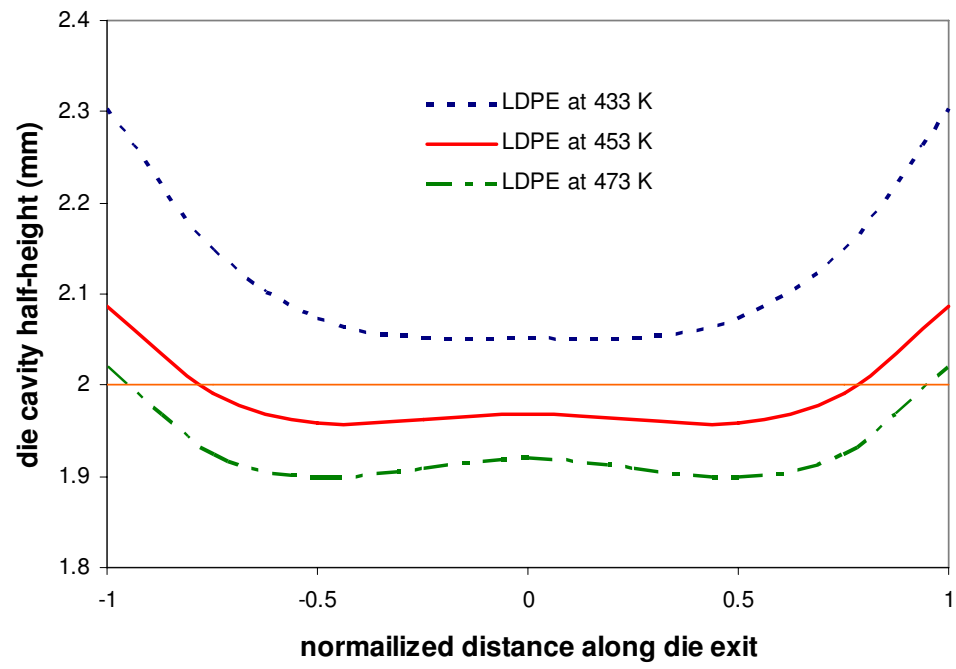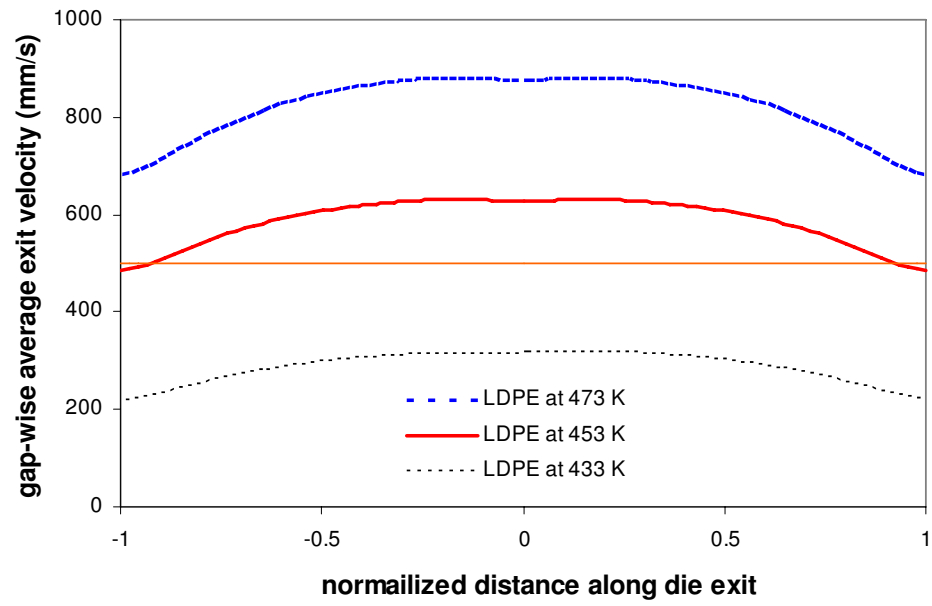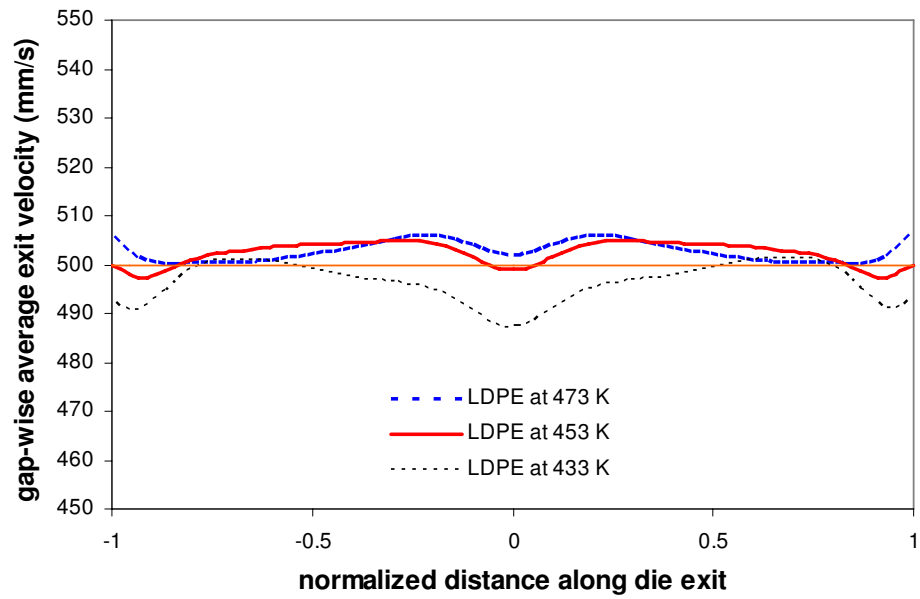
Figure 2.7: Choker bar half-height across die for optimal design in LDPE multiple temperature die design

(a) initial design

(b) optimal design

Figure 2.8: Exit velocities for LDPE multiple temperature die design

51

CHAPTER 3

FLUID-STRUCTURE INTERACTION

In this chapter, a polymer sheeting die design methodology is presented which integrates the simulation of polymer melt flow and die cavity deformation with numerical optimization to compute die cavity geometry capable of giving a near-uniform exit flow rate. In this research, both polymer melt flow and sheeting die deformation are analyzed with a general purpose finite element program. The approach includes a user-defined element that is used to evaluate the purely viscous non-Newtonian flow in a flat die. The flow analysis, which is simplified with the Hele-Shaw approximation, is coupled with a three-dimensional finite element simulation for die deformation. In addition, an optimal sheeting die cavity geometry is determined by the incorporation of the coupled analyses in our constrained optimization algorithm. A sample problem is discussed to illustrate the die design methodology [7, 47, 48].

3.1   Background

The analysis and design of the polymer extrusion process have received much attention over the last few decades, but only a few attempts have appeared in the literature that analyze the die deformation [45, 46]. It is well known that high internal pressures within the viscous polymer melt flow, acting over the large area of the die flow channel surface, exert forces high enough to bring about significant deformation of the die body, opening up the die, particularly towards the lips and near the center line.

52

This effect (commonly referred to as "clamshelling") can seriously affect melt flow distribution and therefore die performance. As a result, die designs that neglect die body deformation may not perform as desired.

The primary focus of most sheet or slit die designs is the development of a uniform velocity across the width of the die exit. Various design approaches have been applied to T-dies, fish-tail dies, and coat-hanger dies in which the cross-section geometry of the distribution manifold is defined over the width of the die to yield a uniform exit velocity [11, 12]. However, in none of the these works was the analysis of the melt flow and pressure field coupled with die body deflection. The closet approach to this seems to have been done by Helmy [61], who used analytical methods, calculating the pressure field and applying this as a distributed load to a beam representing the die body. However, there was no feed back of the modified slit geometry to the pressure field calculation, and this was therefore not a fully coupled analysis.

It is well understood that die body deformation has a strong effect on the design and operation of extrusion dies, but surprisingly, it has received relatively little attention in the literature. Previous work includes a 1D flow analysis and a deformation analysis, but ignored the effect that the melt pressure has on the deformation of die body [61, 62]. More recently, Sander and Pittman [45] developed a fully coupled approach, using a 2.5D Hele-Shaw flow simulation to calculate melt pressure and a 2D thick plate analysis for die deflection. The predicted results agreed closely with experimental data for a die with a relatively simple internal flow channel and die body geometry. However, Sander and Pittman avoided the full 3D analysis and more

complex die geometry "because of their high computational demands" [45]. A 3D flow analysis coupled with a full 3D die deformation analysis appears in Gifford's work [46]. Unfortunately, this earlier approach required specialized software to evaluate the polymer flow within the die and to include the effect of die deformations. Furthermore, the computational efforts required to obtain the more accurate 3D solutions can be excessive when used in an iterative design procedures, particularly when applied to detailed industrial designs.

This research considers an optimization-based approach for designing polymer extrusion dies in which the die cavity geometry is computed to minimize the die inlet pressure (P_{in}) while delivering a uniform exit flow rate. The proposed approach enhances previous design methodologies by incorporating the flow analysis and 3D die deformation analysis in the optimization-based design methodology. Die deformation is analyzed in this approach with the general purpose finite element program ABAQUS [63] which is also used to solve the generalized Hele-Shaw flow equation for an isothermal Carreau-Yasuda fluid to obtain the pressure field on the internal surface of the die body. Upon the completion of the coupled fluid-structure interaction analysis, Sequential Quadratic Programming (SQP) in Design Optimization Tools (DOT) [60] is used to solve the optimization problems. An example of a coat-hanger die is provided to demonstrate the proposed methodology.

3.2 Melt Flow Governing Equation

The Hele-Shaw flow model may be derived from the principles of conservation of mass, momentum and energy to provide a simplified governing equation for non-Newtonian and inelastic flows in thin cavities [42]. In this analysis, inertial, body and surface tension forces in the fluid are assumed to be negligible. Moreover, the pressure does not vary significantly in the direction normal to the plane of flow, and the die cavity thickness is assumed to be small in comparison with its in-plane dimensions and has little in-plane variation, and all flow conditions are assumed to be symmetric with respect to the cavity mid-plane. The Hele-Shaw model is widely employed in injection and compression molding [21], and has also been applied to sheet extrusion dies [5, 17, 22, 39, 41, 52, 53].

On the basis of these assumptions, the mass and momentum conservation equations reduce to a single differential equation [21]

$$\boldsymbol{\nabla} \cdot S \, \boldsymbol{\nabla} P = 0 \tag{3.1}$$

as shown in equation 2.3. This study employs the Carreau-Yasuda fluid model to define the non-Newtonian dependence of η on $\dot{\gamma}$. The Carreau-Yasuda model exhibits near-Newtonian behavior at low strain rates, and captures the power-law decay in η as the strain rate increases. It can be written as follows [3]

$$\eta = \eta_\infty + (\eta_0 - \eta_\infty) \left[1 + (\lambda \dot{\gamma})^a \right]^{(n-1)/a} \tag{3.2}$$

where η_0 is the zero-shear-rate viscosity, η_∞ is the infinite-shear-rate viscosity, λ is a time constant, n is the power-law index, and a is an empirically derived material

constant. $\eta_\infty = 0$ and $a = 2$ are typical for polymer melt [64]. The flow conductance S (see e.g., equation 2.4) cannot be evaluated analytically when the Carreau-Yasuda fluid model is employed. The analysis is further complicated because η, defined in equation 3.2, is a function of $\dot\gamma$ through equation 2.5 in the generalized Hele-Shaw formulation. To solve the example to follow, we evaluate S in equation 2.4 numerically with an eight-point Gaussian Quadrature, for which η, defined through equations 2.5 and 3.2, is computed at a given value of z with a local Newton-Raphson iteration, as described elsewhere [5].

The residual, R, for the boundary value problem described in equation 3.1 is obtained via the method of weighted residuals [54] in the usual manner (see e.g., [53]) as

$$R(P) = \int_\Omega \boldsymbol{\nabla} w \cdot S(P) \boldsymbol{\nabla} P \, d\Omega \tag{3.3}$$

where w is an arbitrary weighting function and we have assumed that there is no prescribed flow rate on the boundary of the 2D flow domain, Ω. The tangent operator, $\frac{\partial R}{\partial P}$, acting on the increment, $[\triangle P]$, is obtained by the differentiation of equation 3.3 with respect to P as

$$\frac{\partial R(P)}{\partial P}[\Delta P] = \int_\Omega \boldsymbol{\nabla} w \cdot \left[S(P) \boldsymbol{\nabla}[\Delta P] + \frac{\partial S(P)}{\partial P}[\Delta P] \boldsymbol{\nabla} P \right] d\Omega \tag{3.4}$$

where equation 2.4 is differentiated to obtain

$$\frac{\partial S}{\partial P}[\Delta P] = -\int_0^h \frac{z^2}{\eta^2} \frac{\partial \eta}{\partial P}[\Delta P] \, dz \tag{3.5}$$

Furthermore, equations 2.5 and 3.2 are differentiated with respect to P, and following some mathematical manipulations, we obtain $\frac{\partial \eta}{\partial P}$ appearing in equation 3.5 (cf. table

56

2.2)

$$\frac{\partial \eta}{\partial P}[\Delta P] = \left[\frac{(n-1)(\lambda\dot{\gamma})^2 \, (\eta - \eta_\infty)}{\eta + (\lambda\dot{\gamma})^2 \, (\eta_\infty + n \, (\eta - \eta_\infty))} \right] \eta \frac{\boldsymbol{\nabla} P \cdot \boldsymbol{\nabla}[\Delta P]}{\|\boldsymbol{\nabla} P\|^2} \tag{3.6}$$

The isoparametric finite element method (see e.g., [54]) may be used to discretize the residual and tangent operator in equations 3.3 and 3.4, respectively, and related terms from equations 3.5 and 3.6. The detailed derivations are given in chapters 2.3.1 and 2.3.2, and are ignored here for conciseness. Once the residual and tangent matrix are evaluated with the finite element method, the nodal pressure vector increment, $\Delta\mathbf{P}$, is computed at iteration $\mathbf{I}$ with the Newton-Raphson method via equation 2.8. The nodal pressures are updated as $\mathbf{P_{I+1}} = \mathbf{P_I} + \Delta\mathbf{P}$. Iterations are repeated until convergence is reached. Once the pressure solution is obtained, the gap-wise average velocity, $\bar{v}$, is computed from equation 2.9.

In this work, equations 3.3 and 3.4 are discretized with the Galerkin finite element method and then solved with the general purpose finite element program ABAQUS with a user-defined element (UEL) [63]. The pressure P within the die cavity is computed at each node with Newton Raphson iterations.

3.3 Coupled Analysis with Fluid-Structure Interaction

It is clear that for a proper simulation of the die design, it is necessary to couple the analysis of the flow distribution and pressure field in the die cavity with the analysis of the die body deformation. Indeed, the high internal pressure within the melt flow causes die deformation, which, in turn, alters the pressure field. Figure 3.1 illustrates

the iterative computational methodology used to solve the coupled fluid-structure analysis. The coupled analysis loop starts with the initialization of pressures and nodal heights. These values are included in an input file of a user-defined element subroutine (UEL) to calculate the nodal pressure solution. To better serve the 3D simulation in the finite element program, the nodal pressures are translated into surface pressures. The resulting surface pressures are then interpolated onto the mesh surface of the die's internal channel, and the linear elastic deformation of the die is calculated, corresponding to those pressure loads.

The deformation caused by the melt pressure forces the die channel to open; thus, the new and deformed heights of the flow channel are generated. The newly generated heights are then interpolated back to the Hele-Shaw model to recalculate the pressure solution. As the die flow channel opens, the change in pressure in the die between iterations will decrease, reducing the tendency of further deformation [46]. The iterative loop presented here normally takes three or four iterations to converge in our example, as shown in figure 3.2. To reduce the computational time, an automatic algorithm is developed in this work to compute the coupled pressure solutions and die deformation, and the overall simulation based on this automatic algorithm can run on a personal computer with only a few minutes of calculation.
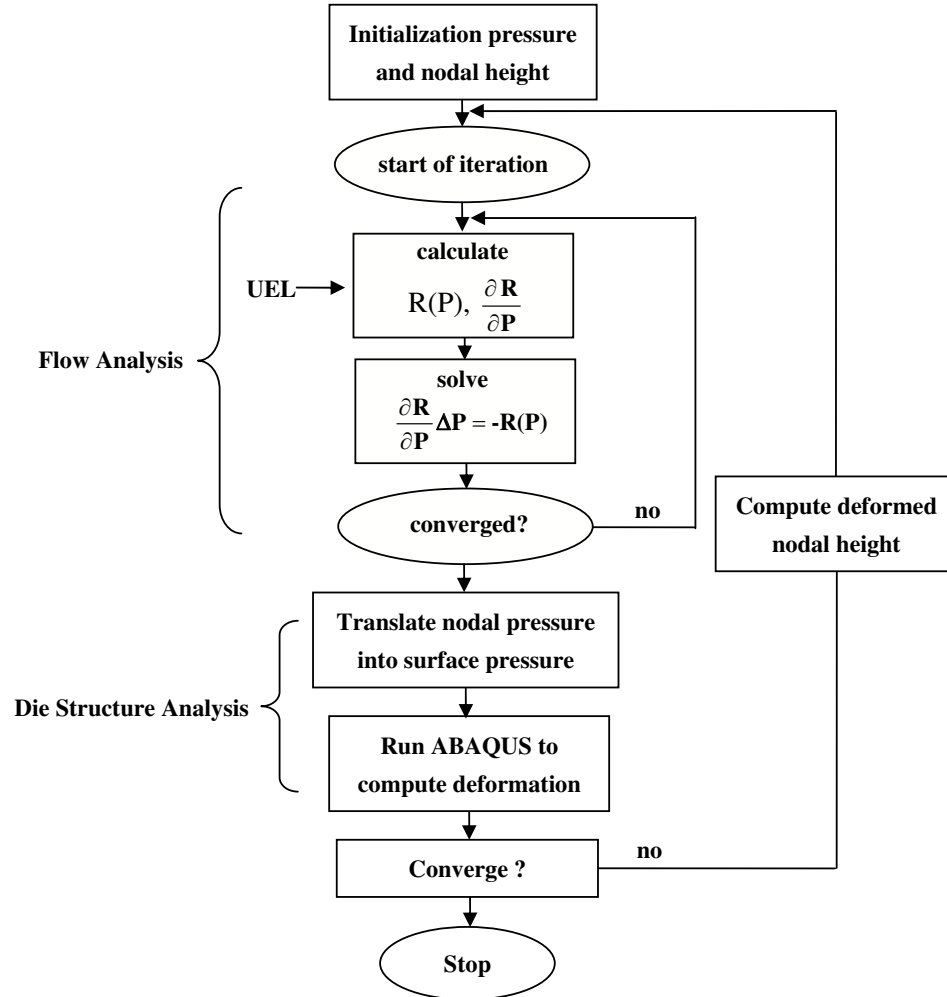
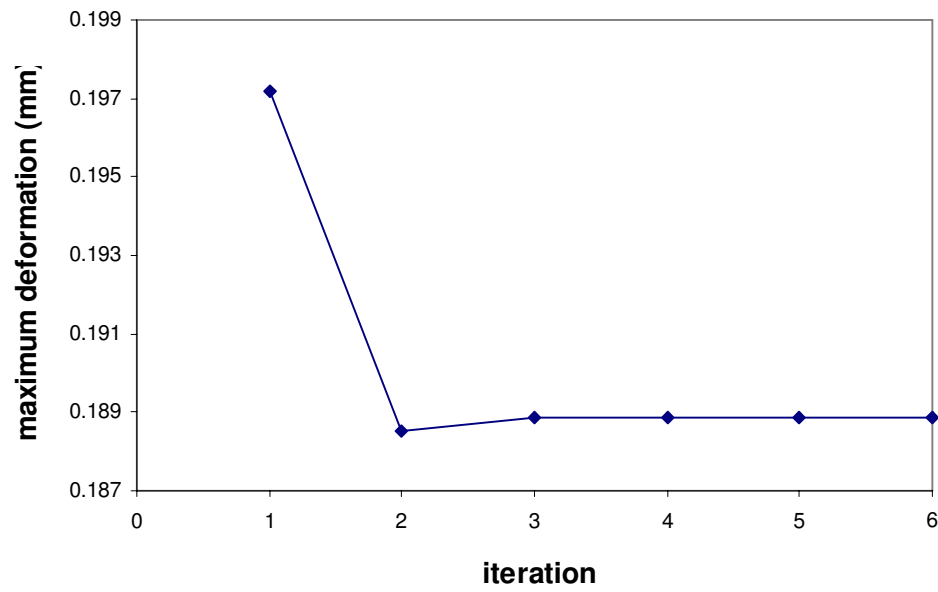Figure 3.1: Computational procedure for the coupled fluid-structure analysis

Figure 3.2: Typical iteration history of the maximum deformation of the die body

3.4   Coat Hanger Die Flow and Deformation Example

The sheeting die design considered in this research is derived from the coat hanger die, which is commonly used in industrial applications and widely studied and tested experimentally [4, 5, 53]. The specific die geometry used in this study is shown in figure 2.3; it is symmetric about the die's centerline (i.e., $x = 0$) and is similar to that presented elsewhere by Gifford [25]. It consists of four major regions, as shown in figure 2.3: the manifold, preland, secondary manifold, and the land. The purpose of the manifold is to distribute the polymer melt uniformly across the die. The secondary manifold and the land each have a uniform cavity half-height and act as a resistance to the flow, which provides better flow uniformity [64].

The land defines the thickness of the polymer melt immediately exiting the die. The dimensions that define our die cavity geometry are taken from table 1 of Gifford [25], except for the land gap, which is fixed at 1.6 mm (i.e., die exit half-height $h_{exit} = 0.8$ mm) for the initial design in this research. The total die exit width is 1016 mm, which results in an exit width-to-height aspect ratio of 635. The die inlet gap and width are 19.05 and 101.6 mm, respectively, and the total die length (including the inlet channel) is 330 mm which includes the 137 mm long inlet channel. The land, secondary manifold, and preland lengths along the die centerline are 25.4, 50.8 and 50.8 mm, respectively. There is a flow channel along the top of the die in the manifold region, which has a uniform half-height in the y-direction and a centerline length of 15.2 mm. The manifold also includes a region having a centerline length of

50.8 mm with a half-height that decreases linearly in the y-direction between the flow channel and the die preland. For illustration, the finite element mesh in figure 3.3 represents the entire flow domain, in which the flow channel is modeled with three-node triangular elements; however, all of the calculations to follow are performed with a half-symmetry model in $x \geq 0$ (not shown) having 853 nodes and 1558 elements.

The flow of low density polyethylene (LDPE) at 270^0C is selected at which material constant $\eta_0 = 800$ Pa-s, $\eta_\infty = 0$, $\lambda = 0.02129$ s, $n = 0.45958$, and $a = 2$ are taken from Gifford [46]. The die inlet pressure P_{in} is defined as 10 MPa, whereas the outlet is defined as zero pressure along die exit. The cavity thickness is defined at each node. The die body geometry is determined by the parameters listed in table 1 of Gifford [46]. The die is assumed to be constructed of carbon steel with a Young's modulus of 2.068×10^{11} Pa and a Poisson's ratio of 0.3. Figure 3.4 shows the finite element mesh of one half of the die body with $109,060$ elements containing $24,072$ nodes. The coat hanger die used here has two planes of symmetry. Therefore, we only consider one quadrant of the die in the structural analysis. The boundary conditions in the plane of flow are $P = P_{in}$ and $P = 0$ at the die inlet and exit, respectively. The boundary conditions for the die body structural model are defined as $U_y = 0$ on the entire back side face (i.e., the side where the flow inlet is located, as shown in figure 3.4), $U_x = 0$ on the $x = 0$ face and $U_y = 0$ on the $y = 0$ face.

Figure 3.5 shows the deformed die body geometry after the convergence is reached. Because of the plane of symmetry, only a quarter of the die body geometry is shown in figure 3.5. The highest deformation occurs at the center position of the die exit,
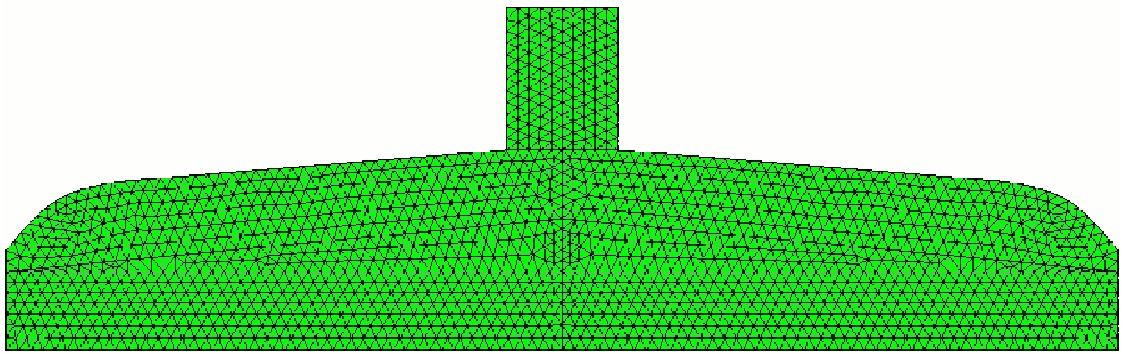
Figure 3.3: Finite element mesh of polymer melt flow domain

at which the die cavity half-height h is increased by 23.6% from 0.8 mm to 0.989 mm. The pressure distributions in the die for the undeformed and deformed die body are shown in figures 3.6(a) and 3.6(b), respectively. As expected, when the die deformation is included in the simulation, the pressure distribution across the die will change such that the pressure decreases in the die as the die flow channel opens up. Additionally, pressure isobars along the die exit region for the undeformed die body are more uniform than those for the deformed die body. This is because the largest deformation occurs at the center position of the die exit, causing the lower pressure at the center and higher pressure at the edge of the die exit.

Figure 3.4: Half symmetry of finite element mesh of the undeformed die body

Figure 3.5: Displacement magnitude of die body (deformation scale factor: 336)

(a) undeformed die body

(b) deformed die body

Figure 3.6: Pressure distribution in the die cavity

3.5 Sheeting Die Design Optimization

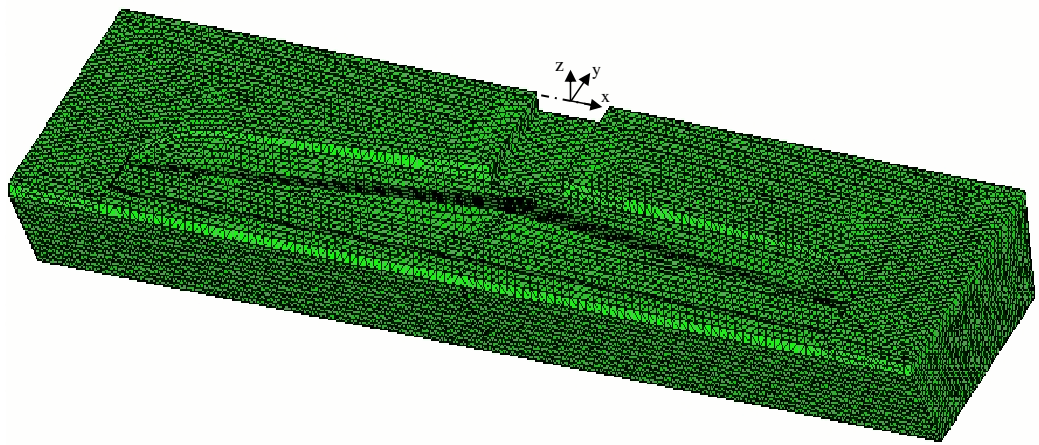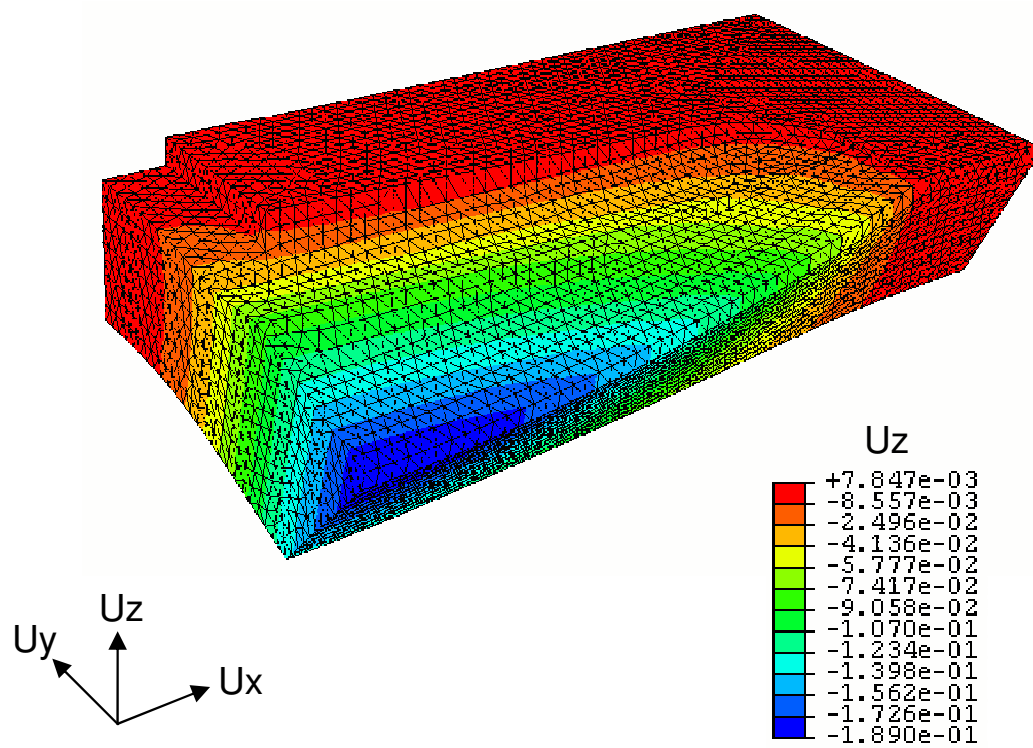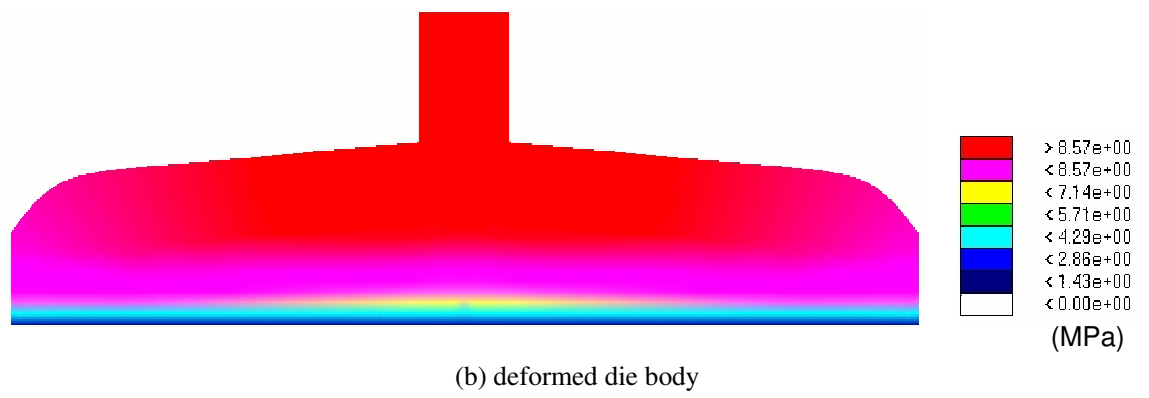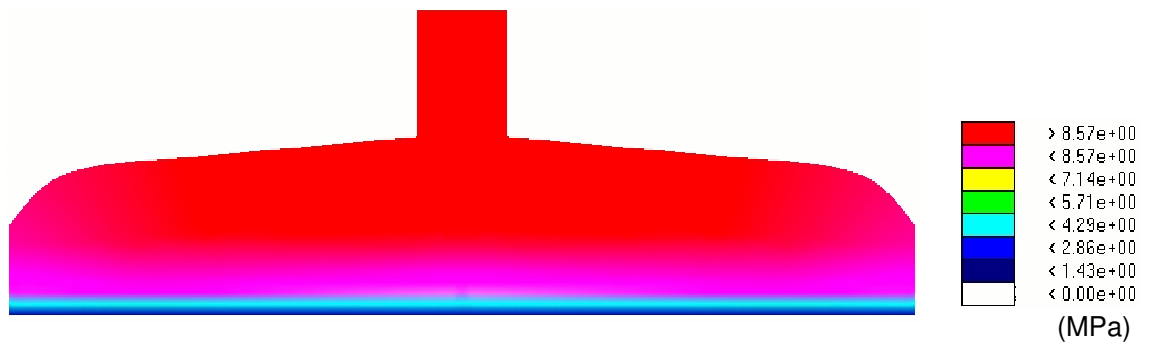In the die design optimization problem considered in this study, the pressure drop across the die and the die exit flow rate variation define the success of a given die design. These criteria are chosen because the pressure drop determines the extruder size and power requirements, and die exit flow rate variation influences the sheet thickness uniformity. The goal of minimizing the inlet pressure P_{in} can be realized by the variation of the thickness distribution in the die cavity, while placing a constraint on die exit flow rate variation and limiting the slope of die cavity surface in the manifold region. The nonlinear constrained die design optimization problem can be stated in terms of the design variable vector, $\boldsymbol{\phi}$, as

$$
\begin{array}{ll}
\text{Determine} & \boldsymbol{\phi} \\[2ex]
\text{Such that} & g_1(\boldsymbol{\phi}) = \frac{1}{L} \int_{l_{exit}} \left(\frac{q(x,\boldsymbol{\phi})}{q_P} - 1 \right)^2 dx \leq \epsilon \\[2ex]
& g_2(\boldsymbol{\phi}) = \text{Max} \left(\frac{dh(x)}{dx} \right) \leq 0 \\[2ex]
& \phi_i^L \leq \phi_i \leq \phi_i^U
\end{array}
\tag{3.7}
$$

where l_{exit} denotes the die exit edge. P_{in} is minimized. This cost function represents the pressure drop through the die because we fix the outlet pressure (P_{out}) at 0. Constraint function g_1 measures the exit flow rate variation and is imposed to obtain a uniform exit flow rate within the tolerance, ϵ. In g_1, $q(x,\boldsymbol{\phi})$ is the exit flow rate per unit of width, and q_P is the desired exit flow rate per unit of width. When $q(x,\boldsymbol{\phi})$ equals q_P across the entire die exit, the die is operating at the desired total flow rate,

Q, which is determined as

$$Q = 2 \int_{l_{exit}} q(x, \boldsymbol{\phi}) dx \qquad (3.8)$$

In the manifold region of the die cavity, the half-height parameter, $h(x)$, is arbitrary, so the constraint function g_2 is imposed to restrict the slope of h in the x direction to less than zero. In the aforementioned optimization problem, $\boldsymbol{\phi}$ is the design variable vector with real components ϕ_i ($i = 1, 2, \ldots N$, where N is the total number of design variables), limited by upper and lower bounds ϕ_i^U and ϕ_i^L, respectively. In addition, the die cavity half-height h in the flow channel is constrained to decrease along the centerline of the die.

3.6   Coat Hanger Die Design Example

In this example, the sheeting die design problem described above has $N = 7$ design variables that are included in the design variable vector $\boldsymbol{\phi}$. P_{in} is defined by the design as $P_{in} = \phi_1$ and is bounded by 1.0 MPa $\leq P_{in} \leq$ 20 MPa. In addition, the half-heights in the preland, manifold and secondary manifold regions shown in figure 2.3 are defined by the remaining 6 design variables. The half-height in the preland region is defined as a constant, ϕ_2. h in the manifold flow channel along the top of the die is defined by the Lagrange interpolating polynomial in x as

$$h(x) = \frac{(x - L/2)(x - L)}{L^2/2} h_0 + \frac{x(x - L)}{-L^2/4} \phi_3 + \frac{x(x - L/2)}{L^2/2} \phi_4 \qquad (3.9)$$

where $L = 508$ mm is the die half-width and h_0 is the die half-height at $x = 0$. Design variables ϕ_3 and ϕ_4 in equation 3.9 are the manifold half-heights at $x = L/2$

and $x = L$, respectively. The slope of h in the manifold region of the die cavity is evaluated from equation 3.9 as

$$\frac{dh(x)}{dx} = \frac{2x - 1.5L}{L^2/2}h_0 + \frac{2x - L}{-L^2/4}\phi_3 + \frac{2x - L/2}{L^2/2}\phi_4 \qquad (3.10)$$

which is constrained by g_2 in equation 3.7. h in the secondary manifold region is defined by a cubic polynomial as

$$h(x) = \phi_5 + (-7.0\phi_5 + 8.0\phi_6 - \phi_7)\left(\frac{x}{L}\right)^2 + (6.0\phi_5 - 8.0\phi_6 + 2.0\phi_7)\left(\frac{x}{L}\right)^3 \quad (3.11)$$

where $\frac{dh}{dx} = 0$ is imposed at $x = 0$. In equation 3.11, the design variables ϕ_5, ϕ_6, and ϕ_7 are the secondary manifold half-height at $x = 0$, $x = L/2$, and $x = L$, respectively. The secondary manifold region can be treated as a choker bar for which $h(x, y)$ can be adjusted independently; this assumes that an operator, or perhaps an automatic control device, can make an adjustment for flow condition considered to facilitate the optimal die flow operation. All half-height design variables are bounded by 1.0 mm $\leq \phi_k \leq$ 19.05 mm $(k = 2, 3 \ldots N)$ in the die optimization problem. The desired exit flow rate per unit of width is $q = 350$ mm^2/s for the flow condition considered in equation 3.7. Also, the exit flow rate tolerance for constraint g_1 in equation 3.7 is defined as $\epsilon = 0.0015$.

The computational procedure of die design optimization is shown in figure 3.7, which includes the coupled fluid-structure interaction in the die design problem. Starting with initial values of the design variables, the computer program calculates the pressure and dies cavity half-height in a coupled analysis. The values of the

deformed die cavity half-heights are compared with the previous values until conver-

gence is reached. Upon completion of the coupled fluid-structure analysis loop, a new

design variable, ϕ, is computed using the DOT SQP algorithm [60]. The design sen-

sitivity is evaluated via the *forward finite-difference* method (see e.g., [54, 65] for the

mathematical equation of *finite-difference* method), and is computed in DOT with a

user-defined parameter for $\Delta\phi_i$.

3.7   Results and Discussion

A new design has been computed with the DOT SQP algorithm [60] in 19 optimization

iterations with gradients computed via the forward finite difference approximation.

The optimization results for the die design are summarized in table 3.1. The optimal

history for the inlet pressure P_{in} appears in figure 3.8(a), and the value of constraint

g_1 in equation 3.7 is shown in figure 3.8(b) at each optimization iteration. In these

calculations, the pressure drop decreases from 10 to 6.57 MPa, a 34.3% reduction,

whereas the exit flow rate constraint, g_1, is reduced considerably from its initial value

of 1.34 to its optimal value of 0.00013, which is well below the tolerance ϵ. Changes

in the design variables are also shown in table 3.1. The uniformity in exit flow rate

is evidenced by the reduction in the difference between the maximum and minimum

gap-wise exit velocity values. Moreover, the optimal average exit flow rate per unit

width is near the desired value of 350 mm^2/s.

The pressure distributions in the mid-plane of the initial and optimal designs are

shown in figure 3.9(a,b), respectively. When the die deformation is included in the
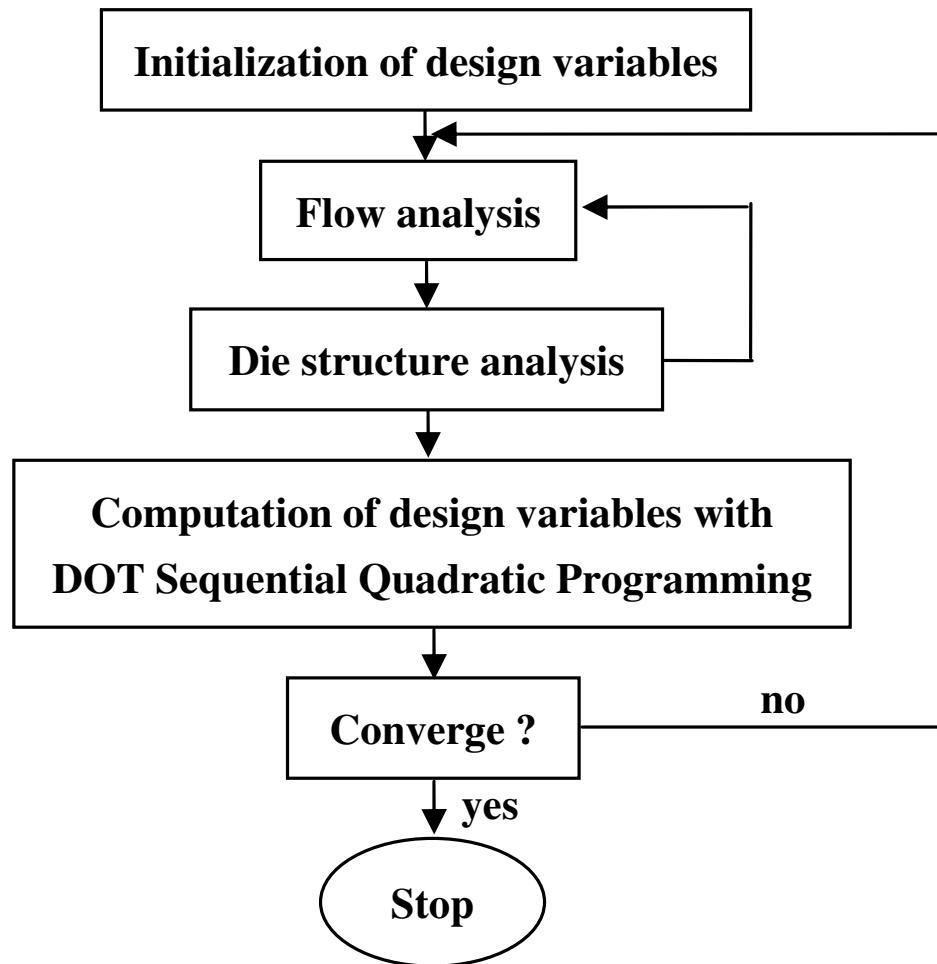
Figure 3.7: Computational procedure of die design optimization

Table 3.1: Initial and optimal design variable and performance measure values

Die Design		Initial	Optimal
Design Variables			
$\phi_1 = P_{in}$ (MPa)		10.0	6.57
ϕ_2 (mm)		3.2	12.64
ϕ_3 (mm)		12.05	18.23
ϕ_4 (mm)		5.2	17.32
ϕ_5 (mm)		3.0	3.08
ϕ_6 (mm)		3.5	3.75
ϕ_7 (mm)		4.0	12.23
Constraint			
g_1		1.34	0.00013
Exit Flow Rate per Unit Width (mm^2/s)			
q_{exit} (ave)		736.0	347.3
q_{exit} (max)		853.6	364.2
q_{exit} (min)		452.2	290.5
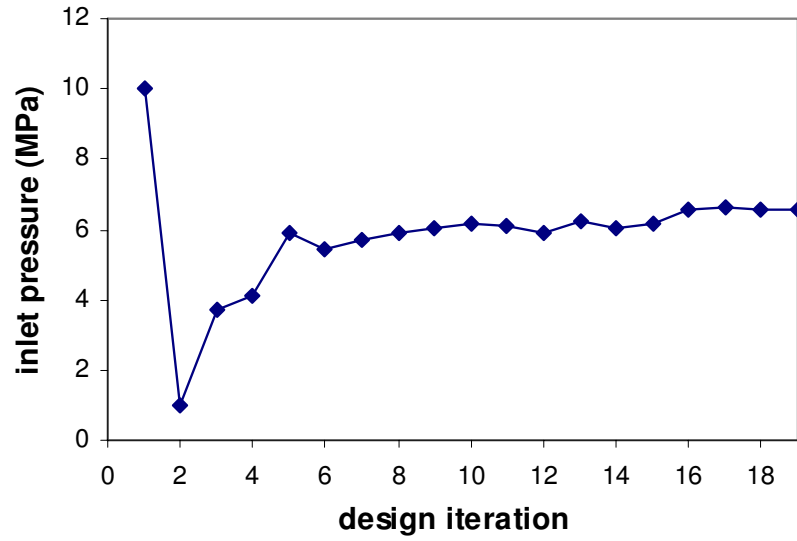
(a) objective function optimization history
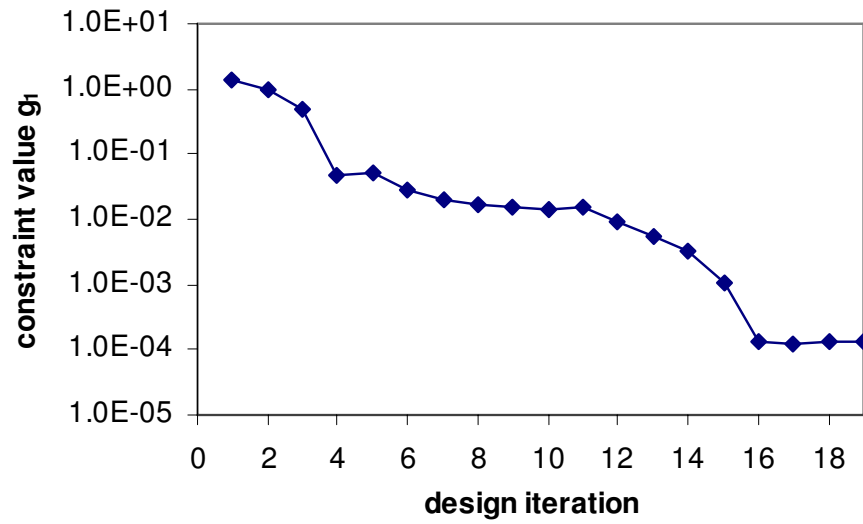
(b) optimization history for exit flow rate constraint

Figure 3.8: Design iteration history for the objective function and exit flow rate constraint

design simulation, the die pressure decreases as the die channel opens up. Since the half-heights along the die exit are no longer uniform because of the gap opening, the pressure isobars will not be parallel to the die exit. As expected, the isobars just inside the die exit of the initial design are more parallel than those of the optimal design, as shown in figure 3.9(a,b), respectively. The die cavity half-heights are presented in figure 3.10(a) for the initial design and in figure 3.10(b) for the optimal design. The gap thickness in the manifold and preland regions of the optimal design are increased in comparison with that of the initial design. The half-height changes can also be seen in the secondary manifold region (i.e., choker bar).

Die exit flow rates are illustrated for the initial and optimal designs in figure 3.11, in which the distance along the die exit is normalized with the exit width. The exit flow rates for the initial design are far from the desired value and show a significantly higher flow rate along the centerline of the die than at its edge. The optimal die design provides a more uniform exit flow rate, which illustrates how well the design approach is able to meet the desired flow rate over the entire width of the die. Figure 3.12 shows the die exit flow rate and velocity distribution for the optimal design and is provided here to illustrate the influence of die deformation on the uniformity of the flow distribution. The exit flow rate is the product of the die exit half-height and velocity. For the uniform exit flow rate, the exit velocity will decrease as the half-height increases. The die exit half-height, which is initially uniform across the die exit, increases more in the center, resulting in a lower velocity than that at the die's outer edge. Compared with the exit velocity distribution, the flow rate is more
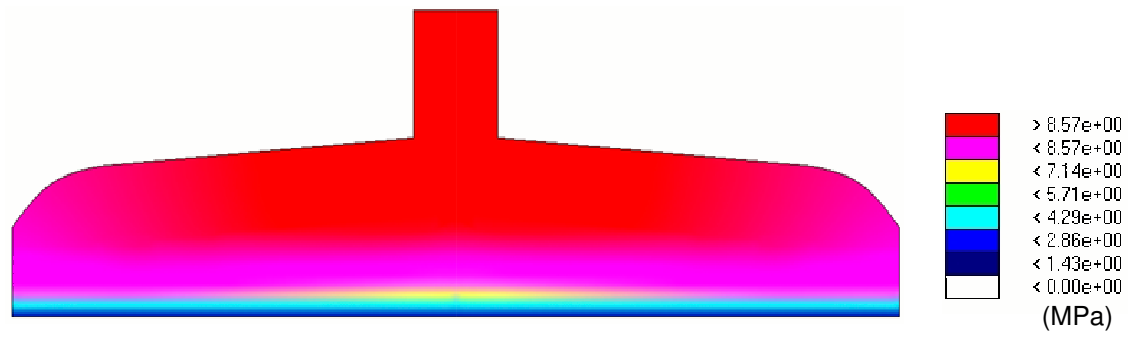
(a) initial pressure distribution
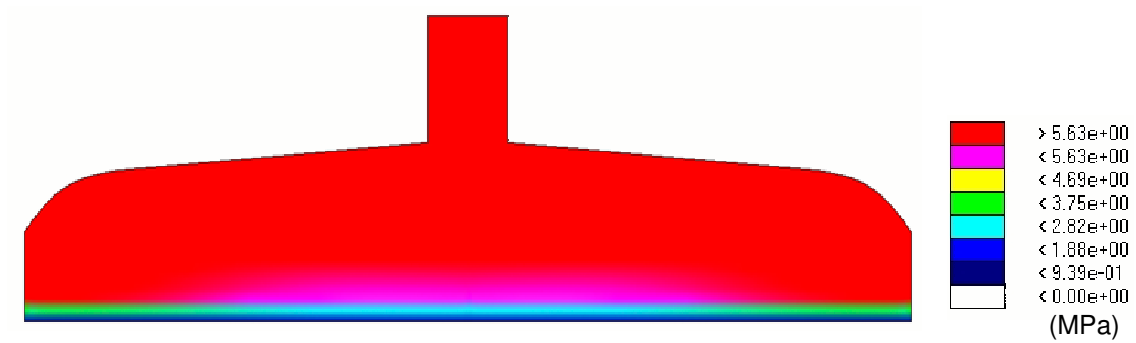
(b) optimal pressure distribution

Figure 3.9: Pressure distribution in the die cavity

(a) initial half-height distribution

(b) optimal half-height distribution
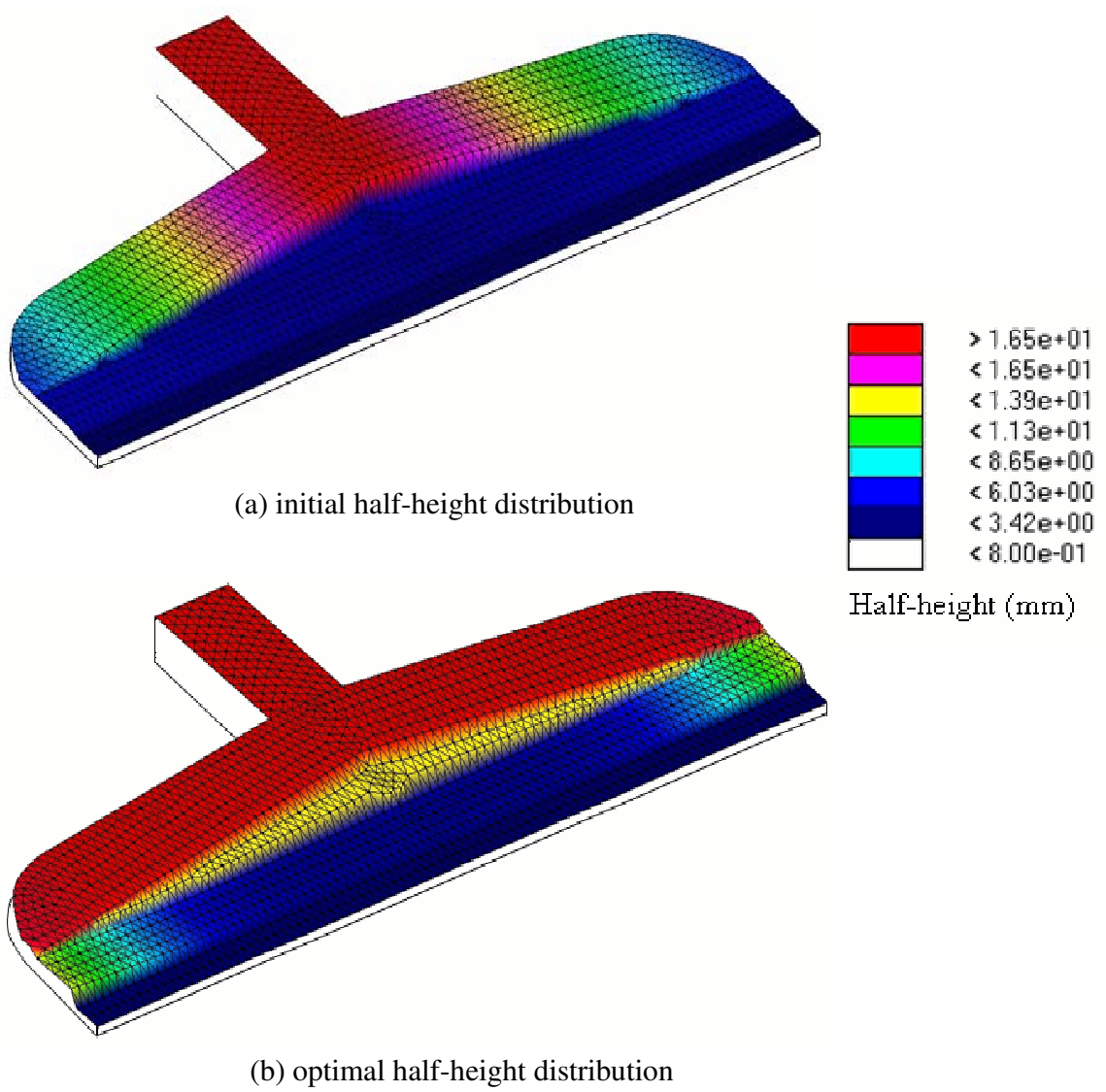
Figure 3.10: Die cavity half-height distributions

uniform. As can be seen in the plot, the optimal design generates a nearly uniform flow rate distribution at the die exit.

3.8 Summary

An optimization-based polymer sheeting die design methodology has been described that couples an isothermal Hele-Shaw pressure field/flow analysis with die deformation analysis, taking into account the interaction of internal pressure, flow distribution, and die deformation. The performance measures in the optimization have been evaluated with a coupled flow analysis and 3D simulation of die deformation. In this approach, sheeting dies are analyzed with a general purpose finite element program, in which a user element program is developed to evaluate the purely viscous non-Newtonian flow in a die. An automatic algorithm to calculate the coupled pressure and die deformation has been presented, and a sheeting die design optimization problem has illustrated the design approach.
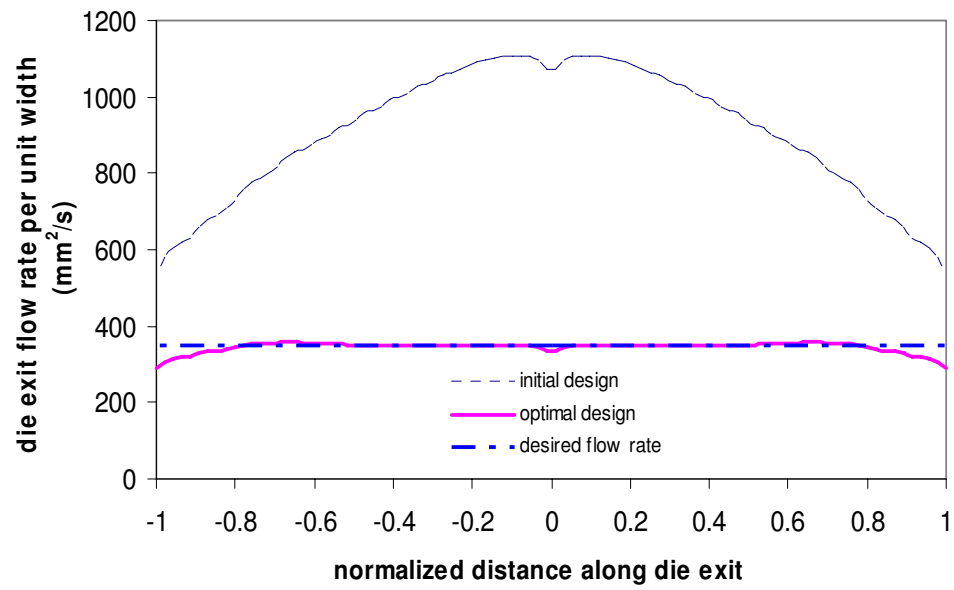
Figure 3.11: Exit flow rate for coat hanger die design
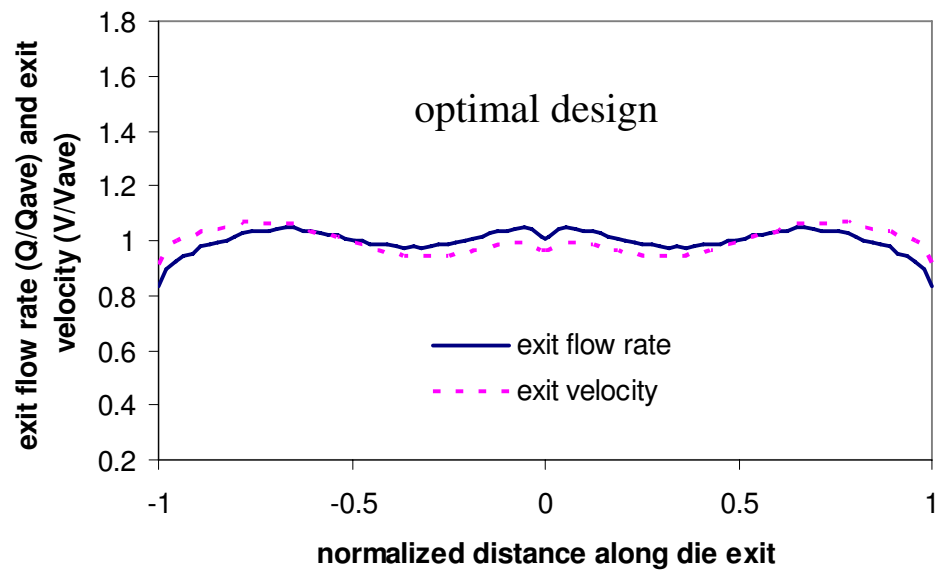
Figure 3.12: Effect of die deformation on the exit flow distribution

CHAPTER 4

NON-ISOTHERMAL ANALYSIS: FULLY-COUPLED NONLINEAR STEADY-STATE TEMPERATURE AND PRESSURE SYSTEMS

The simulation of the extrusion and mold filling processes for molten polymers has received considerable attention in the literature [21]. Despite inherent difficulties associated with non-Newtonian, non-isothermal and transient fluid flow, considerable progress has been made during the last decade. A detailed formulation is presented in this work for simulating the extrusion in thin cavities. The modelling incorporates the generalized Hele-Shaw flow approximation for an inelastic, non-Newtonian fluid under non-isothermal conditions. A hybrid numerical scheme is employed in which the pressure solution of 2.5D Hele-Shaw flow is fully coupled with a non-linear 3D energy equation for the calculation of temperature. An iterative procedure is provided to calculate the coupled Hele-Shaw flow approximation and energy equation. In addition, the design sensitivities for fully coupled nonlinear steady-state temperature and pressure systems are derived. To demonstrate the methodology, a sheet extrusion die is designed by incorporating the fully coupled systems in a constrained optimization algorithm to simultaneously minimize the exit velocity variation and the exit temperature variation.

4.1 Background

In recent years, numerous theoretical computations have been developed for the analysis and design of injection and extrusion processes, based on numerical solutions of equations governing flow and heat transfer in two or three dimensions [44, 66–68]. Among these efforts, many studies have been devoted to use finite difference, finite volume, or finite element methods to model complex die geometry more realistically, and to incorporate thermal effects.

Arpin et al. [44] developed a 2D non-isothermal flow model based on a modified FAN method and used the Biot number to allow thermal resistance at the melt-metal interface. They compared the simulation results using two different thermal boundary conditions: an isothermal wall and an adiabatic wall. Indeed, the assumption of a uniform wall temperature appears in other publications as well. One would expect the die wall temperature to vary with position, as a result of thermal interaction between the melt and the die body. The treatment of uniform die wall temperature, however, are only simplification, rather than limitation, of the non-isothermal analysis in die design.

A complete thermal analysis would require a three-dimensional numerical simulation of the conjugate problem of flow and heat transfer in the melt, coupled with conduction in the die body, and taking into account electrical heating and surface heat losses [8]. While this is certainly possible, it is somewhat impractical, because

of the substantial computational demands. Although the flow of the molten polymer in a die is in most cases three-dimensional, it can sometimes be treated as a two-dimensional one, particularly when the flow channel is narrow, that is when the dimension normal to the plane of the flow (the channel depth) is small in comparison with the other two dimensions. As justified by Pittman and Sander [8], if the circumstances in which melt temperature variations are dependent in terms of predictions of pressure drop and flow distribution are not significant, then a computational economical two-dimensional isothermal analysis, based on Hele-Shaw flow, will be adequate. If thermal effects must be taken into account, then one would like to access the formulation of non-isothermal Hele-Shaw flow analysis, for example, the assumption of a uniform channel wall temperature. In the non-isothermal analysis, one would also like to know more about temperature fields in the die body, taking into account the interactions with the flowing melt, with a view to optimizing the location of heaters and control thermocouples, and achieving a design that minimizes melt temperature inhomogeneities [8, 62].

More recently, the finite element method and the Newton-Raphson solution algorithm are combined to solve the momentum, mass and energy conservation equations for coupled thermal and fluid flow problem. Sensitivity analyses have been presented for numerous thermal problems. Haftka [69] and Meric [70] described sensitivity analysis for linear thermal systems, while Tortorelli and co-workers [71, 72] and Dems [73, 74] described an adjoint method for non-linear thermal systems. Direct differentiation approaches for transient, non-linear thermal systems are also presented

in references [73–75]. Sensitivity analyses have also been presented for coupled fluid flow systems. Smith [9, 22, 76] have considered sensitivity analysis for steady-state nonlinear weakly coupled systems and evaluated the material residence time in polymer melts. Michaleris et al. [77] developed a systematic approach for the design of weakly coupled thermoelastoplastic systems and used Newton-Raphson iteration method in the solution process. Wang, Tortorelli and Dantzig [78] presented a systematic approach for computing explicit design sensitivity for transient laminar flows, coupled with the solution of the energy equation.

The present research attempts to provide new insights in these areas using finite element simulations of the coupled melt flow and die body heat transfer problem. The analysis based on 2.5D Hele-Shaw flow evaluates the pressure distribution in the polymer melt which is used to calculate the velocity field. We then substitute the pressure and velocity solutions into the 3D energy equation to compute the melt temperature. Thus, a fully coupled analysis exists between these analyses since the viscosity is temperature dependent and thermal energy is generated via viscous heating. The analysis and sensitivity analysis for fully coupled thermal and flow systems are derived. The tangent operators of the Newton-Raphson solution processes are used to compute sensitivities accurately and efficiently via the adjoint method. The analysis and sensitivity analysis are incorporated into a numerical optimization algorithm to design a polymer sheeting die.

4.2 Modeling and Simulation

4.2.1 Governing Equation

The Hele-Shaw flow in a thin cavity with arbitrary in-plane dimensions for an inelastic non-Newtonian fluid under non-isothermal conditions is governed by conservation equations of mass, momentum, and energy, i.e. [55, 59],

$$\frac{\partial v_x}{\partial x} + \frac{\partial v_y}{\partial y} + \frac{\partial v_z}{\partial z} = 0 \qquad (4.1)$$

$$\rho\left(\frac{\partial v_x}{\partial t} + v_x\frac{\partial v_x}{\partial x} + v_y\frac{\partial v_x}{\partial y} + v_z\frac{\partial v_x}{\partial z}\right) = -\frac{\partial P}{\partial x} + \left(\frac{\partial \tau_{xx}}{\partial x} + \frac{\partial \tau_{yx}}{\partial y} + \frac{\partial \tau_{zx}}{\partial z}\right) + f_x$$

$$\rho\left(\frac{\partial v_y}{\partial t} + v_x\frac{\partial v_y}{\partial x} + v_y\frac{\partial v_y}{\partial y} + v_z\frac{\partial v_y}{\partial z}\right) = -\frac{\partial P}{\partial y} + \left(\frac{\partial \tau_{xy}}{\partial x} + \frac{\partial \tau_{yy}}{\partial y} + \frac{\partial \tau_{zy}}{\partial z}\right) + f_y \quad (4.2)$$

$$\rho\left(\frac{\partial v_z}{\partial t} + v_x\frac{\partial v_z}{\partial x} + v_y\frac{\partial v_z}{\partial y} + v_z\frac{\partial v_z}{\partial z}\right) = -\frac{\partial P}{\partial z} + \left(\frac{\partial \tau_{xz}}{\partial x} + \frac{\partial \tau_{yz}}{\partial y} + \frac{\partial \tau_{zz}}{\partial z}\right) + f_z$$

$$\rho c_p\left(\frac{\partial T}{\partial t} + v_x\frac{\partial T}{\partial x} + v_y\frac{\partial T}{\partial y} + v_z\frac{\partial T}{\partial z}\right) = k\left[\frac{\partial^2 T}{\partial x^2} + \frac{\partial^2 T}{\partial y^2} + \frac{\partial^2 T}{\partial z^2}\right] + \eta\dot{\gamma}^2 \qquad (4.3)$$

where ρ, c_p and k are density, specific heat and thermal conductivity, respectively. P is the pressure, and f is the body force. The viscous stresses in the momentum equation 4.2 are defined in index notation as [55]

$$\tau_{ij} = \eta\dot{\gamma}_{ij} \qquad (4.4)$$

where $\dot{\gamma}$ is the magnitude of the rate of deformation tensor given as

$$\dot{\gamma} = \sqrt{(\dot{\gamma}_{ij}\dot{\gamma}_{ij})/2} \qquad (4.5)$$

where repeated indicies imply summation in the usual manner, and

$$\dot{\gamma}_{ij} = v_{i,j} + v_{j,i} \qquad (4.6)$$

To reflect the non-isothermal influence on the rheological behavior of polymer melt, the temperature-shifting function is introduced. The non-isothermal constitutive equation used here can be expressed as

$$\eta = m \exp\left[\frac{E}{R}\left(\frac{1}{T} - \frac{1}{T_0}\right)\right]\dot{\gamma}^{n-1} \tag{4.7}$$

for non-isothermal power-law fluid model. In the above, E/R is Arrhenius factors. m and n are the consistency index and power-law index, respectively, at the reference temperature T_0.

It is noted that these model equations are based on the following assumptions, (i) viscoelastic effects and inertial, body and surface tension forces are ignored; (ii) uniform pressure and negligible velocity in the direction of die cavity thickness; (iii) thermal convection in the gap-wise direction is ignored; (iv) the following physical properties are considered constant: density, conductivity and specific heat. In addition to the above assumptions, the Peclet number is employed to evaluate the influence of heat convection and conduction to temperature field. The Peclet number is the ratio of heat convection to heat conduction, and is given by

$$Pe = \frac{vD}{\alpha} \tag{4.8}$$

where v is the velocity, D is the characteristic dimension, and α is the thermal diffusivity. In our problem, $Pe = 2.3 \times 10^5$, which means conduction in x and y-direction can be neglected relative to convection. Since the conduction terms $\frac{\partial^2 T}{\partial x^2}$ and $\frac{\partial^2 T}{\partial y^2}$ are negligible in the energy equation 4.3, their presence may not affect the temperature solution. We still keep these two terms in the energy equation to facilitate the

computation of residual that follows.

It is worth noting that, in the Cartesian coordinate system as shown in figure 4.1, the center line is at $z = 0$ and the top and bottom surfaces of the die cavity are at $z = +h$ and $z = -h$, respectively, such that the total die cavity thickness is $2h$. For the thermal boundary conditions, we may have a constant temperature profile at the die entrance and a constant wall temperature T_w. Consistent with the above governing equations, appropriate boundary conditions in the z-direction are given by

$$v_x = v_y = 0 \qquad \text{at} \quad z = h$$

$$\frac{\partial v_x}{\partial z} = \frac{\partial v_y}{\partial z} = \frac{\partial T}{\partial z} = 0 \qquad \text{at} \quad z = 0$$

$$T = T_w \qquad \text{at} \quad z = h \ \ and \ \ x = x_{sidewall} \qquad (4.9)$$

The mass, momentum and energy equations may be simplified according to the above assumptions for the steady-state problem as

$$\frac{\partial v_x}{\partial x} + \frac{\partial v_y}{\partial y} = 0 \qquad (4.10)$$

$$\frac{\partial P}{\partial x} = \frac{\partial}{\partial z}\left(\eta \frac{\partial v_x}{\partial z}\right)$$

$$\frac{\partial P}{\partial y} = \frac{\partial}{\partial z}\left(\eta \frac{\partial v_y}{\partial z}\right) \qquad (4.11)$$

$$\frac{\partial P}{\partial z} = 0$$

$$\rho c_p \left(v_x \frac{\partial T}{\partial x} + v_y \frac{\partial T}{\partial y}\right) = k\nabla^2 T + \eta \dot{\gamma}^2 \qquad (4.12)$$

Based on the Hele-Shaw model assumption for generalized Newtonian fluids, the continuity equation and momentum equation reduce to a differential equation, called Hele-Shaw approximation equation, in pressure P, as shown in equation 2.3.
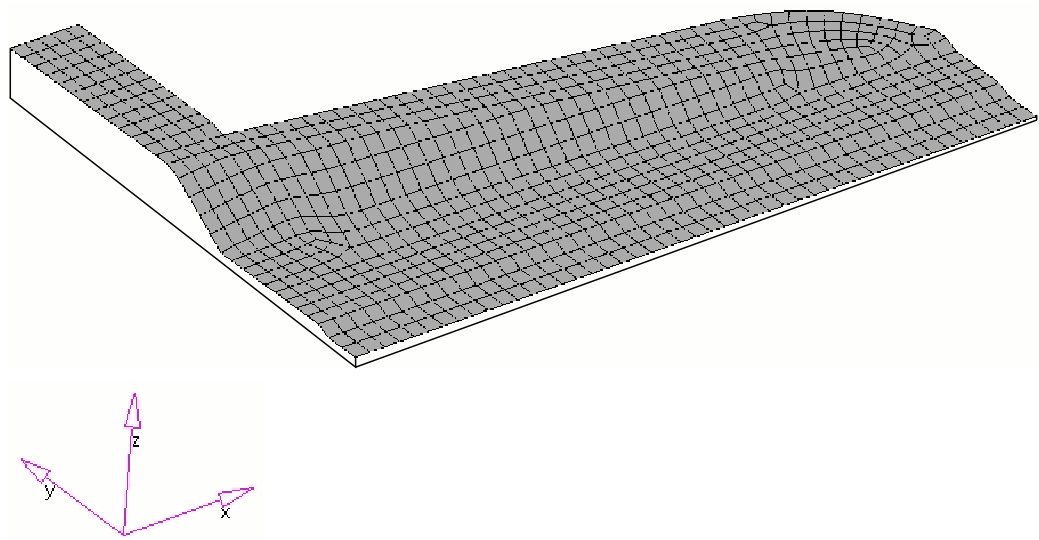
Figure 4.1: One quadrant of coat hanger sheeting die

In the following, a hybrid scheme is employed to solve the coupled energy equation 4.12 and Hele-Shaw approximation equation 2.3. Coupling occurs due to the presence of the velocity v and a shear rate dependent heat source in the energy equation and the inclusion of thermal dependent viscosity in the Hele-Shaw equation.

4.2.2   Model Solution

The solution of the above coupled equations generally require an iterative procedure. A Newtonian-Raphson iteration is used in which the global residual is defined as

$$R(P,T) = \left\{ \begin{array}{c} R^P(P,T) \\ R^T(P,T) \end{array} \right\} = 0 \tag{4.13}$$

The residual R as in equation 4.13, is deemed the global system. Note that the R^P and R^T are the local residuals of pressure and temperature, respectively, and they may be obtained by employing the method of Weighted Residuals and *Gauss's Divergence theorem* over the two dimensional flow domain Ω_2 and three dimensional temperature domain Ω_3, respectively, as [5]

$$R^P(P,T) = \int_{\Omega_2} \boldsymbol{\nabla} w \cdot S(P) \boldsymbol{\nabla} P \, d\Omega_2 - \int_{\partial\Omega_2^q} w \, q^P ds \tag{4.14}$$

and

$$R^T(P,T) = \int_{\Omega_3} \tilde{u} \, \rho \, c_p \, b \, \boldsymbol{\nabla} P \cdot \boldsymbol{\nabla} T \, d\Omega_3 + \int_{\Omega_3} \boldsymbol{\nabla} w \, k \, \boldsymbol{\nabla} T \, d\Omega_3 - \int_{\Omega_3} w \, \eta \, \dot{\gamma}^2 d\Omega_3 \tag{4.15}$$

where

$$b = -\int_z^h \frac{z}{\eta} \, dz \tag{4.16}$$

The boundary conditions in the 2D plane of flow domain are $P = P^p$ on $\partial\Omega_2^p$ and $S(\boldsymbol{\nabla}P \cdot \mathbf{n}) = q^p$ on $\partial\Omega_2^q$ where q^p is the prescribed flow rate, $\mathbf{n}$ is the outward

89

unit normal to the boundary $\partial\Omega_2$. The Streamline Upwind Petrov-Galerkin (SUPG) method proposed by Brooks and Hughes [49] is employed to compute the residual R^T. It is seen from equation 4.15 that the streamline upwind modification does not affect the weighting of the diffusion and viscous dissipation terms. The SUPG method provides a physically realistic and spatially stable alternative to the Galerkin finite element, and numerous examples demonstrate the effectiveness of the SUPG method in convection dominated flow analyses [49, 79–81]. Details of the SUPG method are provided elsewhere, see e.g., [49, 81]. Here, the discussion is limited to the details required for the residual calculation.

In the SUPG method, the weighting function $\tilde{u}(P; w)$ of equation 4.15 is given as [79]

$$\tilde{u}(P; w) = w + \frac{\alpha\, d_e(P)}{2\|\mathbf{v}(P)\|} \boldsymbol{\nabla} \cdot (w\, \mathbf{v}(P)) \tag{4.17}$$

where w is the standard Galerkin weighting function [81], d_e is the characteristic element length, and α is a scaling parameter analogous to an artificial diffusivity. Here we emphasize the dependence of $\tilde{u}$ on the pressure field P. The weighting function $\tilde{u}$ adds a highly anisotropic artificial diffusion which attains its maximum value in the flow direction and is zero in the direction normal to the flow direction [81]. We choose the characteristic element length d_e as the element length in the velocity direction and hence it is also a function of the pressure field (since $\mathbf{v}$ is a function of P (cf. equation 2.9)). See appendix A for the evaluation of d_e for isoparametric elements.

4.2.3 Finite Element Discretization

The isoparametric Streamline Upwind Petrov-Galerkin (SUPG) method is also used to discretize equation 4.12 over the 3D flow domain Ω_3. The flow domain Ω_3 in equation 4.12 is divided into multiple finite element domain Ω_{3k}. The domain discretization provides a means for the purpose of numerically evaluating the integral in the expression above. As is common in finite element methods, we use Gauss-Legendre Quadrature to numerically evaluate the required integrals.

In each element domain Ω_k, the pressure P, temperature T and weighting function $\tilde{u}$ are defined as

$$P(x, y) = \mathbf{N^P}(\xi, \eta) \overset{n}{\mathbf{P}} \tag{4.18}$$

$$T(x, y, z) = \mathbf{N^T}(\xi, \eta, \zeta) \overset{n}{\mathbf{T}} \tag{4.19}$$

$$\tilde{u}(x, y, z) = \mathbf{N^T}(\xi, \eta, \zeta) \overset{n}{\mathbf{u}} \tag{4.20}$$

where $\mathbf{N^P}(\xi, \eta)$ and $\mathbf{N^T}(\xi, \eta, \zeta)$ are the element interpolation(shape) function matrix for pressure and temperature, respectively. $\overset{n}{\mathbf{P}}$ is the element nodal pressure vector, $\overset{n}{\mathbf{T}}$ is the element nodal temperature vector, and $\overset{n}{\mathbf{u}}$ is a vector of SUPG nodal weights. The transformation between the reference domain and actual domain is characterized by the Jacobian matrix $\mathbf{J}$ as

$$\mathbf{J}(\boldsymbol{\xi}) = \frac{\partial \mathbf{N}}{\partial \boldsymbol{\xi}} \overset{n}{\mathbf{X}} \tag{4.21}$$

where $\frac{\partial \mathbf{N}}{\partial \xi}$ denotes differentiation with respect to the reference coordinate in the parent element.

It can be shown that the gradient ∇P and ∇T in equation 4.15 are computed as

$$\nabla P = \mathbf{B_2^P} \overset{n}{\mathbf{P}}$$

$$\nabla T = \mathbf{B_3^T} \overset{n}{\mathbf{T}} \tag{4.22}$$

where the element gradient matrices are

$$\mathbf{B_2^P} = \mathbf{J_2^{-T}} \frac{\partial \mathbf{N^P}}{\partial \boldsymbol{\xi}}$$

$$\mathbf{B_3^T} = \mathbf{J_3^{-T}} \frac{\partial \mathbf{N^T}}{\partial \boldsymbol{\xi}} \tag{4.23}$$

Here we use $\mathbf{B_2^P}$ and $\mathbf{B_3^T}$ in the 2D pressure and 3D temperature solution, respectively. For conciseness, $\mathbf{B_2}$ and $\mathbf{B_3}$ are used in the rest of this chapter. Similarly, $\mathbf{J_2}$ and $\mathbf{J_3}$ are Jacobian matrices of 2D pressure and 3D temperature solution, respectively. The area $d\Omega_2$ in each element domain may be expressed in terms of the reference area $d\Omega_{2k}$, as

$$d\Omega_2 = J_2 \, d\Omega_{2k} \tag{4.24}$$

where $J_2 = det(\mathbf{J_2})$.

Substituting the above finite element expression in the residual equation 4.14, we obtain

$$\mathbf{R^P}(\mathbf{P}, \mathbf{T}) = \int_{\Omega_{2k}} [\mathbf{B_2^T} \, S(\mathbf{P}, \mathbf{T}) \, \mathbf{B_2} \overset{n}{\mathbf{P}}] \, J_2 \, d\Omega_{2k} - \int_{\partial\Omega_{2k}} \mathbf{N^T} \, q^P j_2 \, ds_k \tag{4.25}$$

where $j_2 = J_2 \, \|\mathbf{J_2^{-T}} \, \mathbf{n}_k\|$ which is called the surface area metric and $\mathbf{n}_k$ is the outward unit normal vector to the reference element boundary.

Similarly, the residual $\mathbf{R^T}(\mathbf{P}, \mathbf{T})$ may be evaluated with the finite element method as

$$\mathbf{R^T}(\mathbf{P}, \mathbf{T}) = \int_{\Omega_{3k}} \mathbf{N}^T \rho c_p \, b \, \mathbf{B}_3 \overset{\text{n}}{\mathbf{P}} \cdot \mathbf{B}_3 \overset{\text{n}}{\mathbf{T}} \, J_3 d\Omega_{3k} + \int_{\Omega_{3k}} \left(\frac{\alpha d_e}{2\|\mathbf{v}\|} \mathbf{B}_3^T \mathbf{v} \right) \rho c_p \, b \, \mathbf{B}_3 \overset{\text{n}}{\mathbf{P}} \cdot \mathbf{B}_3 \overset{\text{n}}{\mathbf{T}} \, J_3 d\Omega_{3k}$$
$$+ \int_{\Omega_{3k}} \mathbf{B}_3^T \, k \, \mathbf{B}_3 \overset{\text{n}}{\mathbf{T}} \, J_3 d\Omega_{3k} - \int_{\Omega_{3k}} \mathbf{N}^T \eta \dot{\gamma}^2 \, J_3 d\Omega_{3k} \qquad (4.26)$$

By means of Gauss-Legendre Quadrature, we evaluate the above integral with appropriate location and weights. A Newtonian-Raphson iteration is used, as shown in figure 4.2, to compute the coupled pressure and temperature solutions. Starting with initial values of pressure and temperature, the Hele-Shaw approximation equation for die cavity pressure is solved using the Newton-Raphson iteration method. The resulting pressure and velocity solutions are then substituted into the energy equation and the Newton-Raphson method is used again to compute the melt temperature. The newly generated temperature solutions are compared to the previous values and the coupled analysis repeats until the convergence is reached. In this analysis, the coupled pressure and temperature solutions take 9 iterations to converge.

Suppose we have an existing guess for the solutions of the above, say $\mathbf{P^I}$ and $\mathbf{T^I}$, which do not satisfy equation 4.13. The objective then, is to determine the appropriate changes, i.e. the $\Delta\mathbf{P}$ and $\Delta\mathbf{T}$, which when added to the current solution guess, will satisfy the above equation. To this end, we perform a first-order Taylor series expansion about the current solution which gives [50]

$$\frac{\partial \mathbf{R^P}(\mathbf{P}, \mathbf{T})}{\partial \mathbf{P}} \Delta\mathbf{P} = -\mathbf{R^P}(\mathbf{P}, \mathbf{T})$$
$$\frac{\partial \mathbf{R^T}(\mathbf{P}, \mathbf{T})}{\partial \mathbf{T}} \Delta\mathbf{T} = -\mathbf{R^T}(\mathbf{P}, \mathbf{T}) \qquad (4.27)$$
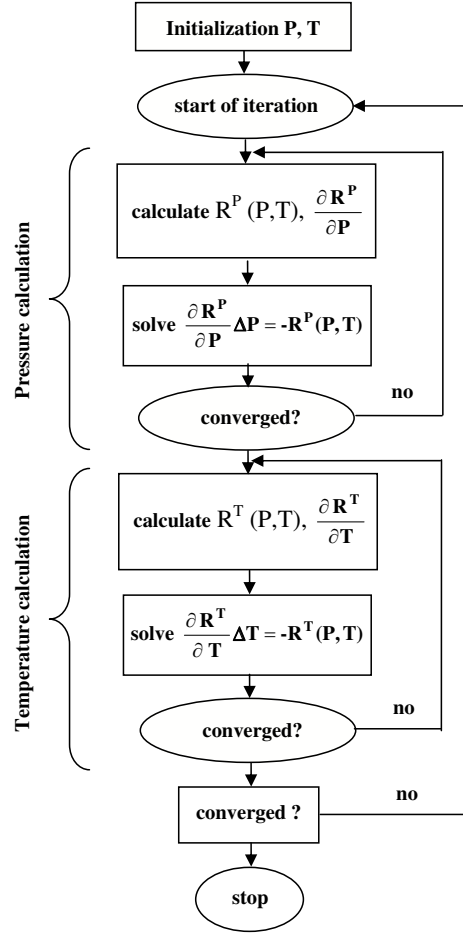
Figure 4.2: Computational procedure of the coupled pressure and temperature solution

here we assume that $\frac{\partial R^P(P,T)}{\partial P} \approx \mathbf{w}^T \frac{\partial \mathbf{R^P(P,T)}}{\partial \mathbf{P}}$, so that the tangent stiffness matrix $\frac{\partial \mathbf{R^P(P,T)}}{\partial \mathbf{P}}$ and $\frac{\partial \mathbf{R^T(P,T)}}{\partial \mathbf{T}}$ in equation 4.27 may be evaluated with the finite element method as

$$\frac{\partial \mathbf{R^P(P,T)}}{\partial \mathbf{P}} = \int_{\Omega_{2k}} \left[\mathbf{B}_2^T S(\mathbf{P,T}) \, \mathbf{B}_2 + \mathbf{B}_2^T \mathbf{B}_2 \overset{n}{\mathbf{P}} \frac{\partial S(\mathbf{P,T})}{\partial \mathbf{P}} \right] J_2 \, d\Omega_{2k} \qquad (4.28)$$

and

$$\frac{\partial \mathbf{R^T}(\mathbf{P}, \mathbf{T})}{\partial \mathbf{T}} = \int_{\Omega_{3k}} \mathbf{N}^T \rho \, c_p \, \frac{\partial b}{\partial \mathbf{T}} \, \mathbf{B}_3 \overset{\text{n}}{\mathbf{P}} \cdot \mathbf{B}_3 \overset{\text{n}}{\mathbf{T}} \, J_3 \, d\Omega_{3k}$$

$$+ \int_{\Omega_{3k}} \mathbf{N}^T \rho \, c_p \, b \, \mathbf{B}_3 \overset{\text{n}}{\mathbf{P}} \cdot \mathbf{B}_3 \, J_3 \, d\Omega_{3k}$$

$$- \int_{\Omega_{3k}} \left(\frac{\alpha \, d_e}{2\|\mathbf{v}\|^2} \frac{\partial \|\mathbf{v}\|}{\partial \mathbf{T}} \, \mathbf{B}_3^T \mathbf{v} \right) \rho \, c_p \, b \, \mathbf{B}_3 \overset{\text{n}}{\mathbf{P}} \cdot \mathbf{B}_3 \overset{\text{n}}{\mathbf{T}} \, J_3 \, d\Omega_{3k}$$

$$+ \int_{\Omega_{3k}} \left(\frac{\alpha}{2\|\mathbf{v}\|} \frac{\partial d_e}{\partial \mathbf{T}} \, \mathbf{B}_3^T \mathbf{v} \right) \rho \, c_p \, b \, \mathbf{B}_3 \overset{\text{n}}{\mathbf{P}} \cdot \mathbf{B}_3 \overset{\text{n}}{\mathbf{T}} \, J_3 \, d\Omega_{3k}$$

$$+ \int_{\Omega_{3k}} \left(\frac{\alpha \, d_e}{2\|\mathbf{v}\|} \, \mathbf{B}_3^T \frac{\partial \mathbf{v}}{\partial \mathbf{T}} \right) \rho \, c_p \, b \, \mathbf{B}_3 \overset{\text{n}}{\mathbf{P}} \cdot \mathbf{B}_3 \overset{\text{n}}{\mathbf{T}} \, J_3 \, d\Omega_{3k}$$

$$+ \int_{\Omega_{3k}} \left(\frac{\alpha \, d_e}{2\|\mathbf{v}\|} \, \mathbf{B}_3^T \mathbf{v} \right) \rho \, c_p \, \frac{\partial b}{\partial \mathbf{T}} \, \mathbf{B}_3 \overset{\text{n}}{\mathbf{P}} \cdot \mathbf{B}_3 \overset{\text{n}}{\mathbf{T}} \, J_3 \, d\Omega_{3k}$$

$$+ \int_{\Omega_{3k}} \left(\frac{\alpha \, d_e}{2\|\mathbf{v}\|} \, \mathbf{B}_3^T \mathbf{v} \right) \rho \, c_p \, b \, \mathbf{B}_3 \overset{\text{n}}{\mathbf{P}} \cdot \mathbf{B}_3 \, J_3 \, d\Omega_{3k}$$

$$+ \int_{\Omega_{3k}} \mathbf{B}_3^T \, k \, \mathbf{B}_3 \, J_3 \, d\Omega_{3k}$$

$$+ \int_{\Omega_{3k}} \mathbf{N}^T \dot{\gamma}^2 \, \frac{\partial \eta}{\partial \mathbf{T}} \, J_3 \, d\Omega_{3k} \tag{4.29}$$

The above may be solved for the incremental response $\Delta \mathbf{P}$ and $\Delta \mathbf{T}$ by inverting the global tangent stiffness matrix. The responses are then updated according to

$$\mathbf{P^{I+1}} = \mathbf{P^I} + \Delta \mathbf{P} \tag{4.30}$$

$$\mathbf{T^{I+1}} = \mathbf{T^I} + \Delta \mathbf{T} \tag{4.31}$$

The global residual is again evaluated, and if it is not sufficiently small, the process is repeated. It should be noted that when the power-law viscosity equation 4.7 is inserted into equation 2.4, the flow conductance S may not be obtained analytically when the temperature is not uniform in the z-direction. Instead, a numerical solution is required to compute S for the non-isothermal power-law fluid. Compared with Tortorelli [50], solving equation 4.27 is expected to be computationally more efficient

than the equivalent computation in Tortorelli since we replace a single large system in $\mathbf{P}$ and $\mathbf{T}$ with two separate smaller systems, one for $\mathbf{P}$ and another for $\mathbf{T}$. However, the overall computation burden is also influenced by the numbers of iterations which are expected to be less in the full Newton-Raphson method in Tortorelli [50].

The numerical integration formula, known as Gauss-Legendre Quadrature, is used to solve the integral equation 2.4 for S. Since all of the Gauss-Legendre rules in this research use limits of integration ± 1 [82], we transform the integral with $z = \frac{h}{2}(r+1)$. Such that

$$S = \int_{-1}^{1} \frac{[\frac{h}{2}(r+1)]^2}{\eta} \left(\frac{h}{2}\right) dr \tag{4.32}$$

The Gauss numerical integration formula gives

$$S = \sum_{i=1}^{NG} W_i \frac{[\frac{h}{2}(r_i+1)]^2}{\eta(r_i)} \left(\frac{h}{2}\right) \tag{4.33}$$

where NG is the number of Gauss points. W_i and r_i are called Gauss weights and abscissas, respectively. Since the domain of integration in equation 2.4 does not depend on P, we may differentiate its integrand to give

$$\frac{\partial S}{\partial P}[\Delta P] = -\int_0^h \frac{z^2}{\eta^2} \frac{\partial \eta}{\partial P}[\Delta P] dz \tag{4.34}$$

where equations 2.5 and 4.7 are employed to obtain

$$\frac{\partial \eta}{\partial P}[\Delta P] = (1 - \frac{1}{n}) \eta \frac{\boldsymbol{\nabla} P \cdot \boldsymbol{\nabla}[\Delta P]}{\|\boldsymbol{\nabla} P\|^2} \tag{4.35}$$

for a power-law fluid.

The Gauss-Legendre rule is adopted again to solve for the term $\frac{\partial S}{\partial P}$ as

$$\frac{\partial S}{\partial P}[\Delta P] = -\sum_{i=1}^{NG} W_i \frac{[\frac{h}{2}(r_i+1)]^2}{\eta^2} \frac{\partial \eta}{\partial P}[\Delta P] \left(\frac{h}{2}\right) \tag{4.36}$$

96

where we may substitute equation 4.35 into equation 4.36.

The derivative $\frac{\partial b}{\partial \mathbf{T}}$ in equation 4.29 is given as

$$\frac{\partial b}{\partial \mathbf{T}} = \int_z^h \frac{z}{\eta^2} \frac{\partial \eta}{\partial \mathbf{T}} \, dz \tag{4.37}$$

where

$$\frac{\partial \eta}{\partial \mathbf{T}} = -\mathbf{N^T} \frac{E}{R} \frac{1}{n} \eta \frac{1}{\mathbf{T}^2} \tag{4.38}$$

The derivations of derivatives $\frac{\partial d_e}{\partial \mathbf{T}}$ and $\frac{\partial \|\mathbf{V}\|}{\partial \mathbf{T}}$ are given in appendix A.

4.3   Optimization Problem Statement

As we have described before, the pressure drop across the die and exit velocity distribution are related to the success of die design. Pressure drop determines the extruder size and power requirements, and die exit velocity variation influences the sheet thickness uniformity [9]. The goal of minimizing the inlet pressure can be realized by varying the thickness distribution in the die cavity, while placing the constraints on die exit velocity and temperature variation and limiting the slope of die cavity surface.

The die design optimization problem used here is

$$
\boxed{
\begin{aligned}
&\min_{\boldsymbol{\phi} \in \Re^N} && f(\boldsymbol{\phi}) \;=\; P_{in} \\[2mm]
&\text{Such that} && g_1(\boldsymbol{\phi}) = \tfrac{1}{L} \int_{l_{exit}} \left(\tfrac{\bar{v}(\boldsymbol{\phi})}{\bar{v}_a(\boldsymbol{\phi})} - 1 \right)^2 dx \le \epsilon_1 \\[2mm]
& && g_2(\boldsymbol{\phi}) = \left(\tfrac{\bar{v}_a(\boldsymbol{\phi})}{\bar{v}_p} - 1 \right)^2 \le \epsilon_2 \\[2mm]
& && g_3(\boldsymbol{\phi}) = \tfrac{1}{L} \int_{l_{exit}} \left(\tfrac{T(\boldsymbol{\phi})}{T_a(\boldsymbol{\phi})} - 1 \right)^2 dx \le \epsilon_3 \\[2mm]
& && g_4^K(\boldsymbol{\phi}) = \tfrac{\|\boldsymbol{\nabla} h^K(\boldsymbol{\phi})\|}{\|\boldsymbol{\nabla} h_p\|} - 1 \le 0
\end{aligned}
}
\tag{4.39}
$$

The non-linear constrained optimization is to minimize the inlet pressures P_{in}. Design parameters are denoted by $\phi = \{P_{in}, h^I\}$, $I = 1, 2 \ldots N - 1$, where h^I are the $N - 1$ nodal half-height design variables and N is the total number of design variables. The optimization approach considered here can also be used to determine a sheeting die cavity geometry that will accommodate multiple operating conditions (see e.g., [65]), including multiple temperatures and multiple flow materials.

The constraint function g_1, measure the exit velocity variation and are imposed to obtain a uniform exit velocity to within the tolerance ϵ_1. $\bar{v}(\phi)$ is the computed exit velocity, $\bar{v}_a(\phi)$ is the average velocity at the die exit, and l_{exit} denotes the die exit edge. A zero value of g_1 indicates the computed velocity $\bar{v}(\phi)$ equals the average velocity $\bar{v}_a(\phi)$ over the entire width of the die exit.

The average velocity at die exit is written as

$$\bar{v}_a = \frac{1}{L} \int_{l_{exit}} \bar{v}(x) \, dx \tag{4.40}$$

where L is the total length along the die exit.

The constraint function g_2 is imposed to define the flow rate through the die. In our example, the die exit has a uniform height h_{exit} that does not change as a function of design. Therefore, when the average exit velocity $\bar{v}_a$ equals the prescribed exit velocity $\bar{v}_p$, the die is operating at the desired total flow rate Q given as

$$Q = 2h_{exit} \int_{l_{exit}} \bar{v}_p \, dx \tag{4.41}$$

In the optimization problem in equation 4.39, the inlet pressure P_{in} may vary with the design to achieve a desired flow rate [41]. This formulation provides a means to independently enforce exit velocity uniformity with g_1 and total flow rate with g_2, thus allowing more control over the design than that given by Smith [22].

A good extrusion die must distribute the polymer melt in the flow channel such that the material exits from the die with a uniform velocity and temperature [44]. The constraint function g_3, therefore, is employed to obtain a uniform exit temperature. Here, g_3 becomes zero when the temperature T along the centerline of die exit equals the average temperature T_a over the die exit. The average exit temperature T_a is not prescribed a *priori*, but is instead calculated from the temperature field as

$$T_a = \frac{1}{L} \int_{l_{exit}} T(x) \, dx \tag{4.42}$$

In the die cavity, the half-height parameter $h(x, y)$ is arbitrary, so that constraints g_4^K, $K = 1, 2, \ldots N_s$, are imposed to restrict the slope of h to within the prescribed value $\|\nabla h_p\|$. Here, N_s is the number of elements in the finite element model that have a limit on ∇h.

It is important to note that the objective function $f(\phi)$ and constraint g_4^K are explicitly dependent on the design parameters, while the constraints g_1, g_2 and g_3 are explicitly dependent on the design parameters and implicitly dependent on the design parameters through the pressure and temperature field equations. The implicit dependence complicates the design sensitivity analysis. In the following sections, we present an analytical approach to sensitivity analysis and its implementation with the finite element method.

Before illustrating the design sensitivity analysis and optimization, we compute the temperature distribution along the center line of die exit to choose the appropriate value of the SUPG weighting parameter α. We investigate the effect of α on the temperature field using the finite element model shown in figure 4.3. The non-isothermal power-law fluid is used in the analysis and the inlet pressure is 15 MPa.

Figure 4.4 illustrates the temperature distribution along the center line of die exit for α equal to 0.5, 1.0, 3.0, 7.0, 10.0 and 20.0. Note that the SUPG weighting function $\tilde{u}$ reduces to the Galerkin weighting function when $\alpha = 0$. If no upwinding is applied or weighting parameter α is small, as shown in figure 4.4(a), the exit temperature distribution lacks spatially stability. As α increases, the stability in the solution increases. For $\alpha = 7.0$, a spatially smooth temperature distribution is obtained especially in the center area along die exit as illustrated in figure 4.4(d). However, a large value of α may overcompensate convection term (cf. equation 4.15), causing unstable temperature distribution as illustrated in figure 4.4(e,f). Therefore, $\alpha = 7.0$ is used in the following analysis.

4.4   Design Sensitivity Analysis for Fully-Coupled Nonlinear System

Since the objective function $f(\boldsymbol{\phi})$ and constraint $g_4^K(\boldsymbol{\phi})$ in equation 4.39 are explicitly defined on the design $\boldsymbol{\phi}$, the calculation of design sensitivities is straightforward. For the objective function $f(\boldsymbol{\phi})$ in equation 4.39, the design sensitivities may be computed
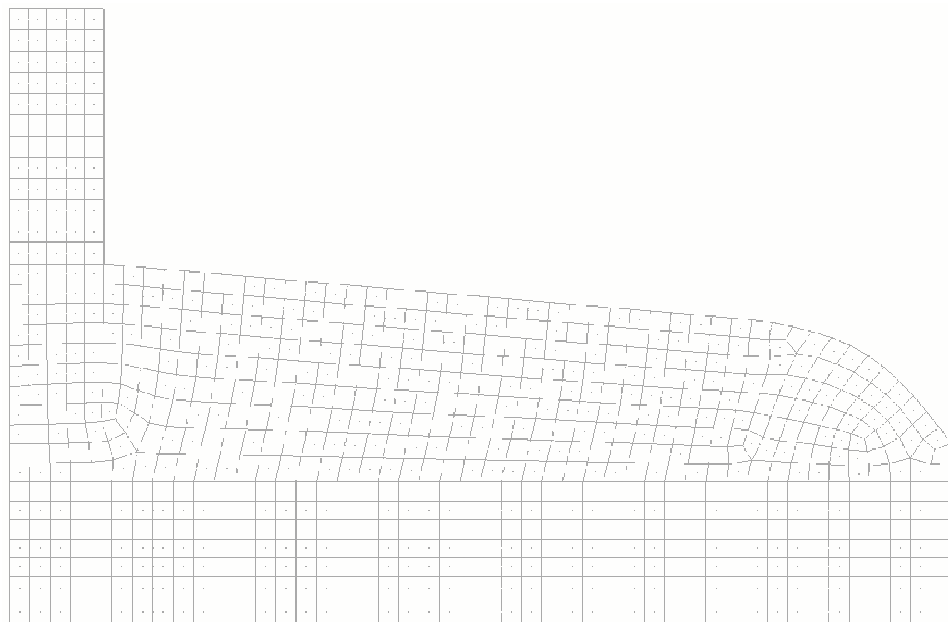
Figure 4.3: Coat hanger sheeting die finite element mesh

a) $\alpha = 0.5$ b) $\alpha = 1.0$

c) $\alpha = 3.0$ d) $\alpha = 7.0$

e) $\alpha = 10.0$ f) $\alpha = 20.0$
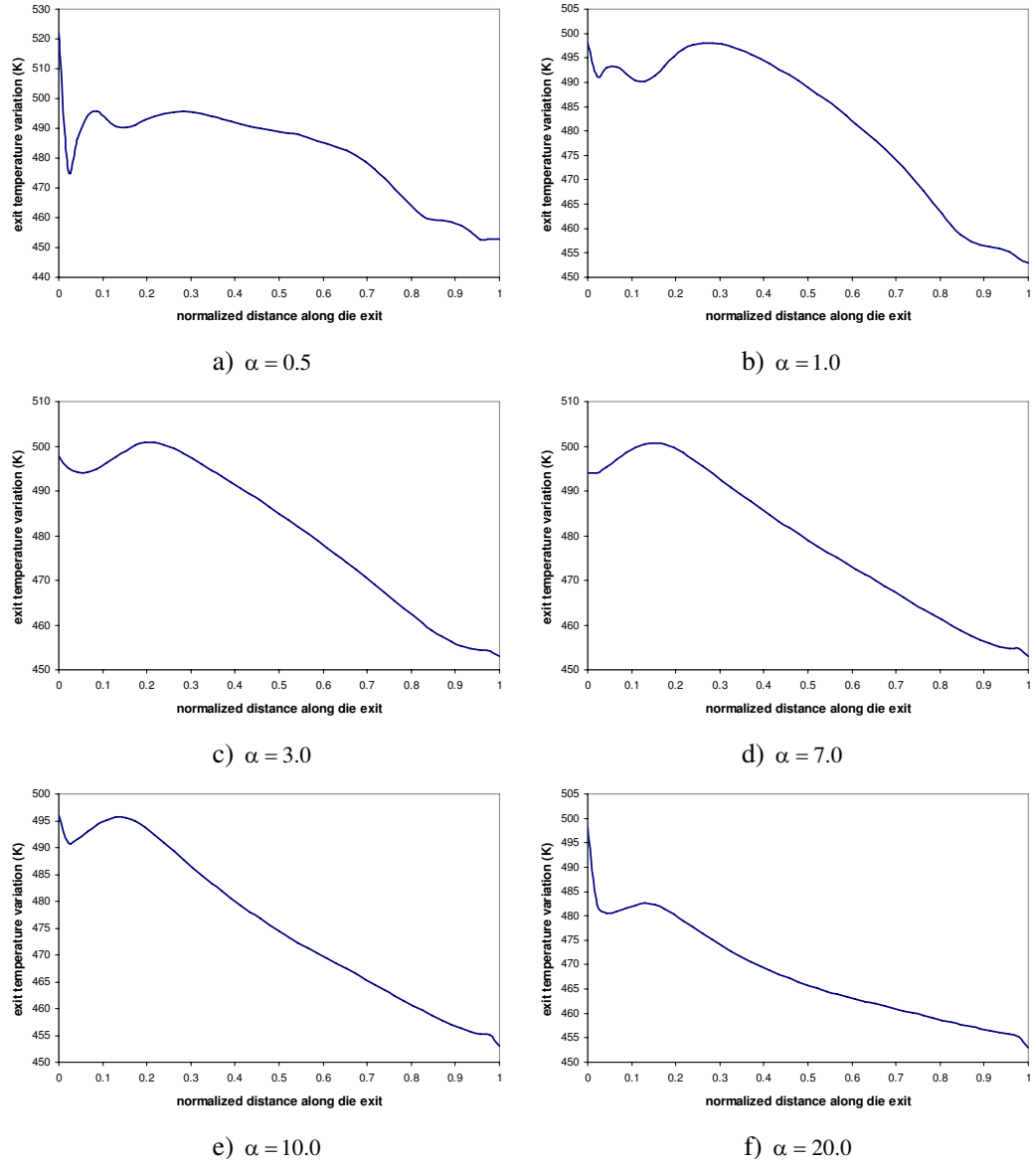
Figure 4.4: Coat hanger sheeting die exit temperature distribution along the center-line as a function of α

from

$$\frac{Df(\boldsymbol{\phi})}{D\phi_i} = \begin{cases} 1 & \text{for} \quad \phi_i = P_{in} \\ 0 & \text{otherwise} \end{cases} \tag{4.43}$$

Following the same procedure, we obtain the sensitivity for the constraint g_4

$$\frac{Dg_4(\boldsymbol{\phi})}{D\phi_i} = \begin{cases} 0 & \text{for} \quad \phi_i = P_{in} \\ \frac{1}{\|\boldsymbol{\nabla} h\|\|\boldsymbol{\nabla} h_p\|}\boldsymbol{\nabla} h \cdot \boldsymbol{\nabla} & \text{otherwise} \end{cases} \tag{4.44}$$

In the analysis to follow, equation 4.44 is evaluated with the finite element method as

$$\frac{Dg_4(\boldsymbol{\phi})}{D\phi_i} = \begin{cases} 0 & \text{for} \quad \phi_i = P_{in} \\ \frac{1}{\|\boldsymbol{\nabla} h_p\|}(\overset{n}{\mathbf{h}}{}^T \mathbf{B}^T \mathbf{B} \overset{n}{\mathbf{h}})^{-\frac{1}{2}} \overset{n}{\mathbf{h}}{}^T \mathbf{B}^T \mathbf{B} & \text{otherwise} \end{cases} \tag{4.45}$$

where we use $\boldsymbol{\nabla} h = \mathbf{B} \overset{n}{\mathbf{h}}$.

The constraint functions $g_1(\boldsymbol{\phi})$, $g_2(\boldsymbol{\phi})$ and $g_3(\boldsymbol{\phi})$ in equation 4.39 are not defined explicitly in terms of design parameters above. Instead, these functions are implicitly defined through the pressure solution computed in equation 2.3 and the temperature solution. To evaluate the implicit sensitivities, we consider a general performance measure

$$F(\boldsymbol{\phi}) = G(\mathbf{P}(\boldsymbol{\phi}), \mathbf{T}(\boldsymbol{\phi}), \boldsymbol{\phi}) \tag{4.46}$$

where F, which may represent the objective function or any one of the constraints, is defined through the function G which is both explicitly dependent on $\boldsymbol{\phi}$ and implicit dependent on $\boldsymbol{\phi}$ through the solution of $\mathbf{P}$ and $\mathbf{T}$. Assuming sufficient smoothness, the design sensitivity of F with respect to the design parameter ϕ_i may be calculated from

$$\frac{DF}{D\phi_i} = \frac{\partial G}{\partial \mathbf{P}} \frac{D\mathbf{P}}{D\phi_i} + \frac{\partial G}{\partial \mathbf{T}} \frac{D\mathbf{T}}{D\phi_i} + \frac{\partial G}{\partial \phi_i} \tag{4.47}$$

103

where the chain-rule is applied to obtain this result. The explicit derivative $\frac{\partial G}{\partial \mathbf{P}}$, $\frac{\partial G}{\partial \mathbf{T}}$ and $\frac{\partial G}{\partial \phi_i}$ are readily available once the objective and constraint functions are defined [41]. The difficulty in evaluating $\frac{DF}{D\phi_i}$ arises from the presences of the implicit response sensitivities $\frac{D\mathbf{P}}{D\phi_i}$ and $\frac{D\mathbf{T}}{D\phi_i}$, which are defined through the Hele-Shaw governing equation 2.3 and energy equation 4.12, respectively. Therefore, the derivatives $\frac{D\mathbf{P}}{D\phi_i}$ and $\frac{D\mathbf{T}}{D\phi_i}$ must be evaluated using the *direct differentiation* method or eliminated from equation 4.47 with the *adjoint variable* method. See [54, 65] for the details about the *direct differentiation* method and the *adjoint variable* method. In this research the number of design variables far exceeds the number of implicit response functions, so that the *adjoint variable* method will be employed (see e.g., [54])

4.4.1   The Adjoint Variable Method

In the adjoint variable method, we eliminate the implicit response derivative $\frac{D\mathbf{P}}{D\phi_i}$ and $\frac{D\mathbf{T}}{D\phi_i}$ from equation 4.47 by defining and solving the appropriate *adjoint* problem. This is accomplished via the Lagrange multiplier method [54]. Equation 4.46 and residual equations 4.25, and 4.26 are combined to form the augmented performance measure $\hat{F}$ as

$$\hat{F}(\boldsymbol{\phi}) = G(\mathbf{P}(\boldsymbol{\phi}), \mathbf{T}(\boldsymbol{\phi}), \boldsymbol{\phi}) - \boldsymbol{\lambda} \cdot \mathbf{R}(\mathbf{P}(\boldsymbol{\phi}), \mathbf{T}(\boldsymbol{\phi}), \boldsymbol{\phi}) \tag{4.48}$$

where $\boldsymbol{\lambda} = \{\boldsymbol{\lambda^P}, \boldsymbol{\lambda^T}\}$ is the *adjoint variable vector* which is an arbitrary vector with a length equal to the number of free degrees of freedom in the finite element problem [54]. $\boldsymbol{\lambda^P}$ is the *adjoint variable vector* for pressure solution, and $\boldsymbol{\lambda^T}$ is the *adjoint variable vector* for temperature solution. The residual term $\mathbf{R}(\mathbf{P}(\boldsymbol{\phi}), \mathbf{T}(\boldsymbol{\phi}), \boldsymbol{\phi})$ is

defined as

$$\mathbf{R}(\mathbf{P}(\boldsymbol{\phi}), \mathbf{T}(\boldsymbol{\phi}), \boldsymbol{\phi}) = \left\{ \begin{array}{c} \mathbf{R^P}\left(\mathbf{P}(\boldsymbol{\phi}), \mathbf{T}(\boldsymbol{\phi}), \boldsymbol{\phi}\right) \\ \mathbf{R^T}\left(\mathbf{P}(\boldsymbol{\phi}), \mathbf{T}(\boldsymbol{\phi}), \boldsymbol{\phi}\right) \end{array} \right\} = 0 \tag{4.49}$$

Here, $\hat{F}(\boldsymbol{\phi}) = F(\boldsymbol{\phi})$ since the augmented term is identically zero. The augmented function is next differentiated with respect to the design variable ϕ_i gives

$$\begin{aligned} \frac{D\hat{F}}{D\phi_i} &= \frac{\partial G}{\partial \mathbf{P}}\frac{D\mathbf{P}}{D\phi_i} + \frac{\partial G}{\partial \mathbf{T}}\frac{D\mathbf{T}}{D\phi_i} + \frac{\partial G}{\partial \phi_i} \\ &\quad - \boldsymbol{\lambda}^\mathbf{P} \cdot \left\{ \frac{\partial \mathbf{R^P}}{\partial \mathbf{P}}\frac{D\mathbf{P}}{D\phi_i} + \frac{\partial \mathbf{R^P}}{\partial \mathbf{T}}\frac{D\mathbf{T}}{D\phi_i} + \frac{\partial \mathbf{R^P}}{\partial \phi_i} \right\} \\ &\quad - \boldsymbol{\lambda}^\mathbf{T} \cdot \left\{ \frac{\partial \mathbf{R^T}}{\partial \mathbf{P}}\frac{D\mathbf{P}}{D\phi_i} + \frac{\partial \mathbf{R^T}}{\partial \mathbf{T}}\frac{D\mathbf{T}}{D\phi_i} + \frac{\partial \mathbf{R^T}}{\partial \phi_i} \right\} \end{aligned} \tag{4.50}$$

Rearranging equation 4.50 yields

$$\begin{aligned} \frac{D\hat{F}}{D\phi_i} &= \frac{\partial G}{\partial \phi_i} - \boldsymbol{\lambda}^\mathbf{P}\frac{\partial \mathbf{R^P}}{\partial \phi_i} - \boldsymbol{\lambda}^\mathbf{T}\frac{\partial \mathbf{R^T}}{\partial \phi_i} \\ &\quad + \frac{D\mathbf{P}}{D\phi_i} \cdot \left\{ \left(\frac{\partial G}{\partial \mathbf{P}}\right)^T - \left[\frac{\partial \mathbf{R^P}}{\partial \mathbf{P}}\right]^T \boldsymbol{\lambda}^\mathbf{P} - \left[\frac{\partial \mathbf{R^T}}{\partial \mathbf{P}}\right]^T \boldsymbol{\lambda}^\mathbf{T} \right\} \\ &\quad + \frac{D\mathbf{T}}{D\phi_i} \cdot \left\{ \left(\frac{\partial G}{\partial \mathbf{T}}\right)^T - \left[\frac{\partial \mathbf{R^P}}{\partial \mathbf{T}}\right]^T \boldsymbol{\lambda}^\mathbf{P} - \left[\frac{\partial \mathbf{R^T}}{\partial \mathbf{T}}\right]^T \boldsymbol{\lambda}^\mathbf{T} \right\} \end{aligned} \tag{4.51}$$

where $()^T$ denotes the matrix transpose. To eliminate $\frac{D\mathbf{P}}{D\phi_i}$ and $\frac{D\mathbf{T}}{D\phi_i}$ from equation 4.51, we equate the coefficients of $\frac{D\mathbf{P}}{D\phi_i}$ and $\frac{D\mathbf{T}}{D\phi_i}$ to zero. The adjoint variable vector $\{\boldsymbol{\lambda}^\mathbf{P}, \boldsymbol{\lambda}^\mathbf{T}\}$, therefore, may be computed by solving the adjoint problem

$$\left\{ \frac{\partial \mathbf{R^T}}{\partial \mathbf{T}} - \frac{\partial \mathbf{R^T}}{\partial \mathbf{P}}\left[\frac{\partial \mathbf{R^P}}{\partial \mathbf{P}}\right]^{-1}\frac{\partial \mathbf{R^P}}{\partial \mathbf{T}} \right\}^T \boldsymbol{\lambda}^\mathbf{T} = \left(\frac{\partial G}{\partial \mathbf{T}}\right)^T - \left[\frac{\partial \mathbf{R^P}}{\partial \mathbf{T}}\right]^T\left[\frac{\partial \mathbf{R^P}}{\partial \mathbf{P}}\right]^{-T}\left(\frac{\partial G}{\partial \mathbf{P}}\right)^T \tag{4.52}$$

$$\boldsymbol{\lambda}^\mathbf{P} = \left[\frac{\partial \mathbf{R^P}}{\partial \mathbf{P}}\right]^{-T}\left\{ \left(\frac{\partial G}{\partial \mathbf{P}}\right)^T - \left[\frac{\partial \mathbf{R^T}}{\partial \mathbf{P}}\right]^T \boldsymbol{\lambda}^\mathbf{T} \right\} \tag{4.53}$$

The derivation here for $\boldsymbol{\lambda}^\mathbf{P}$ and $\boldsymbol{\lambda}^\mathbf{T}$ is similar to that given in Tortorelli [50]. We first assemble $\left\{ \frac{\partial \mathbf{R^T}}{\partial \mathbf{T}} - \frac{\partial \mathbf{R^T}}{\partial \mathbf{P}}\left[\frac{\partial \mathbf{R^P}}{\partial \mathbf{P}}\right]^{-1}\frac{\partial \mathbf{R^P}}{\partial \mathbf{T}} \right\}^T$ and solve for $\boldsymbol{\lambda}^\mathbf{T}$ via the equation 4.52,

and then assemble $\left\{ \left(\frac{\partial G}{\partial \mathbf{P}}\right)^T - \left[\frac{\partial \mathbf{R^T}}{\partial \mathbf{P}}\right]^T \boldsymbol{\lambda^T} \right\}$ and solve for $\boldsymbol{\lambda^P}$ via the equation 4.53. It is noted that, while the solutions for $\mathbf{P}$ and $\mathbf{T}$ as described in figure 4.2 varies from the full Newton-Raphson method in Tortorelli [50], the adjoint sensitivity problem in equations 4.52 and 4.53 are the same.

Once the adjoint variable vector $\{\boldsymbol{\lambda^P}, \boldsymbol{\lambda^T}\}$ is computed, the unknown derivative $\frac{D\mathbf{P}}{D\phi_i}$ and $\frac{D\mathbf{T}}{D\phi_i}$ are eliminated from the sensitivity calculation and we may evaluate $\frac{D\hat{F}}{D\phi_i}$ from the equation 4.51 as

$$\frac{D\hat{F}}{D\phi_i} = \frac{\partial G}{\partial \phi_i} - \boldsymbol{\lambda^P} \frac{\partial \mathbf{R^P}}{\partial \phi_i} - \boldsymbol{\lambda^T} \frac{\partial \mathbf{R^T}}{\partial \phi_i} \tag{4.54}$$

Recall that $\frac{\partial \mathbf{R^P}}{\partial \mathbf{P}}$ and $\frac{\partial \mathbf{R^T}}{\partial \mathbf{T}}$ are the transpose of the inverted tangent stiffness which are evaluated from equations 4.28 and 4.29. The adjoint variable method requires the evaluation of one adjoint problem for each objective and constraint function, thus this method is efficient because it involves only an adjoint load vector assembly and its back substitution into the inverted tangent stiffness for each performance measure [9]. The calculation of $\frac{\partial G}{\partial \mathbf{P}}$, $\frac{\partial G}{\partial \mathbf{T}}$, $\frac{\partial \mathbf{R^P}}{\partial \mathbf{T}}$, $\frac{\partial \mathbf{R^T}}{\partial \mathbf{P}}$, $\frac{\partial \mathbf{R^P}}{\partial \phi_i}$ and $\frac{\partial \mathbf{R^T}}{\partial \phi_i}$ for the die design problem in equations 4.52, 4.53, and 4.54 will be given in the following section.

As an indispensable validation test, finite-difference gradient is calculated and compared against the gradient computed via the adjoint method. The finite-difference check proceeds as follows: The i-th component of the gradient $\frac{D\hat{F}}{D\phi_i}$ is compared with the following finite-difference gradient

$$\frac{d\,F(\phi)}{d\,\phi_i} = \frac{F(\phi + \Delta\phi_i) - F(\phi)}{\Delta\phi_i} \tag{4.55}$$

106

and the comparison is performed for each objective and constraint function. Comparison results are summarized in table 4.1.

Table 4.1: Gradient check via finite-difference method

constraint function	adjoint	finite-difference
constraint g_1	5.6084E-003	1.3107E-003
constraint g_2	3.1535E-001	1.3427E-002
constraint g_3	4.2013E-006	7.7609E-006

4.4.2   Sensitivity Calculations

The derivatives of constraint g_1, g_2 and g_3 in equation 4.39 with respect to the residual vector $\mathbf{P}$ are evaluated, respectively, from

$$\frac{\partial g_1}{\partial \mathbf{P}} = \frac{1}{L} \int_{l_{exit}} 2 \left(\frac{\bar{v}}{\bar{v}_a} - 1 \right) \left[\frac{\partial \bar{v}}{\partial \mathbf{P}} \frac{1}{\bar{v}_a} - \frac{\bar{v}}{\bar{v}_a^2} \frac{\partial \bar{v}_a}{\partial \mathbf{P}} \right] dx \tag{4.56}$$

$$\frac{\partial g_2}{\partial \mathbf{P}} = 2 \left(\frac{\bar{v}_a}{\bar{v}_p} - 1 \right) \left(\frac{1}{\bar{v}_p} \frac{\partial \bar{v}_a}{\partial \mathbf{P}} \right) \tag{4.57}$$

$$\frac{\partial g_3}{\partial \mathbf{P}} = 0 \tag{4.58}$$

where the arguments are omitted for conciseness and it is assumed that pressures and velocities are associated with the appropriate flow conditions.

Equations 4.56 and 4.57 require two derivatives with respect to $\mathbf{P}$, i.e., $\frac{\partial \bar{v}}{\partial \mathbf{P}}$ and $\frac{\partial \bar{v}_a}{\partial \mathbf{P}}$. Differentiating equation $\bar{v} = -\frac{S}{h} \boldsymbol{\nabla} P$ with respect to P, we obtain

$$\frac{\partial \bar{v}}{\partial P}[\Delta P] = \frac{1}{h} \left[\frac{\partial S}{\partial P}[\Delta P] \|\boldsymbol{\nabla} P\| + \frac{S}{\|\boldsymbol{\nabla} P\|} \boldsymbol{\nabla} P \cdot \boldsymbol{\nabla}[\Delta P] \right] \tag{4.59}$$

which is evaluated in the finite element model as

$$\frac{\partial \bar{v}}{\partial \mathbf{P}} = \frac{1}{h} \left[\frac{\partial S}{\partial \mathbf{P}} \|\boldsymbol{\nabla} P\| + \frac{S}{\|\boldsymbol{\nabla} P\|} \overset{n}{\mathbf{P}}{}^T \mathbf{B}^T \mathbf{B} \right] \tag{4.60}$$

The derivative $\frac{\partial \bar{v}_a}{\partial \mathbf{P}}$ is evaluated by differentiating equation 4.40

$$\frac{\partial \bar{v}_a}{\partial \mathbf{P}} = \frac{1}{L} \int_{l_{exit}} \frac{\partial \bar{v}(x)}{\partial \mathbf{P}} \, dx \tag{4.61}$$

By substituting $\frac{\partial \bar{v}}{\partial \mathbf{P}}$ and $\frac{\partial \bar{v}_a}{\partial \mathbf{P}}$ in equations 4.56 and 4.57, the derivatives $\frac{\partial g_1}{\partial \mathbf{P}}$ and $\frac{\partial g_2}{\partial \mathbf{P}}$ are obtained. It should be noted that the integral of equation 4.56 is defined over the entire length along the die exit. Gauss-Legendre quadrature is used to evaluate the integrals along the die exit in equations 4.56 and 4.61.

Similarly, the derivatives of constraint g_1, g_2 and g_3 in equation 4.39 with respect to the residual vector $\mathbf{T}$ are evaluated, respectively, from

$$\frac{\partial g_1}{\partial \mathbf{T}} = \frac{1}{L} \int_{l_{exit}} 2\left(\frac{\bar{v}}{\bar{v}_a} - 1\right) \left[\frac{\partial \bar{v}}{\partial \mathbf{T}} \frac{1}{\bar{v}_a} - \frac{\bar{v}}{\bar{v}_a^2} \frac{\partial \bar{v}_a}{\partial \mathbf{T}}\right] dx \tag{4.62}$$

$$\frac{\partial g_2}{\partial \mathbf{T}} = 2\left(\frac{\bar{v}_a}{\bar{v}_p} - 1\right) \left(\frac{1}{\bar{v}_p} \frac{\partial \bar{v}_a}{\partial \mathbf{T}}\right) \tag{4.63}$$

$$\frac{\partial g_3}{\partial \mathbf{T}} = \frac{1}{L} \int_{l_{exit}} 2\left(\frac{T}{T_a} - 1\right) \left[\frac{\partial T}{\partial \mathbf{T}} \frac{1}{T_a} - \frac{T}{T_a^2} \frac{\partial T_a}{\partial \mathbf{T}}\right] \tag{4.64}$$

Equations 4.62 and 4.63 require two derivatives with respect to $\mathbf{T}$, i.e., $\frac{\partial \bar{v}}{\partial \mathbf{T}}$ and $\frac{\partial \bar{v}_a}{\partial \mathbf{T}}$. Differentiating equation $\bar{v} = -\frac{S}{h}\boldsymbol{\nabla} P$ with respect to $\mathbf{T}$, we obtain

$$\frac{\partial \bar{v}}{\partial \mathbf{T}}[\Delta P] = \frac{1}{h}\frac{\partial S}{\partial \mathbf{T}}[\Delta P] \|\boldsymbol{\nabla} P\| \tag{4.65}$$

where $\frac{\partial S}{\partial \mathbf{T}}$ is written as

$$\frac{\partial S}{\partial \mathbf{T}} = -\int_0^h \frac{z^2}{\eta^2} \frac{\partial \eta}{\partial \mathbf{T}} \, dz \tag{4.66}$$

where $\frac{\partial \eta}{\partial \mathbf{T}}$ is given in equation 4.38.

The derivative $\frac{\partial \bar{v}_a}{\partial \mathbf{T}}$ is evaluated by differentiating equation 4.40

$$\frac{\partial \bar{v}_a}{\partial \mathbf{T}} = \frac{1}{L} \int_{l_{exit}} \frac{\partial \bar{v}(x)}{\partial \mathbf{T}} \, dx \tag{4.67}$$

108

To evaluate $\frac{\partial \mathbf{R^P}}{\partial \mathbf{T}}$ and $\frac{\partial \mathbf{R^T}}{\partial \mathbf{P}}$, the residual R^P and R^T of equations 4.14 and 4.15 are differentiated with respect to T and P, respectively. The linear operator $\frac{\partial R^P}{\partial T}$ is defined such that $\frac{\partial R^P}{\partial T} \approx \mathbf{w}^T \frac{\partial \mathbf{R^P}}{\partial \mathbf{T}}$ where

$$\frac{\partial R^P}{\partial T} = \int_{\Omega_2} \boldsymbol{\nabla} w \cdot \frac{\partial S}{\partial T} \boldsymbol{\nabla} P \, d\Omega_2 \tag{4.68}$$

where we assume q^P is not a function of half-height parameter. Similarly,

$$
\begin{aligned}
\frac{\partial R^T}{\partial P} &= \int_{\Omega_3} w \, \rho \, c_p \frac{\partial b}{\partial P} \boldsymbol{\nabla} P \cdot \boldsymbol{\nabla} T \, d\Omega_3 + \int_{\Omega_3} w \, \rho \, c_p \, b \, \boldsymbol{\nabla} \Delta P \cdot \boldsymbol{\nabla} T \, d\Omega_3 \\
&+ \int_{\Omega_3} \left(\frac{\alpha}{2\|\mathbf{v}\|} \frac{\partial de}{\partial P} \boldsymbol{\nabla} w \cdot \mathbf{v} \right) \rho \, c_p \, b \, \boldsymbol{\nabla} P \cdot \boldsymbol{\nabla} T \, d\Omega_3 \\
&- \int_{\Omega_3} \left(\frac{\alpha \, de}{2\|\mathbf{v}\|^2} \frac{\partial \|\mathbf{v}\|}{\partial P} \boldsymbol{\nabla} w \cdot \mathbf{v} \right) \rho \, c_p \, b \, \boldsymbol{\nabla} P \cdot \boldsymbol{\nabla} T \, d\Omega_3 \\
&+ \int_{\Omega_3} \left(\frac{\alpha \, de}{2\|\mathbf{v}\|} \boldsymbol{\nabla} w \cdot \frac{\partial \mathbf{v}}{\partial P} \right) \rho \, c_p \, b \, \boldsymbol{\nabla} P \cdot \boldsymbol{\nabla} T \, d\Omega_3 \\
&+ \int_{\Omega_3} \left(\frac{\alpha \, de}{2\|\mathbf{v}\|} \boldsymbol{\nabla} w \cdot \mathbf{v} \right) \rho \, c_p \frac{\partial b}{\partial P} \boldsymbol{\nabla} P \cdot \boldsymbol{\nabla} T \, d\Omega_3 \\
&+ \int_{\Omega_3} \left(\frac{\alpha \, de}{2\|\mathbf{v}\|} \boldsymbol{\nabla} w \cdot \mathbf{v} \right) \rho \, c_p \, b \, \boldsymbol{\nabla} \triangle P \cdot \boldsymbol{\nabla} T \, d\Omega_3 \\
&+ \int_{\Omega_3} w \, \dot{\gamma}^2 \frac{\partial \eta}{\partial P} \, d\Omega_3 - 2 \int_{\Omega_3} w \frac{\eta}{\|\boldsymbol{\nabla} P\|} \dot{\gamma}^2 \frac{\partial \|\boldsymbol{\nabla} P\|}{\partial P} \, d\Omega_3 \tag{4.69}
\end{aligned}
$$

Equation 4.68 is evaluated in the finite element model as

$$\frac{\partial \mathbf{R^P}}{\partial \mathbf{T}} = \int_{\Omega_{2k}} \mathbf{B}_2^T \frac{\partial S}{\partial \mathbf{T}} \mathbf{B}_2 \overset{n}{\mathbf{P}} \, J_2 d\Omega_{2k} \tag{4.70}$$

Equation 4.69 is evaluated in the finite element model as

$$
\begin{aligned}
\frac{\partial \mathbf{R^T}}{\partial \mathbf{P}} &= \int_{\Omega_{3k}} \mathbf{N}^T \rho \, c_p \frac{\partial b}{\partial \mathbf{P}} \mathbf{B}_3 \overset{n}{\mathbf{P}} \cdot \mathbf{B}_3 \overset{n}{\mathbf{T}} \, J_3 d\Omega_{3k} \\
&+ \int_{\Omega_{3k}} \mathbf{N}^T \rho \, c_p \, b \, \mathbf{B}_3 \cdot \mathbf{B}_3 \overset{n}{\mathbf{T}} \, J_3 d\Omega_{3k}
\end{aligned}
$$

$$
+ \int_{\Omega_{3k}} \left(\frac{\alpha}{2\|\mathbf{v}\|} \frac{\partial de}{\partial \mathbf{P}} \mathbf{B}_3^T \mathbf{v} \right) \rho\, c_p\, b\, \mathbf{B}_3 \overset{n}{\mathbf{P}} \cdot \mathbf{B}_3 \overset{n}{\mathbf{T}}\, J_3 d\Omega_{3k}
$$

$$
- \int_{\Omega_{3k}} \left(\frac{\alpha\, de}{2\|\mathbf{v}\|^2} \frac{\partial \|\mathbf{v}\|}{\partial \mathbf{P}} \mathbf{B}_3^T \mathbf{v} \right) \rho\, c_p\, b\, \mathbf{B}_3 \overset{n}{\mathbf{P}} \cdot \mathbf{B}_3 \overset{n}{\mathbf{T}}\, J_3 d\Omega_{3k}
$$

$$
+ \int_{\Omega_{3k}} \left(\frac{\alpha\, de}{2\|\mathbf{v}\|} \mathbf{B}_3^T \frac{\partial \mathbf{v}}{\partial \mathbf{P}} \right) \rho\, c_p\, b\, \mathbf{B}_3 \overset{n}{\mathbf{P}} \cdot \mathbf{B}_3 \overset{n}{\mathbf{T}}\, J_3 d\Omega_{3k}
$$

$$
+ \int_{\Omega_{3k}} \left(\frac{\alpha\, de}{2\|\mathbf{v}\|} \mathbf{B}_3^T \mathbf{v} \right) \rho\, c_p\, \frac{\partial b}{\partial \mathbf{P}} \mathbf{B}_3 \overset{n}{\mathbf{P}} \cdot \mathbf{B}_3 \overset{n}{\mathbf{T}}\, J_3 d\Omega_{3k}
$$

$$
+ \int_{\Omega_{3k}} \left(\frac{\alpha\, de}{2\|\mathbf{v}\|} \mathbf{B}_3^T \mathbf{v} \right) \rho\, c_p\, b\, \mathbf{B}_3 \cdot \mathbf{B}_3 \overset{n}{\mathbf{T}}\, J_3 d\Omega_{3k}
$$

$$
+ \int_{\Omega_{3k}} \mathbf{N}^T \dot{\gamma}^2 \frac{\partial \eta}{\partial \mathbf{P}}\, J_3 d\Omega_{3k}
$$

$$
-2 \int_{\Omega_{3k}} \mathbf{N}^T \frac{\eta}{\|\boldsymbol{\nabla} P\|} \dot{\gamma}^2 \frac{\partial \|\boldsymbol{\nabla} P\|}{\partial \mathbf{P}}\, J_3 d\Omega_{3k} \tag{4.71}
$$

Next, we calculate the terms $\frac{\partial \mathbf{R^P}}{\partial \phi_i}$ and $\frac{\partial \mathbf{R^T}}{\partial \phi_i}$. In the case of $\phi_i = P_{in}$, $\frac{\partial \mathbf{R^P}}{\partial \phi_i}$ and $\frac{\partial \mathbf{R^T}}{\partial \phi_i}$ are computed through the tangent stiffness $\frac{\partial \mathbf{R^P}}{\partial \mathbf{P}}$ and $\frac{\partial \mathbf{R^T}}{\partial \mathbf{P}}$, respectively. The evaluation forms are as follows

$$
\frac{\partial \mathbf{R^P}}{\partial P_{in}} = \frac{\partial \mathbf{R^P}}{\partial \mathbf{P}} \frac{\partial \mathbf{P}}{\partial P_{in}}
$$

$$
\frac{\partial \mathbf{R^T}}{\partial P_{in}} = \frac{\partial \mathbf{R^T}}{\partial \mathbf{P}} \frac{\partial \mathbf{P}}{\partial P_{in}} \tag{4.72}
$$

where $\frac{\partial \mathbf{P}}{\partial P_{in}}$ is a zero vector with unity in the components associated with P_{in}. Therefore, only those nodes associated with inlet pressure P_{in} need to be considered when computing equation 4.72.

In case of $\phi_i = h^I, I = 1, 2 \ldots N - 1$, where h^I are the $N - 1$ nodal half-height design variables and N is the total number of design variables, the derivative $\frac{\partial \mathbf{R^P}}{\partial \phi_i}$ is computed by differentiating equation 4.14 with respect to ϕ_i as

$$
\frac{\partial \mathbf{R^P}}{\partial \phi_i} = \int_{\Omega_2} \boldsymbol{\nabla} w \cdot \frac{\partial S}{\partial \phi_i} \nabla P\, d\Omega_2 \tag{4.73}
$$

where we assume q^P is not a function of half-height parameter. Equation 4.73 is evaluated in the finite element model as

$$\frac{\partial \mathbf{R^P}}{\partial \phi_i} = \int_{\Omega_{2k}} \mathbf{B}_2^T \frac{\partial S}{\partial \phi_i} \mathbf{B}_2 \overset{n}{\mathbf{P}} J_2 d\Omega_{2k} \tag{4.74}$$

Similarly, the derivative $\frac{\partial \mathbf{R^T}}{\partial \phi_i}$ is computed by differentiating equation 4.15 with respect to ϕ_i, and evaluated in the finite element model as

$$
\begin{aligned}
\frac{\partial \mathbf{R^T}}{\partial \phi_i} &= \int_{\Omega_{3k}} \mathbf{N}^T \rho\, c_p \frac{\partial b}{\partial \phi_i} \mathbf{B}_3 \overset{n}{\mathbf{P}} \cdot \mathbf{B}_3 \overset{n}{\mathbf{T}} J_3 d\Omega_{3k} \\
&+ \int_{\Omega_{3k}} \mathbf{N}^T \rho\, c_p\, b \frac{\partial \mathbf{B}_3}{\partial \phi_i} \overset{n}{\mathbf{P}} \cdot \mathbf{B}_3 \overset{n}{\mathbf{T}} J_3 d\Omega_{3k} \\
&+ \int_{\Omega_{3k}} \mathbf{N}^T \rho\, c_p\, b\, \mathbf{B}_3 \overset{n}{\mathbf{P}} \cdot \frac{\partial \mathbf{B}_3}{\partial \phi_i} \overset{n}{\mathbf{T}} J_3 d\Omega_{3k} \\
&+ \int_{\Omega_{3k}} \mathbf{N}^T \rho\, c_p\, b\, \mathbf{B}_3 \overset{n}{\mathbf{P}} \cdot \mathbf{B}_3 \overset{n}{\mathbf{T}} \frac{\partial J_3}{\partial \phi_i} d\Omega_{3k} \\
&+ \int_{\Omega_{3k}} \left(\frac{\alpha}{2\|\mathbf{v}\|} \frac{\partial de}{\partial \phi_i} \mathbf{B}_3^T \mathbf{v} \right) \rho\, c_p\, b\, \mathbf{B}_3 \overset{n}{\mathbf{P}} \cdot \mathbf{B}_3 \overset{n}{\mathbf{T}} J_3 d\Omega_{3k} \\
&- \int_{\Omega_{3k}} \left(\frac{\alpha\, de}{2\|\mathbf{v}\|^2} \frac{\partial \|\mathbf{v}\|}{\partial \phi_i} \mathbf{B}_3^T \mathbf{v} \right) \rho\, c_p\, b\, \mathbf{B}_3 \overset{n}{\mathbf{P}} \cdot \mathbf{B}_3 \overset{n}{\mathbf{T}} J_3 d\Omega_{3k} \\
&+ \int_{\Omega_{3k}} \left(\frac{\alpha\, de}{2\|\mathbf{v}\|} \frac{\partial \mathbf{B}_3^T}{\partial \phi_i} \mathbf{v} \right) \rho\, c_p\, b\, \mathbf{B}_3 \overset{n}{\mathbf{P}} \cdot \mathbf{B}_3 \overset{n}{\mathbf{T}} J_3 d\Omega_{3k} \\
&+ \int_{\Omega_{3k}} \left(\frac{\alpha\, de}{2\|\mathbf{v}\|} \mathbf{B}_3^T \frac{\partial \mathbf{v}}{\partial \phi_i} \right) \rho\, c_p\, b\, \mathbf{B}_3 \overset{n}{\mathbf{P}} \cdot \mathbf{B}_3 \overset{n}{\mathbf{T}} J_3 d\Omega_{3k} \\
&+ \int_{\Omega_{3k}} \left(\frac{\alpha\, de}{2\|\mathbf{v}\|} \mathbf{B}_3^T \mathbf{v} \right) \rho\, c_p \frac{\partial b}{\partial \phi_i} \mathbf{B}_3 \overset{n}{\mathbf{P}} \cdot \mathbf{B}_3 \overset{n}{\mathbf{T}} J_3 d\Omega_{3k} \\
&+ \int_{\Omega_{3k}} \left(\frac{\alpha\, de}{2\|\mathbf{v}\|} \mathbf{B}_3^T \mathbf{v} \right) \rho\, c_p\, b \frac{\partial \mathbf{B}_3}{\partial \phi_i} \overset{n}{\mathbf{P}} \cdot \mathbf{B}_3 \overset{n}{\mathbf{T}} J_3 d\Omega_{3k} \\
&+ \int_{\Omega_{3k}} \left(\frac{\alpha\, de}{2\|\mathbf{v}\|} \mathbf{B}_3^T \mathbf{v} \right) \rho\, c_p\, b\, \mathbf{B}_3 \overset{n}{\mathbf{P}} \cdot \frac{\partial \mathbf{B}_3}{\partial \phi_i} \overset{n}{\mathbf{T}} J_3 d\Omega_{3k} \\
&+ \int_{\Omega_{3k}} \left(\frac{\alpha\, de}{2\|\mathbf{v}\|} \mathbf{B}_3^T \mathbf{v} \right) \rho\, c_p\, b\, \mathbf{B}_3 \overset{n}{\mathbf{P}} \cdot \mathbf{B}_3 \overset{n}{\mathbf{T}} \frac{\partial J_3}{\partial \phi_i} d\Omega_{3k} \\
&+ \int_{\Omega_{3k}} \frac{\partial \mathbf{B}_3^T}{\partial \phi_i} k\, \mathbf{B}_3 \overset{n}{\mathbf{T}} J_3 d\Omega_{3k} + \int_{\Omega_{3k}} \mathbf{B}_3^T k \frac{\partial \mathbf{B}_3}{\partial \phi_i} \overset{n}{\mathbf{T}} J_3 d\Omega_{3k} \\
&+ \int_{\Omega_{3k}} \mathbf{B}_3^T k\, \mathbf{B}_3 \overset{n}{\mathbf{T}} \frac{\partial J_3}{\partial \phi_i} d\Omega_{3k} - \int_{\Omega_{3k}} \mathbf{N}^T \eta\, \dot{\gamma}^2 \frac{\partial J_3}{\partial \phi_i} d\Omega_{3k}
\end{aligned}
$$

111

$$+ \int_{\Omega_{3k}} \mathbf{N}^T \dot{\gamma}^2 \frac{\partial \eta}{\partial \phi_i} J_3 d\Omega_{3k} - 2 \int_{\Omega_{3k}} \mathbf{N}^T \dot{\gamma}^2 \frac{\eta}{h} \frac{\partial h}{\partial \phi_i} J_3 d\Omega_{3k} \qquad (4.75)$$

where

$$\frac{\partial \mathbf{B}_3}{\partial \phi_i} = \frac{\partial \mathbf{J}_3^{-T}}{\partial \phi_i} \frac{\partial \mathbf{N}}{\partial \boldsymbol{\xi}} \qquad (4.76)$$

The expressions for $\frac{\partial \mathbf{J}_3^{-T}}{\partial \phi_i} = -\mathbf{J}_3^{-T} \frac{\partial \mathbf{J}_3^T}{\partial \phi_i} \mathbf{J}_3^{-T}$, $\frac{\partial J_3}{\partial \phi_i} = J_3 \, tr \left(\frac{\partial \mathbf{J}_3}{\partial \phi_i} \mathbf{J}_3^{-1} \right)$ and $\frac{\partial \mathbf{J}_3}{\partial \phi_i} = \frac{\partial \mathbf{N}}{\partial \boldsymbol{\xi}} \frac{\partial \mathbf{X}}{\partial \phi_i}^{\mathrm{n}}$

from Tortorelli and Wang [50] are used to evaluate the above equation.

Note that, for the adjoint variable method, the adjoint analysis must be performed

for each implicit response functional, i.e., each objective function and constraint func-

tion. In the above, we must evaluate $\frac{\partial S}{\partial \phi_i}$ which depend on the fluid material model.

Non-isothermal fluid flow complicates the evaluation of flow conductance S since it

has no explicit formula when the temperature varies through the thickness of the die.

The derivative $\frac{\partial S}{\partial \phi_i}$ cannot be obtained analytically. Therefore, the flow conductance

sensitivity for non-isothermal power-law fluid must be calculated numerically.

Differentiating equation 4.32 with the limits of integration from -1 to 1, the

expression $\frac{\partial S}{\partial \phi_i}$ and its numerical solution can be written as

$$\frac{\partial S}{\partial \phi_i} = \int_{-1}^{1} \left[\frac{3z^2}{2\eta} \frac{\partial h}{\partial \phi_i} - \frac{hz^2}{2\eta^2} \frac{\partial \eta}{\partial \phi_i} \right] dr \qquad (4.77)$$

where we map the domain of integration such that $z = \frac{h}{2}(r + 1)$ to facilitate differ-

entiation. Equation 4.77 is evaluated numerically using Gauss-Legendre integration

as

$$\frac{\partial S}{\partial \phi_i} = \sum_{i=1}^{NG} W_i \left[\frac{3z^2}{2\eta} \frac{\partial h}{\partial \phi_i} - \frac{hz^2}{2\eta^2} \frac{\partial \eta}{\partial \phi_i} \right] \qquad (4.78)$$

where W_i and r_i are Gauss weights and abscissas, respectively. We use 8-point Gauss quadrature, i.e. $NG = 8$ for Gauss-Legendre integration.

As can be seen in equation 4.77, in order to determine $\frac{\partial S}{\partial \phi_i}$, the term $\frac{\partial \eta}{\partial \phi_i}$ is needed. Differentiating the viscosity η from equation 4.7 with respect to the half-height design variable ϕ_i and rearranging gives

$$\frac{\partial \eta}{\partial \phi_i} = \frac{n-1}{n} \frac{\eta}{h} \frac{\partial h}{\partial \phi_i} \tag{4.79}$$

where the height sensitivity $\frac{\partial h}{\partial \phi_i}$ with respect to a nodal height design variable at an arbitrary node k, i.e., $\phi_i = h^k$, is

$$\frac{\partial h}{\partial \phi_i} = \mathbf{N}(\boldsymbol{\xi}) \frac{\partial \overset{n}{\mathbf{h}}}{\partial h^k} \tag{4.80}$$

where we only consider those elements connected to the node k. Thus, the height sensitivity becomes

$$\frac{\partial h}{\partial \phi_i} = \mathbf{N}(\boldsymbol{\xi}) \frac{\partial \overset{n}{\mathbf{h}}}{\partial h^k} = N^k(\boldsymbol{\xi}) \tag{4.81}$$

Once the terms $\frac{\partial G}{\partial \mathbf{P}}$, $\frac{\partial G}{\partial \mathbf{T}}$, $\frac{\partial \mathbf{R^P}}{\partial \mathbf{T}}$, $\frac{\partial \mathbf{R^T}}{\partial \mathbf{P}}$, $\frac{\partial \mathbf{R^P}}{\partial \phi_i}$ and $\frac{\partial \mathbf{R^T}}{\partial \phi_i}$ are evaluated, the adjoint variable vector $\{\boldsymbol{\lambda^P}, \boldsymbol{\lambda^T}\}$ is computed with equations 4.52 and 4.53, and the design sensitivity $\frac{D\hat{F}}{D\phi_i}$ follows from the equation 4.54.

4.5 Die Design Example

The design sensitivity analysis discussed above is combined with optimization algorithm [60] to design coat-hanger sheeting dies and sheeting dies with a general cavity thickness distribution and in-plane shape. Of particular interest here is the die design

for producing polymer sheets with large width-to-height ratios. In this die design, the pressure drop across the die and the exit velocity and temperature distribution are of fundamental importance. Die designs are obtained with a minimum pressure drop and uniform exit velocity and temperature.

The coat-hanger design has a flow channel along its back edge that distributes the polymer melt across the width of the die. The polymer melt leaves the flow channel through a thin slit and passes through a region of uniform height to the die exit. The die cavity geometry considered here follows that given in chapter 2 (see e.g., figure 2.3). Part of manifold is considered as the design region, while the die inlet, preland, secondary manifold and land each have uniform cavity half-height, and act as a resistance to provide better fluid flow uniformity. The dimensions that define our die cavity geometry are given in a paper of Gifford [46], except for the land half-height, which is fixed at 1.2 mm in this study.

The finite element mesh of coat-hanger die cavity geometry appears in figure 4.5. The die cavity geometry is modeled with 4-node isoparametric quadrilateral elements. Due to the symmetry and computational efficiency, we only consider the half geometry in the calculation with 873 nodes and 799 elements. The design variable ϕ from equation 4.39 defines the die cavity half-height in the manifold region through 425 nodal half-height design variables (bounded by $1.20\,\mathrm{mm} \leq h^I \leq 19.05\,\mathrm{mm}$ in the optimization), and die inlet pressure P_{in} (bounded by $1.0\,\mathrm{MPa} \leq P_{in} \leq 20\,\mathrm{MPa}$ in the optimization). Therefore, a total of $N = 426$ design variables in the optimization problem are given in equation 4.39.
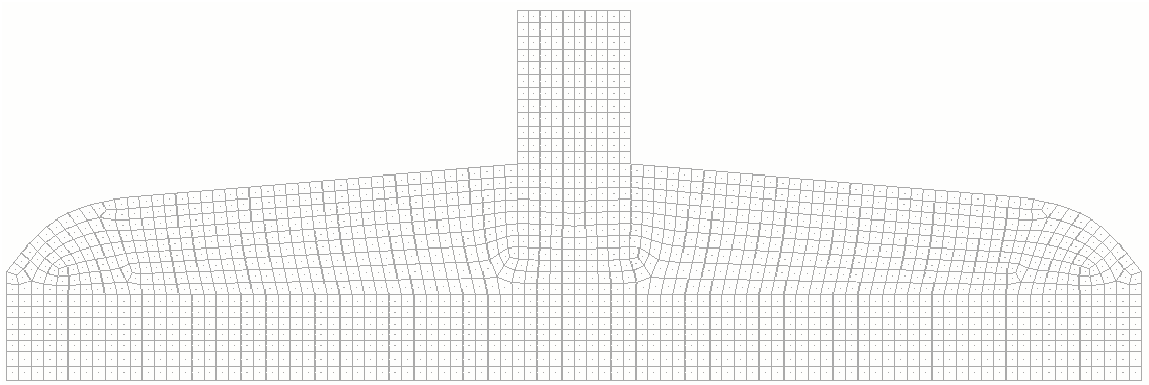
Figure 4.5: Finite element mesh of coat hanger die cavity geometry

The objective and constraint functions are given in equation 4.39 for design optimization considered below. Exit velocity tolerances for constraints g_1 and g_2 are defined as $\epsilon_1 = 0.01$ and $\epsilon_2 = 0.001$, respectively. Exit temperature tolerance for constraint g_3 is defined as $\epsilon_3 = 0.0005$. In addition, $N_s = 425$ height-gradient constraints are defined as $\|\nabla h_p\| = 0.25$. The sequential linear programming (SLP) algorithm in Design Optimization Tools (DOT) [60] is used to solve the optimization problems.

This example considers the optimal design of the die cavity geometry described above using the non-isothermal power-law fluid model. The flow of linear low density polyethylene (LLDPE) at $463\,\text{K}$ is selected where material constants $m = 15320\,\text{Pa-s}$, $n = 0.51$, $E/R = 2813\,\text{K}$, and the reference temperature $T_0 = 463\,\text{K}$ are taken from Arpin [44].

Optimization results are summarized in table 4.2, where the optimal die cavity design is obtained in 60 SLP design iterations. The pressure drop decreases from 15.0 MPa to 9.92 MPa. The optimization history for the inlet pressure appears in figure 4.6 and values of the constraints g_1, g_2 and g_3 in equation 4.39 are shown in figure 4.7 at each optimization iteration. In these calculations, the exit velocity variation constraint g_1 is reduced considerably from its initial value of 43.0×10^{-3} to its optimal value of 6.81×10^{-3}, the exit flow rate constraint g_2 is reduced from 1130×10^{-3} to 0.974×10^{-3}, which is well below the tolerance ϵ_2. Similarly, the exit temperature constraint g_3 is decreased from 1.03×10^{-3} to 0.441×10^{-3} in the same calculation. Figure 4.8 illustrates the gap-wise average exit velocity for the initial and optimal die designs where the distance along the die exit is normalized by dividing

by the exit width of 508 mm. Note that the velocity for the optimal design is uniform over most of the die exit at a value that is close to the target velocity of 100 mm/s, with the exception of a slight reduction at the outer edge. The average exit velocity v_a, and the maximum and minimum gap-wise average exit velocities are given in table 4.2 to further emphasize the success of the optimization procedure. The exit temperature variation for initial and optimal design is shown in figure 4.9. Compared with the initial design, the optimal design generates a relatively uniform temperature distribution at the die exit.

The pressure distribution of the initial and optimal designs are shown in figure 4.10(a,b), respectively. The isobars just inside the die exit of the optimal design are more parallel than those of the initial design, as shown in figure 4.10(a,b). This indicates that the exit velocity distribution of the optimal design should be more uniform than that of the initial design which is, in fact, the case as illustrated in figure 4.8. The goal in design of an extrusion die is to obtain a uniform thickness and temperature across the width at the exit. Figure 4.11 compares the temperature distributions in the midplane of the die for the initial and optimal designs. The temperature distributions at the die exit in figures 4.11(a) and (b) are significantly different. The temperature near the center of die exit in initial design is about 48 degrees higher than that at the die outer edge. The difference in temperature can affect the final thickness of the extruded sheet. It is noted that difference in temperature distributions of the optimal design is much more improved. The temperature at the die exit center is about 35 degrees higher than that at the die outer edge, as shown in figure

117

4.11(b). Additionally, when the highly viscous melt flows through the die inlet and merges into the manifold region, the shear rate near the die wall of proximal end of manifold are higher than those in the other regions of manifold [83]. As a result of combined effect of high shear rate and viscous dissipation, the relatively higher temperature occurs around the neck of the die.

The die cavity half-heights are presented in figure 4.12(a) for the initial design and in figure 4.12(b) for the optimal design. The gap thickness in the manifold region of the optimal design is decreased in comparison with that of the initial design, and has a slight reduction in the area around the neck of the die inlet.

Table 4.2: Optimization results summary

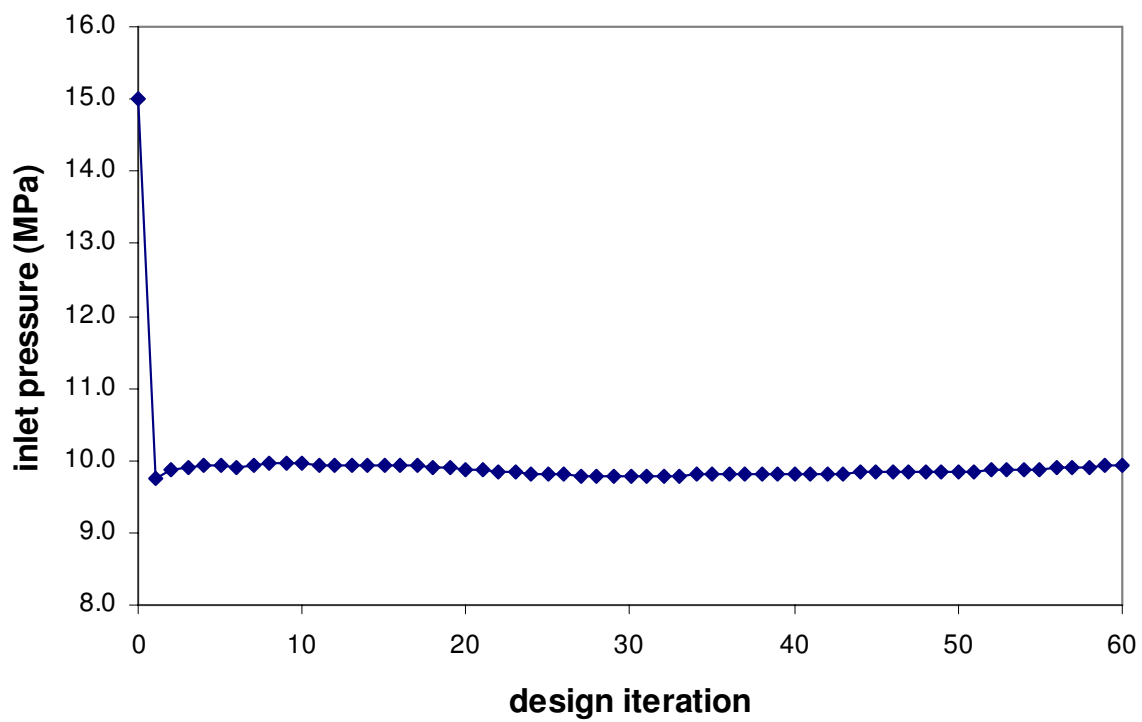| die design	initial	optimal
P_{in} (MPa)	15.0	9.92
constraint g_1 ($\times 10^{-3}$)	43.0	6.81
constraint g_2 ($\times 10^{-3}$)	1130	0.974
constraint g_3 ($\times 10^{-3}$)	1.03	0.441
v_a (mm/s)	206.4	96.8
v_{exit} (mm/s) (max)	266.2	114.2
(min)	136.4	77.1
T_a (K)	478.7	480.1
T_{exit} (K) (max)	500.6	498.0
(min)	453.0	453.0

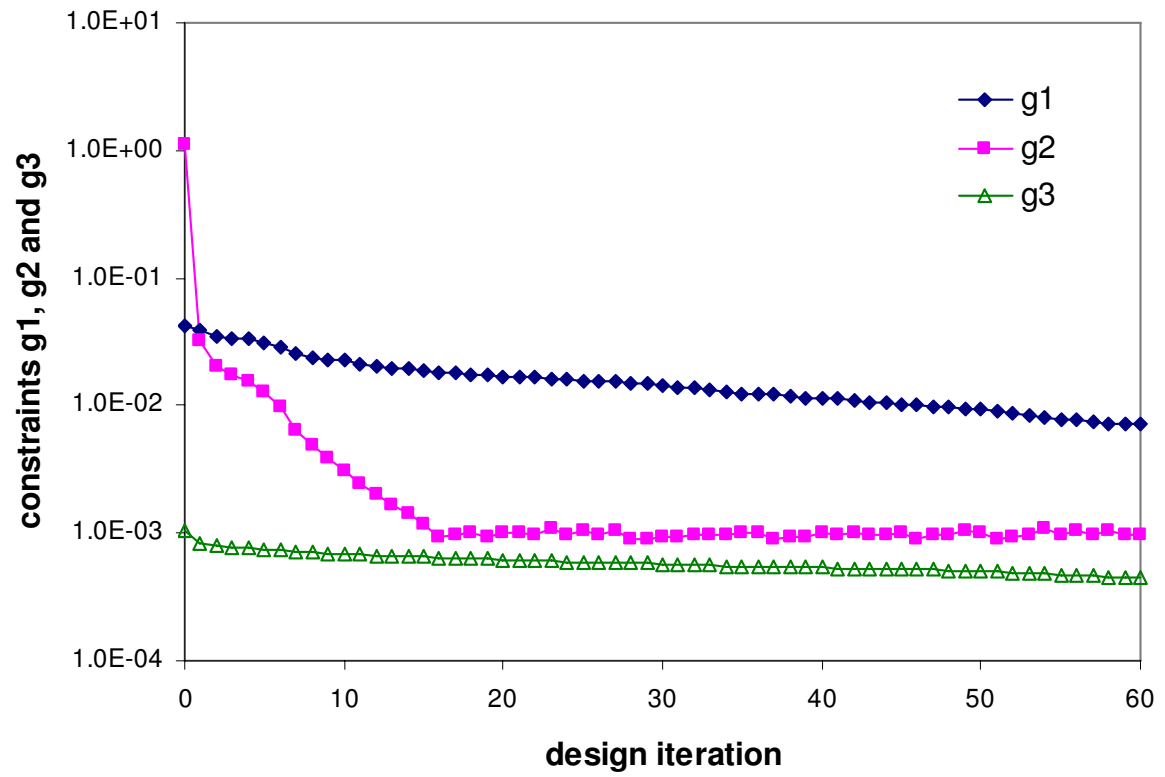Figure 4.6: Objective function optimization history

Figure 4.7: Optimization history for exit velocity and temperature constraints

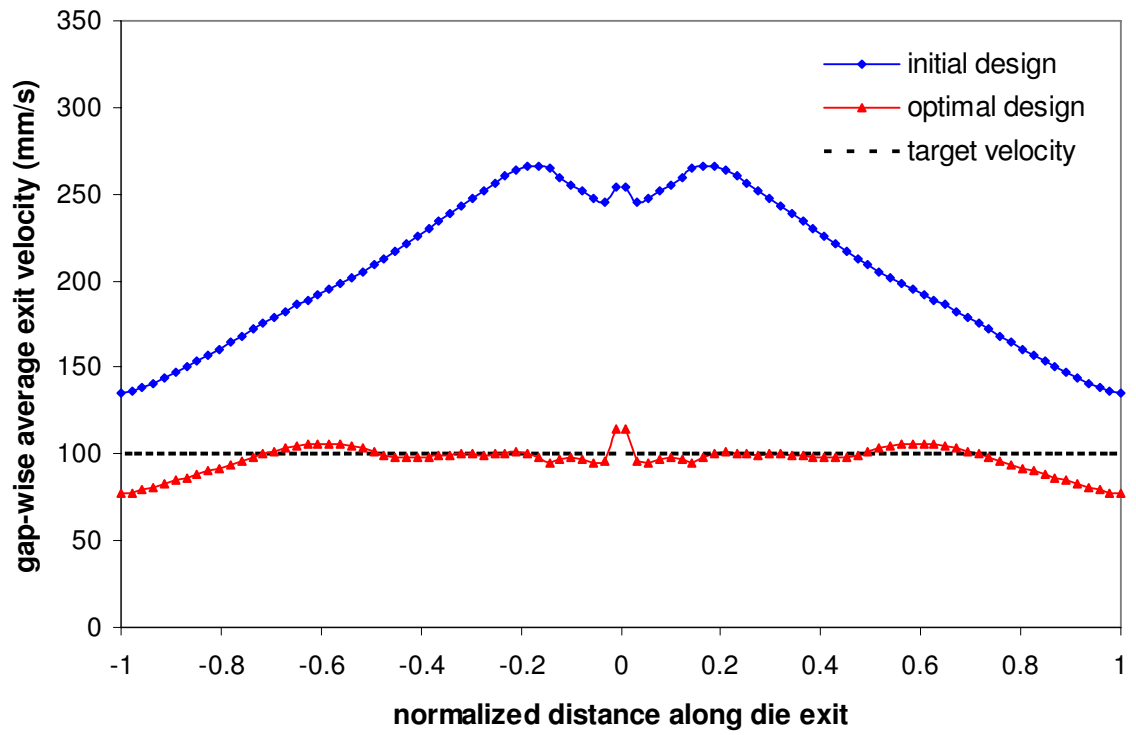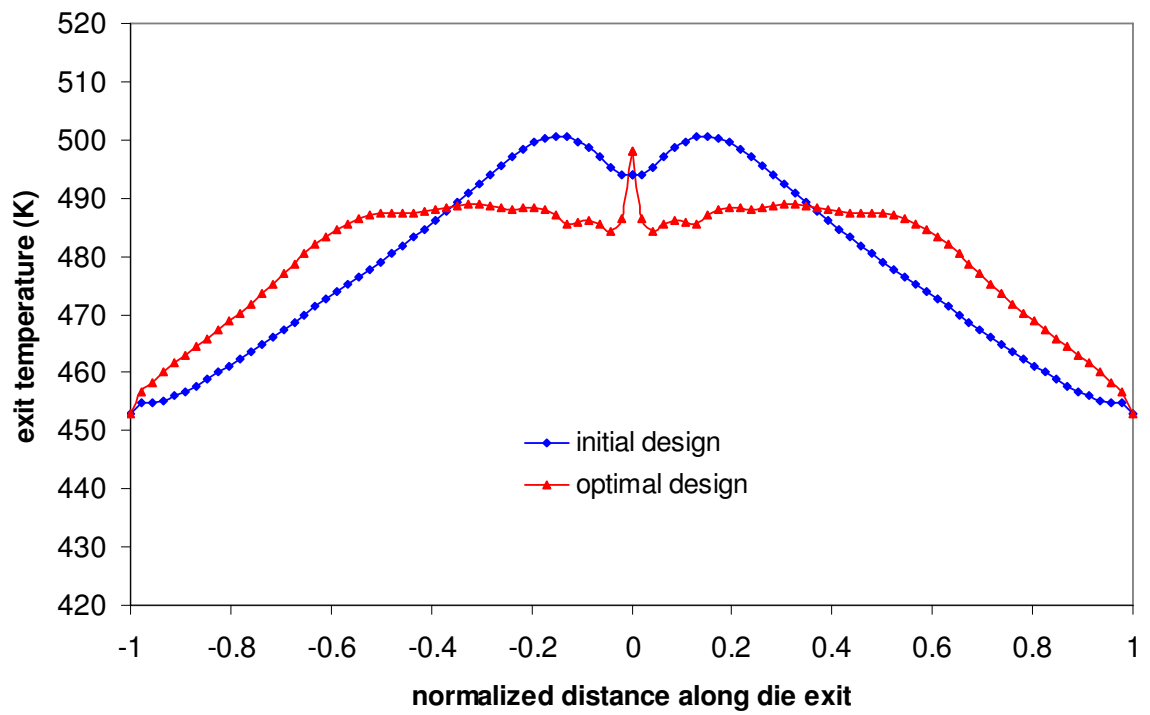Figure 4.8: Exit velocities for coat hanger die design

Figure 4.9: Exit temperatures along the center line of die exit for coat hanger die design
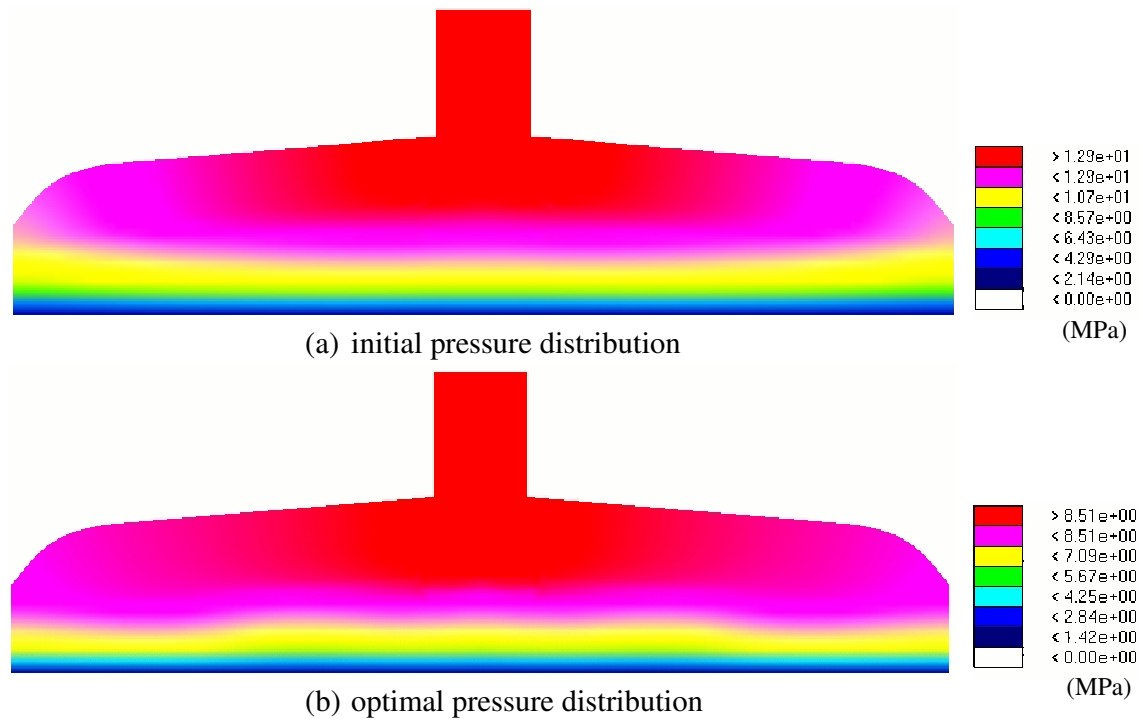
(a) initial pressure distribution

(b) optimal pressure distribution

Figure 4.10: Pressure distribution in the die cavity

(a) initial temperature distribution (K)

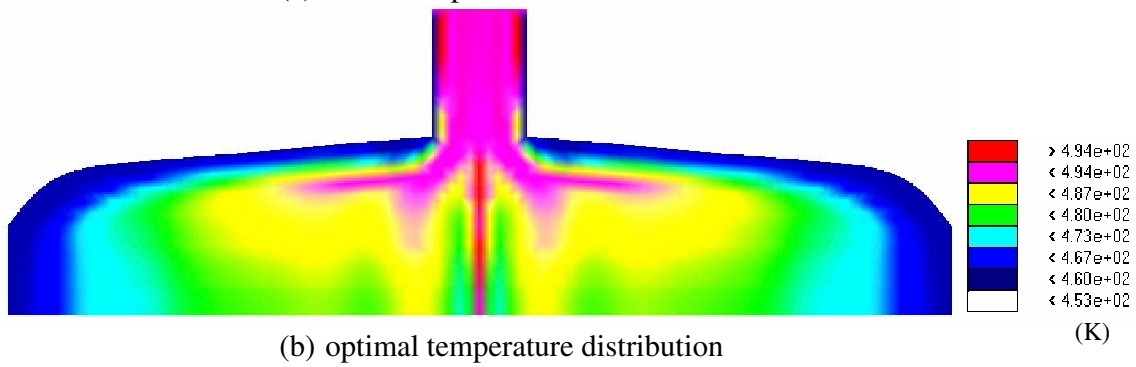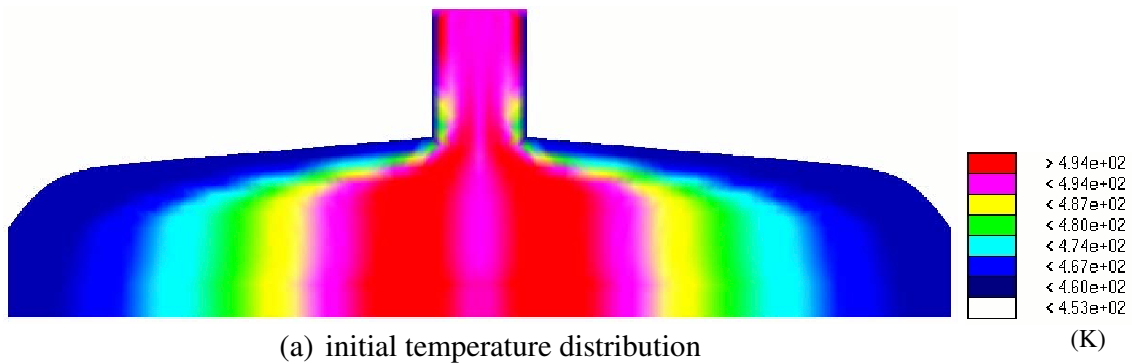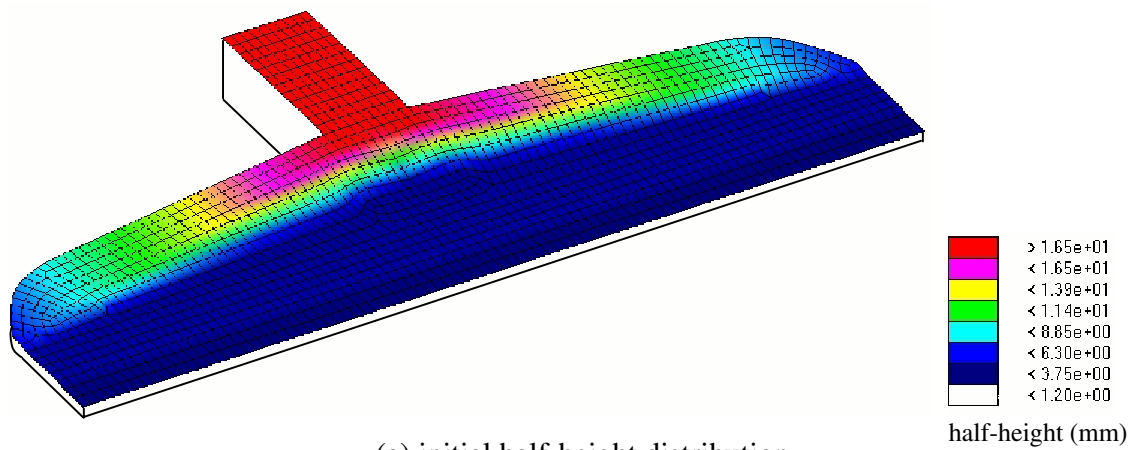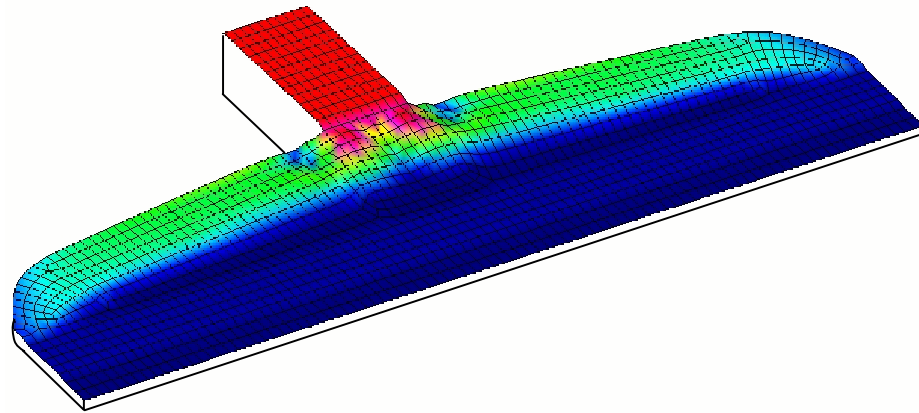(b) optimal temperature distribution (K)

Figure 4.11: Temperature distribution in the die cavity mid-plane

(a) initial half-height distribution

half-height (mm)

(b) optimal half-height distribution

Figure 4.12: Die cavity half-height distribution

4.6 Summary

A hybrid numerical scheme is employed in which the pressure solution of 2.5D Hele-Shaw flow is fully coupled with a non-linear 3D energy equation for the calculation of temperature. The analysis based on 2.5D Hele-Shaw flow evaluates the pressure distribution in the polymer melt which is used to calculate the velocity field. We then substitute the pressure and velocity solutions in to the 3D energy equation to compute the melt temperature. The solution of fully coupled nonlinear steady-state temperature and pressure systems is solved with the Newton-Raphson iteration method. Analytical sensitivities are formulated with the adjoint variable method. The analysis and sensitivity analysis are finally combined with numerical optimization to form an optimum design algorithm. Examples are given in this chapter that integrate the fully-coupled nonlinear steady-state pressure and temperature system with numerical optimization to compute a die cavity geometry capable of giving a nearly uniform exit flow velocity and temperature.

CHAPTER 5

CONCLUSIONS AND RECOMMENDATIONS

There is a great diversity among modern industries associated with polymer processing. The major processes for polymer processing can be categorized as follows: extrusion, postdie processing, forming, and injection molding. Primarily, these processes deal with the conversion of raw polymeric materials into finished products. As justified by Tadmor and Gogos [3], polymer processing is defined as the "engineering activity concerned with operations carried out on polymeric materials or systems to increase their utility". Indeed, polymers and plastic materials are becoming increasingly important due to their versatile property portfolio, performance and their suitability for functionalization with special effects.

The modeling of polymer processing operations requires an accurate quantitative understanding of material properties and behavior. In general, fluid dynamics, heat transfer, mechanics and polymer science are necessary for the successful design, operation, control, and analysis of these processes. Additionally, polymer processing simulation is often complicated and involves complex constitutive models in nonlinear coupled fluid flow analyses. The complexity of current polymer processing renders traditional design approaches inefficient and inadequate, and opens a door for the development of more advanced design methods.

This research presents design sensitivity analysis method with numerical simulation in polymer manufacturing processes. The major accomplishments of this research

are in polymer processing simulation, design sensitivity analysis, and numerical optimization as well as the integration of these to develop a design methodology for polymer processing. The main contribution of this research follows:

- This research presents an efficient method for the design of polymer sheeting dies based on the integration of finite element flow simulations, sensitivity analysis, and optimization. Simulations that are employed in the optimal design process are based on the generalized Hele-Shaw flow model to provide a means for including die cavity geometries with arbitrary in-plane features without the computational burden characteristic of more complex three-dimensional simulations.

- This research extends earlier optimization-based approaches to include various GNF models, such as the power-law, Carreau-Yasuda, Cross, Ellis, and Bingham, in the analyses and sensitivity analyses required for the optimization calculations. A viscosity derivative factor (see e.g., tables 2.1 and 2.2) is derived which facilitates both the Newton-Raphson iteration procedure and design sensitivity optimization.

- This research presents an polymer extrusion design problem and solution procedure that may be used for materials processing design problems where adjustable parameters are employed to accommodate manufacturing variations. The proposed approach is to determine a single sheeting die cavity geometry that will best accommodate multiple operating conditions that may exist due

to variations in temperature, material, and/or flow rate.

- This research is a first step in integrating a simulation of the polymer melt flow and die cavity deformation with numerical optimization in the polymer manufacturing processes. Both the polymer melt flow and sheeting die deformation are analyzed with a general purpose finite element package ABAQUS. The approach includes a user-defined element to evaluate the purely viscous non-Newtonian flow in a flat die. The flow analysis based on Hele-Shaw approximation is coupled to a three-dimensional finite element simulation for die deformation. In addition, shape optimization of a polymer sheeting die is performed by the incorporation of the coupled fluid-structure analyses in a constrained optimization algorithm. This fluid-structure interaction algorithm provides a powerful and convenient computational aid to the design engineers to analyze the deflecting dies.

- This research enhances the current design methodology by including the most realistic temperature dependent constitutive model in the design problem, and incorporating the generalized Hele-Shaw flow approximation for an inelastic, non-Newtonian fluid under non-isothermal conditions. A hybrid numerical algorithm is employed in which the pressure solution of 2.5D Hele-Shaw model is fully coupled with a non-linear 3D energy equation for the calculation of temperature. The Newton-Raphson iteration is used in the solution process so

that analytical design sensitivity formulation is efficiently derived via the adjoint method. Analysis and sensitivity analysis of this fully coupled system are combined with numerical optimization to form an optimum design algorithm.

- Design sensitivities are evaluated using the streamline-upwind Petrov-Galerkin (SUPG) finite element method where special emphasis is given to the SUPG design dependent weighting functions.

- Examples in sheeting die design exemplify the design methodology. Sheeting dies are designed to form the optimal flow channel geometry, reduce pressure drop and generate a uniform exit velocity and exit temperature.

In the extrusion thermal analysis, the current research only considers the constant wall temperature as the thermal boundary condition. Addition research would enhance the current design methodology by considering the thermal interaction between the melt and the die body, e.g., the boundary condition representing heat loss by convection and radiation.

The coupled fluid-structure interaction analysis in the chapter 3 employs the isothermal Carreau-Yasuda model to represent the polymer melt behavior in the design problem. Since polymer viscosities are temperature dependent, simulation results, and thus optimal designs, would be more accurate if we also included the non-isothermal analysis to perform fluid-structure interaction analysis, and to evaluate the die body deformation.

Sensitivity analysis and optimization should also be applied to design short-fiber

composite products and their manufacturing process. Here, the manufacturing process determines the orientation of the fiber suspension which defines the product strength, stiffness and thermal expansion coefficient distributions [9]. A numerical optimization to design these products would include a flow simulation, a structural analysis, and a fully-coupled sensitivity analysis similar to that developed in this research. Since the rheological property of polymeric composites is frequently based on the viscous behavior of rigid particles dispersed in a Newtonian fluid, the art of mathematical modeling of constitutive equations proposed in this research may be utilized to represent the rheological response of polymeric composites.

In the current research, analysis and sensitivity analysis capabilities are combined with numerical optimization to form an optimum design algorithm. The Newton-Raphson iteration is used in the solution process so that analytical design sensitivity formulation may be derived via the adjoint variable method. The computation effort involved in these processes is very large, both in terms of the calculation time and CPU time. Therefore, efficient methods are needed to evaluate the sensitivity and design optimization. Additionally, as larger models are optimized, more efficient filling algorithms, possibly those using implicit time integration, should be developed for the analysis and the sensitivity analysis. Finally, interfacing with commercial analysis codes and industrial die models are encouraged so that the optimization method presented in this research is more applicable to actual material processing applications.

APPENDIX A

CHARACTERISTIC ELEMENT LENGTH

The characteristic element length d_e, as shown in equation 4.17, is calculated along the velocity or advection direction [84] (i.e., along $\mathbf{v}$). Obtaining d_e for one-dimensional elements is straightforward, however, derivation of d_e for two- and three-dimensional elements may involve complex computation. Furthermore, to evaluate $\frac{\partial \mathbf{R}^{\mathbf{T}}}{\partial \mathbf{P}}$ and $\frac{\partial \mathbf{R}^{\mathbf{T}}}{\partial \phi}$, d_e must be differentiated with respect to the design and the pressure field, respectively (cf. equations 4.71 and 4.75). Yu and Heinrich [85] proposed a simple algorithm to calculate a characteristic element length and added perturbed shifting functions in the weighted residuals formulation. This algorithm was later used by Swaminathan and Voller [79]. The resulting value for d_e, however, does not produce the element length along the velocity direction for an arbitrary $\mathbf{v}$.

To evaluate d_e for an element with domain $\overset{e}{D}$, we use the isoparametric finite element mapping $\overset{e}{\chi}$ to relate the body configuration $\overset{e}{D}$ to the reference configuration $\overset{e}{D}_\kappa$ as shown in figure A.1. We evaluate d_e at the element centroid and at this location the velocity vector $\mathbf{v}$ in $\overset{e}{D}$ is treated as an infinitesimal quantity so that when it is projected onto the reference domain $\overset{e}{D}_\kappa$ it transforms to

$$\mathbf{v}_0 = \mathbf{J}^{-1}\,\mathbf{v} \tag{A.1}$$

where $\mathbf{J}$ is the Jacobian of the mapping $\overset{e}{\chi}$. The reference element length d_e in the direction of $\mathbf{v}_0$ is calculated at the element centroid and is straightforward to evaluate

133

since the reference domain $\overset{e}{D}_\kappa$ is a square defined over $-1 \leq \xi_1 \leq 1$ and $-1 \leq \xi_2 \leq 1$ where $\xi = \{\xi_1 \ \xi_2\}^T$. Finally, the stretch ratio $\frac{\|\mathbf{V}\|}{\|\mathbf{V}_0\|}$ transforms the reference element length in the direction of $\mathbf{v}_0$ to the body element length d_e in the direction of $\mathbf{v}$. Thus we define

$$d_e = \begin{cases} 2 \frac{\|\mathbf{V}\|}{\|\mathbf{V}_0\|} \sqrt{1 + \left(\frac{v_{02}}{v_{01}}\right)^2} & \text{if} \quad v_{02} \leq v_{01} \\ 2 \frac{\|\mathbf{V}\|}{\|\mathbf{V}_0\|} \sqrt{1 + \left(\frac{v_{01}}{v_{02}}\right)^2} & \text{if} \quad v_{01} \leq v_{02} \end{cases} \tag{A.2}$$

where $\mathbf{v}_0 = \{v_{01} \ v_{02}\}^T$.

The element length d_e is evaluated via equation A.2 for bilinear elements. However, the calculation may be performed for higher order elements, as well. Note that the value of d_e obtained via equation A.2 is exact for elements with a uniform Jacobian throughout the domain $\overset{e}{D}$, i.e., elements that are square, rectangular, or that form parallelograms. For square or rectangular elements, equation A.2 reduces to

$$d_e = \begin{cases} \frac{\|\mathbf{V}\|}{v_1} \Delta x_1 & \text{if} \quad v_2 \leq v_1 \\ \frac{\|\mathbf{V}\|}{v_2} \Delta x_2 & \text{if} \quad v_1 \leq v_2 \end{cases} \tag{A.3}$$

where Δx_1 and Δx_2 are the element lengths in the x_1 and x_2 directions, respectively, and $\mathbf{v} = \{v_1 \ v_2\}^T$.

In the design problem, we rewrite equation A.2 to emphasize the dependence of d_e on the pressure field $\mathbf{P}$ and the design ϕ as

$$d_e(\mathbf{P}(\phi), \phi) = \begin{cases} 2 \frac{\|\mathbf{v}(\mathbf{P}(\phi),\phi)\|}{\|\mathbf{v}_0(\mathbf{P}(\phi),\phi)\|} \sqrt{1 + \left(\frac{v_{02}(\mathbf{P}(\phi),\phi)}{v_{01}(\mathbf{P}(\phi),\phi)}\right)^2} & \text{if } v_{02}(\mathbf{P}(\phi), \phi) \leq v_{01}(\mathbf{P}(\phi), \phi) \\ 2 \frac{\|\mathbf{v}(\mathbf{P}(\phi),\phi)\|}{\|\mathbf{v}_0(\mathbf{P}(\phi),\phi)\|} \sqrt{1 + \left(\frac{v_{01}(\mathbf{P}(\phi),\phi)}{v_{02}(\mathbf{P}(\phi),\phi)}\right)^2} & \text{if } v_{01}(\mathbf{P}(\phi), \phi) \leq v_{02}(\mathbf{P}(\phi), \phi) \end{cases} \tag{A.4}$$

Similarly, we note the dependence of $\mathbf{v}_0$ on $\mathbf{P}$ and ϕ as

$$\mathbf{v}_0(\mathbf{P}(\phi), \phi) = \mathbf{J}^{-1}(\phi) \, \mathbf{v}(\mathbf{P}(\phi), \phi) \tag{A.5}$$
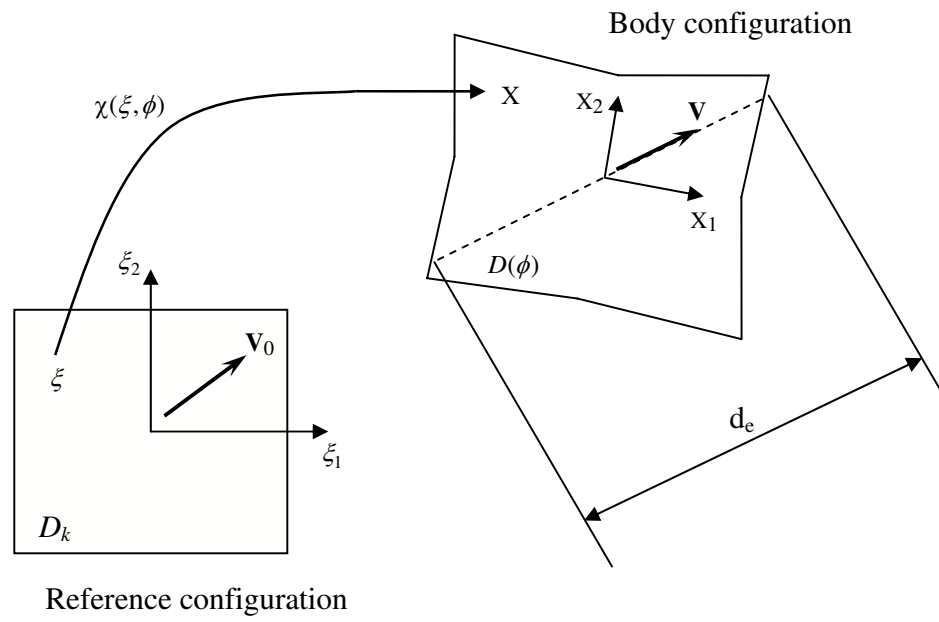
Figure A.1: Element characteristic length

We use the domain parameterization method of shape sensitivity analysis [50] to isolate the explicit dependence of $\mathbf{v}$ on the design $\boldsymbol{\phi}$ from the implicit dependence of $\mathbf{v}$ on $\boldsymbol{\phi}$ through the solution $\mathbf{P}$. Note that in equations A.1 and A.5 we have projected $\mathbf{v}$ from $\overset{e}{D}$ to $\overset{e}{D}_\kappa$ to facilitate the analysis given above and sensitivity analysis presented below.

The derivative $\frac{\partial d_e}{\partial \mathbf{T}}$ is required for the evaluation of $\frac{\partial \mathbf{R}^\mathbf{T}}{\partial \mathbf{T}}$ (cf. equation 4.29) and is defined such that $\frac{\partial d_e}{\partial T}[\triangle T] \approx \frac{\partial d_e}{\partial \mathbf{T}}\triangle \mathbf{T}$ as

$$\frac{\partial d_e}{\partial \mathbf{T}} = d_e \left(\frac{1}{\|\mathbf{v}\|}\frac{\partial \|\mathbf{v}\|}{\partial \mathbf{T}} - \frac{1}{\|\mathbf{v}_0\|}\frac{\partial \|\mathbf{v}_0\|}{\partial \mathbf{T}} + \left(\frac{v_{02}}{v_{01}}\right)\frac{\frac{1}{v_{01}}\frac{\partial v_{02}}{\partial \mathbf{T}} - \frac{v_{02}}{v_{01}^2}\frac{\partial v_{01}}{\partial \mathbf{T}}}{1 + \left(\frac{v_{02}}{v_{01}}\right)^2} \right) \tag{A.6}$$

Note that the above derivation for $\frac{\partial d_e}{\partial \mathbf{T}}$ is valid when $v_{02} \leq v_{01}$. The derivation for $v_{01} \leq v_{02}$ is similar and is not presented here for conciseness. The derivative $\frac{\partial \|\mathbf{V}\|}{\partial \mathbf{T}}$ and $\frac{\partial \|\mathbf{V}_0\|}{\partial \mathbf{T}}$ are computed from

$$\frac{\partial \|\mathbf{v}\|}{\partial \mathbf{T}} = \frac{b}{\|\mathbf{v}\|}\frac{\partial b}{\partial \mathbf{T}}\|\boldsymbol{\nabla}P\|^2 \tag{A.7}$$

and

$$\frac{\partial \|\mathbf{v}_0\|}{\partial \mathbf{T}} = \frac{\|\mathbf{v}_0\|}{b}\frac{\partial b}{\partial \mathbf{T}} \tag{A.8}$$

where

$$b = -\int_z^h \frac{z}{\eta}\,dz \tag{A.9}$$

The $\frac{\partial d_e}{\partial \mathbf{T}}$ derivation contains the derivatives $\frac{\partial \mathbf{V}}{\partial \mathbf{T}}$ and $\frac{\partial \mathbf{V}_0}{\partial \mathbf{T}}$. The former derivative is defined such that $\frac{\partial \mathbf{V}}{\partial T}[\triangle T] \approx \frac{\partial \mathbf{V}}{\partial \mathbf{T}}\triangle \mathbf{T}$ which is obtained by differentiating equation 2.9 with respect to $\mathbf{T}$ and from equation A.1

$$\frac{\partial \mathbf{v}_0}{\partial \mathbf{T}} = \mathbf{J}^{-1}\frac{\partial \mathbf{v}}{\partial \mathbf{T}} \tag{A.10}$$

136

Similarly, the derivative $\frac{\partial d_e}{\partial \mathbf{P}}$ is required for the evaluation of $\frac{\partial \mathbf{R}^\mathbf{T}}{\partial \mathbf{P}}$ (cf. equation 4.71) and is defined such that $\frac{\partial d_e}{\partial P}[\triangle P] \approx \frac{\partial d_e}{\partial \mathbf{P}}\triangle \mathbf{P}$ as

$$\frac{\partial d_e}{\partial \mathbf{P}} = d_e \left(\frac{1}{\|\mathbf{v}\|} \frac{\partial \|\mathbf{v}\|}{\partial \mathbf{P}} - \frac{1}{\|\mathbf{v_0}\|} \frac{\partial \|\mathbf{v_0}\|}{\partial \mathbf{P}} + \left(\frac{v_{02}}{v_{01}} \right) \frac{\frac{1}{v_{01}} \frac{\partial v_{02}}{\partial \mathbf{P}} - \frac{v_{02}}{v_{01}^2} \frac{\partial v_{01}}{\partial \mathbf{P}}}{1 + \left(\frac{v_{02}}{v_{01}} \right)^2} \right) \tag{A.11}$$

Note that the above derivation for $\frac{\partial d_e}{\partial \mathbf{P}}$ is valid when $v_{02} \leq v_{01}$. The derivation for $v_{01} \leq v_{02}$ is similar and is not presented here for conciseness. The derivative $\frac{\partial \|\mathbf{V}\|}{\partial \mathbf{P}}$ and $\frac{\partial \|\mathbf{V_0}\|}{\partial \mathbf{P}}$ are computed from

$$\frac{\partial \|\mathbf{v}\|}{\partial \mathbf{P}} = \frac{1}{\|\mathbf{v}\|} \left(b \frac{\partial b}{\partial \mathbf{P}} \|\boldsymbol{\nabla}P\|^2 + b^2 \boldsymbol{\nabla}P \cdot \boldsymbol{\nabla}\triangle P \right) \tag{A.12}$$

and

$$\frac{\partial \|\mathbf{v_0}\|}{\partial \mathbf{P}} = \frac{1}{b} \frac{\partial b}{\partial \mathbf{P}} \|\mathbf{v_0}\| + \frac{b}{\|\mathbf{v_0}\|} \mathbf{v_0} \, \mathbf{J}^{-1} \boldsymbol{\nabla}\triangle P \tag{A.13}$$

The $\frac{\partial d_e}{\partial \mathbf{P}}$ derivation contains the derivatives $\frac{\partial \mathbf{V}}{\partial \mathbf{P}}$ and $\frac{\partial \mathbf{V_0}}{\partial \mathbf{P}}$ (cf. equation A.4). The former derivative is defined such that $\frac{\partial \mathbf{V}}{\partial P}[\triangle P] \approx \frac{\partial \mathbf{V}}{\partial \mathbf{P}}\triangle \mathbf{P}$ which is obtained by differentiating equation 2.9 with respect to $\mathbf{P}$ and from equation A.1

$$\frac{\partial \mathbf{v_0}}{\partial \mathbf{P}} = \mathbf{J}^{-1} \frac{\partial \mathbf{v}}{\partial \mathbf{P}} \tag{A.14}$$

Finally, to obtain $\frac{\partial d_e}{\partial \phi_i}$ and thus $\frac{\partial \mathbf{R}^\mathbf{T}}{\partial \phi_i}$ (cf. equation 4.75), we differentiate equation A.4 with respect to ϕ_i as

$$\frac{\partial d_e}{\partial \phi_i} = d_e \left(\frac{1}{\|\mathbf{v}\|} \frac{\partial \|\mathbf{v}\|}{\partial \phi_i} - \frac{1}{\|\mathbf{v_0}\|} \frac{\partial \|\mathbf{v_0}\|}{\partial \phi_i} + \left(\frac{v_{02}}{v_{01}} \right) \frac{\frac{1}{v_{01}} \frac{\partial v_{02}}{\partial \phi_i} - \frac{v_{02}}{v_{01}^2} \frac{\partial v_{01}}{\partial \phi_i}}{1 + \left(\frac{v_{02}}{v_{01}} \right)^2} \right) \tag{A.15}$$

The above expression of $\frac{\partial d_e}{\partial \phi_i}$ applies to $v_{02} \leq v_{01}$. The derivation for $v_{01} \leq v_{02}$ can be obtained in a similar way. The resulting derivative of $\frac{\partial d_e}{\partial \phi_i}$ requires the evaluation

of $\frac{\partial \mathbf{v}}{\partial \phi_i}$ and $\frac{\partial \mathbf{v}_0}{\partial \phi_i}$. To evaluate $\frac{\partial \mathbf{v}}{\partial \phi_i}$ we differentiate $\mathbf{v}$ with respect to the design variable

ϕ_i and to compute $\frac{\partial \mathbf{v}_0}{\partial \phi_i}$ we differentiate equation A.5 with respect to ϕ_i, i.e.,

$$\frac{\partial \mathbf{v}_0}{\partial \phi_i} = \frac{\partial \mathbf{J}^{-1}}{\partial \phi_i} \mathbf{v} + \mathbf{J}^{-1} \frac{\partial \mathbf{v}}{\partial \phi_i} \tag{A.16}$$

where we note that $\mathbf{v}_0$ depends on the element shape through $\mathbf{J}$ and on the velocity

$\mathbf{v}$, which is an explicit function of design.

BIBLIOGRAPHY

[1] Szarvasy, I., J. Sienz, J.F.T. Pittman, and E. Hinton. Computer Aided Optimisation of Profile Extrusion Dies. *International Polymer Processing*, 2000:28–39, 2000.

[2] Nobrega, J., F. Pinho, P. Oliveria, and Carneiro O. Sensitivity of Flow Distribution and Flow Patterns in Profile Extrusion Dies. In *ANTEC 2003, Society of Plastics Engineers*, volume 49, Nashville, TN, 2003.

[3] Tadmor, Z. and C.G. Gogos. *Principles of Polymer Processing*. John Wiley and sons, Inc., New York, N.Y., 1979.

[4] Smith, D.E. and Qi Wang. An Optimization-Based Approach to Compute Sheeting Die Designs for Multiple Operation Conditions. In *45th AIAA/ASME/ASCE/AHS/ASC Structures, Structural Dynamics and Materials Conference*, Palm Springs, CA, 2004.

[5] Smith, D.E. and Q. Wang. Optimization-Based Design of Polymer Sheeting Dies Using Generalized Newtonian Fluid Models. *Polymer Engineering and Science*, 45(7):953–965, July 2005.

[6] Smith, D.E. and Qi Wang. Incorporating Adjustable Features in the Optimal Design of Polymer Sheet Extrusion Dies. *ASME Journal of Manufacturing Science and Engineering*, 128(1):11–19, 2006.

[7] Wang, Q. and D.E. Smith. Analysis of the Fluid-Structure Interaction in the Optimization-Based Design of Polymer Sheeting Dies. *Journal of Applied Polymer Science*, 103:3994–4004, 2007.

[8] Pittman, J.F.T. and R. Sander. Thermal Effects in Extrusion: Slit Dies. *International Polymer Processing*, 9(4):326–345, 1994.

[9] Smith, D.E. *Optimal Design and Analysis for Polymer Extrusion and Molding*. PhD thesis, University of Illinois at Urbana-Champaign, 1996.

[10] Chung, C. I. and D.T. Lohkamp. Designing Coat-Hanger Dies by Power-Law Approximation. *Modern Plastics*, pages 52–55, March 1976.

[11] Winter, H.H. and H.G. Fritz. Design of Dies for the Extrusion of Sheets and Annular Parisons: The Distribution Problem. *Polymer Engineering and Science*, 26:543–553, 1986.

[12] Liu, T.J., L.D. Liu, and J.D. Tsou. A Unified Lubrication Approach for the Design of a Coat-Hanger Die. *Polymer Engineering and Science*, 34(7):541–550, April 1994.

[13] Pan, J.P., P.Y. Wu, and T.J. Liu. Extrusion Die Design for Slowly Reacting Materials. *Polymer Engineering and Science*, 37(5):856–867, May 1997.

[14] Michaeli, W. *Extrusion Dies, Design and Engineering Computations*. Hanser Publishers, Munich, Germany, 1984.

[15] Wang, Y. The Flow Distribution of Molten Polymers in Slit Dies and Coathanger Dies Through Three-Dimensional Finite Element Analysis. *Polymer Engineering and Science*, 31(3):204–212, 1991.

[16] Huang, Y., C.R. Gentle, and J.B. Hull. A Comprehensive 3-D Analysis of Polymer Melt Flow in Slit Extrusion Dies. *Advances in Polymer Technology*, 23:111–124, 2004.

[17] Wen, S.H. and T.J. Liu. Extrusion Dies Design for Multiple Stripes. *Polymer Engineering and Science*, 35(9):759–767, 1995.

[18] Lo, S.W. An Efficient Method of Designing Controlled Strain Rate Dies for Extrusions. *Journal of the Chinese Institute of Engineers*, 19(5):623–631, 1996.

[19] Ilinca, F., A. Derdouri, and Hétu, J.F. Numerical Simulation and Experimental Validation of the Filling Stage in the Co-Injection Molding Process. In *ANTEC 2003, Society of Plastics Engineers*, Nashville, TN, 2003.

[20] Chang, R.Y., H.C. Hsu, C.S. Ke, and C.C. Hsu. Cluster Computing in Numerical Simulation of Extrusion Flow. In *ANTEC 2003, Society of Plastics Engineers*, Nashville, TN, 2003.

[21] Hieber, C.A. and S.F. Shen. A Finite-Element/Finite-Difference Simulation of the Injection-Molding Filling Process. *Journal of Non-Newtonian Fluid Mechanics*, 7:1–32, 1980.

[22] Smith, D.E., D.A. Tortorelli, and C.L. Tucker. Optimal Design for Polymer Extrusion. Part I: Sensitivity Analysis for Nonlinear Steady-State Systems. *Computer Methods in Applied Mechanics and Engineering*, 167(3-4):283–302, 1998.

[23] Dooley, J. Simulating the Flow in a Film Die Using Finite Element Analysis. In *ANTEC 1990, Society of Plastics Engineers*, volume 36, Dallas, TX, 1990.

[24] Gifford, W.A. A Three-Dimensional Analysis of Coextrusion in a Single Manifold Flat Die. *Polymer Engineering and Science*, 40(19):2095–2100, 2000.

[25] Gifford, W.A. The Effect of Wall Slip on the Performance of Flat Extrusion Dies. *Polymer Engineering and Science*, 41(11):1886–1892, 2001.

[26] Bird, R.B., R.C. Armstrong, and O. Hassager. *Dynamics of Polymeric Liquids*. John Wiley and Sons, Inc., New York, 1987.

[27] Gifford, W.A. Compensating for Die Swell in the Design of Profile Dies. *Polymer Engineering and Science*, 43(10):1657–1665, 2003.

[28] Arpin, B., P.G. Lafleur, and B. Vergnes. Simulation of Polymer Flow Through a Coat-Hanger Die: A Comparison of Two Numerical Approaches. *Polymer Engineering and Science*, 32(3):206–212, 1992.

[29] Zabaras, N., Y. Bao, A. Srikanth, and W.G. Frazier. A Continuum Lagrangian Sensitivity Analysis for Metal Forming Processes with Applications to Die Design Problems. *International Journal for Numerical Methods in Engineering*, 48:679–720, 2000.

[30] Ulysse, P. Extrusion Die Design for Flow Balance Using FE and Optimization Methods. *International Journal of Mechanical Sciences*, 44(2002):319–341, 2002.

[31] Maniatty, A.M. and M.F. Chen. Shape Sensitivity Analysis for Steady Metal-Forming Process. *International Journal for Numerical Methods in Engineering*, 39:1199–1217, 1996.

[32] Mihelič, A. and Štok, B. Tool Design Optimization in Extrusion Processes. *Computers and Structures*, 68:283–293, 1998.

[33] Legat, V. and J.M. Marchal. Die Design: An Implicit Formulation for the Inverse Problem. *International Journal for Numerical Methods in Fluids*, 16:29–42, 1993.

[34] Zhao, G., E. Wright, and R.V. Grandhi. Sensitivity Analysis Based Preform Die Shape Design for Net-Shape Forging. *International Journal of Machine Tools and Manufacture*, 37(9):1251–1271, 1997.

[35] Haftka, R.T. and Gürdal, Z. *Elements of Structural Optimization*. Kluwer Academic Publishers, 3300 AA Dordrecht, The Netherlands, 1991.

[36] Nobrega, J., O.S. Carneiro, F.T. Pinho, and P.J. Oliveria. Optimisation of the Flow Distribution in Profile Extrusion Dies. In *ANTEC 2002, Society of Plastics Engineers*, volume 48, San Francisco, CA, 2002.

[37] Na, S.Y. and T.Y. Lee. Shape Optimization of Polymer Extrusion Die By Three-Dimensional Flow Simulation. In *IEEE 1997*, pages 601–604, 1997.

[38] Wang, Y. Optimal Extrusion Die Design in Polymer Processing. In *Simulation of Materials Processing: Theory, Method adn Applications* , 1998.

[39] Sartor, L. *Slot Coating: Fluid Mechanics and Die Design*. PhD thesis, University of Minnesota, 1990.

[40] Smith, D.E., D.A. Tortorelli, and C.L. Tucker. Optimal Design of Polymer Sheeting Dies. In *ANTEC 1995, Society of Plastics Engineers*, Boston, MA, 1995.

[41] Smith, D.E. An Optimization-Based Approach to Compute Sheeting Die Designs for Multiple Operating Conditions. In *ANTEC 2003, Society of Plastics Engineers*, Nashville, TN, 2003.

[42] Kennedy, P. *Flow Analysis of Injection Molds*. Hanser Publishers, New York, 1995.

[43] Gifford, W.A. The Use of Three-Dimensional Computational Fluid Dynamics in the Design of Extrusion Dies. *Journal of Reinforced Plastics and Composites*, 16:661–674, 1997.

[44] Arpin, B., P.G. Lafleur, and B. Sanschagrin. A Personal Computer Software for Coathanger Die Simulation. *Polymer Engineering and Science*, 34(8):657–664, 1994.

[45] Sander, R. and J.F.T. Pittman. Simulation of Slit Dies in Operation Including the Interaction Between Melt Pressure and Die Deflection. *Polymer Engineering and Science*, 36(15):1972–1989, 1996.

[46] Gifford, W.A. A Three-Dimensional Analysis of the Effect of Die Body Deflection in the Design of Extrusion Dies. *Polymer Engineering and Science*, 38(10):1729–1739, 1998.

[47] Wang, Q. and D.E. Smith. Incorporate Fluid-Structure Interaction in the Analysis of Polymer Sheeting Dies. In *ANTEC 2006, Society of Plastics Engineers*, pages 872–876, Charlotte, North Carolina, 2006.

[48] Wang, Q. and D.E. Smith. Incorporating Fluid-Structure Interaction in the Optimization-Based Design of Polymer Sheeting Dies. In *11th AIAA/ISSMO Multidisciplinary Analysis and Optimization Conference*, Portsmouth, Virginia, 2006.

[49] Brooks, A.N. and J.R. Hughes. Streamline Upwind/Petrov-Galerkin Formulas for Convection Dominated Flows with Particular Emphasis on the Incompressible Navier-Stokes Equations. *Computer Methods in Applied Mechanics and Engineering*, 32:199–259, 1982.

[50] Tortorelli, D.A. Design Sensitivity Analysis for Coupled Systems and Their Application to Concurrent Engineering. In *Concurrent Engineering: Tools and Technologies for Mechanical System Design*, pages 709–719. Springer, 1993.

[51] Wu, P.Y., T.J. Liu, and H.M. Chang. Design of an Extrusion Die With a Variable Choker Bar. *Journal of Applied Polymer Science*, 51:1005–1014, 1994.

[52] Bates, S.J., J.F.T. Pittman, J. Sienz, and D.S. Langley. Enhancing Slit Die Performance by Optimization of Restrictor Profiles. *Polymer Engineering and Science*, 43(8):1500–1511, 2003.

[53] Smith, D.E. Design Sensitivity Analysis and Optimization for Polymer Sheet Extrusion and Mold Filling Processes. *International Journal for Numerical Methods in Engineering*, 57:1381–1411, 2003.

[54] Huebner, K.H., D.L. Dewhirst, D.E. Smith, and T.G. Byrom. *The Finite Element Method for Engineers.* John Wiley and Sons, Inc., New York, 2001.

[55] Tucker III, C.L. *Computer Modeling for Polymer Processing.* Hanser Publishers, New York, NY, 1989.

[56] Arora, J.S. *Introduction to Optimum Design.* McGraw Hill, New York, 1989.

[57] Tortorelli, D.A. and P. Michaleris. Design Sensitivity Analysis: Overview and Review. *Inverse Problems in Science and Engineering*, (1):71–105, 1994.

[58] Haug, E.J., K.K. Choi, and V. Komkov. *Design Sensitivity Analysis of Structural Systems.* Academic Press, New York, 1986.

[59] Haber, R.B. Computer Aided Optimal Design: Structural and Mechanical Systems. In *NATO ASI Series*, volume F27, Berlin, Germany, 1987.

[60] Vanderplaats Research and Development, Inc., Colorado Springs, CO. *Design Optimization Tools Users Manual*, 1999.

[61] Helmy, H. Recent Developments in Flat Film and Sheet Dies. *Journal of Plastic Film and Sheeting*, 4:193–213, July 1987.

[62] Michaeli, W. *Extrusion Dies for Plastics and Rubber, 2nd Edition.* Hanser Publishers, New York, 1992.

[63] Hibbitt, Karlsson and Sorensen, Inc., Pawtucket, RI. *ABAQUS / Standard User's Manual*, 2002.

[64] Baird, D.G. and D.I. Collias. *Polymer Processing Principles and Design.* Butterworth-Heinemann, Newton, MA, 1995.

[65] Wang, Q. Incorporating Generalized Newtonian Fluids in Polymer Sheeting Die Design. Master's thesis, University of Missouri-Columbia, 2003.

[66] Vergnes, B., P. Saillard, and J.F. Agassant. Non-isothermal Flow of a Molten Polymer in a Coat-Hanger Die. *Polymer Engineering and Science*, 24(12):980–987, 1984.

[67] Ilinca, F., Hétu, J.F., and A. Derdouri. Metal Injection Molding: 3D Modeling of Nonisothermal Filling. *Polymer Engineering and Science*, 42(4):760–770, April 2002.

[68] Lee, G.A., D.Y. Kwak, S.Y. Kim, and Y.T. Im. Analysis and Design of Flat-Die Hot Extrusion Process 1. Three-Dimensional Finite Element Analysis. *International Journal of Mechanical Sciences*, 44:915–934, 2002.

[69] Haftka, R.T. Techniques for thermal sensitivity analysis. *International Journal for Numerical Methods in Engineering*, 17:71–80, 1981.

[70] Meric, R.A. Boundary Element Methods for Optimization of Distributed Parameter Systems. *International Journal for Numerical Methods in Engineering*, 20:1291–1306, 1984.

[71] Tortorelli, D.A. and R.B. Haber. First-Order Design Sensitivities for Transient Conduction Problems by An Adjoint Method. *International Journal for Numerical Methods in Engineering*, 28:733–752, 1989.

[72] Tortorelli, D.A., R.B. Haber, and S.C.-Y. Lu. Design Sensitivity Analysis for Nonlinear Thermal Systems. *Computer Methods in Applied Mechanics and Engineering*, 77:61–77, 1989.

[73] Dems, K. Sensitivity Analysis in Thermal Problems - I: Variation of Material Parameters with a Fixed Domain. *Journal of Thermal Stresses*, 9:303–324, 1986.

[74] Dems, K. Sensitivity Analysis in Thermal Problems - II: Structure Shape Variation. *Journal of Thermal Stresses*, 10:1–16, 1987.

[75] Tortorelli, D.A., M.M. Tiller, and J.A. Dantzig. Optimal Design of Nonlinear Parabolic Systems. Part I: Fixed Spatial Domains with Applications to Process Optimization. *Computer Methods in Applied Mechanics and Engineering*, 113:141–155, 1994.

[76] Smith, D.E., D.A. Tortorelli, and C.L. Tucker. Optimal Design for Polymer Extrusion. Part II: Sensitivity Analysis for Weakly-Coupled Nonlinear Steady-State Systems. *Computer Methods in Applied Mechanics and Engineering*, 167(3-4):303–323, 1998.

[77] Michaleris, P. Analysis and Optimization of Weakly Coupled Thermoelastoplastic Systems with Applications to Weldment Design. *International Journal for Numerical Methods in Engineering*, 38:1259–1285, 1995.

[78] Wang, Z.X., D.A. Tortorelli, and J.A. Dantzig. Sensitivity Analysis and Optimization of Coupled Thermal and Flow Problems with Applications to Contraction Design. *International Journal for Numerical Methods in Fluids*, 23:991–1020, 1996.

[79] Swaminathan, C.R. and V.R. Voller. Streamline Upwind Scheme for Control-volume Finite Elements, Part I: Formulation. *Numerical Heat Transfer*, 22:95–107, 1992.

[80] Swaminathan, C.R. and V.R. Voller. Streamline Upwind Scheme for Control-volume Finite Elements, Part II: Implementation and Comparison with the SUPG Finite Element Scheme. *Numerical Heat Transfer*, 22:109–124, 1992.

[81] Zienkiewicz, O.C. and R.L. Taylor. *The Finite Element Method, vloume 2.* McGraw-Hill, New York, NY, 1991.

[82] Griffiths, D.V. and I.M. Smith. *Numerical Methods for Engineers.* CRC Press, 1991.

[83] Wu, T., B. Jiang, S. Xu, and C. Bi. Nonisothermal Comprehensive 3D Analysis of Polymer Melt Flow in a Coat-Hanger Die. *Polymer Engineering and Science*, 46:406–415, 2006.

[84] Tezduyar, T.E. and D.K. Ganjoo. Petrov-Galerkin Formulations with Weighting Functions Dependent upon Spatial and Temporal Discretization: Applications to Transient Convection-Diffusion Problems. *Computer Methods in Applied Mechanics and Engineering*, 59:49–71, 1986.

[85] Yu, C.C. and J.C. Heinrich. Petrov-Galerkin Method for Multidimensional, Time-Dependent, Convective-Diffusion Equations. *International Journal for Numerical Methods in Engineering*, 24:2201–2215, 1987.

VITA

Qi Wang was born in January, 1977 in the city of Pingdingshan, China. He developed a genuine interest in engineering in high school, and chose Mechanical Engineering as his major at the Wuhan University of Technology, one of the best engineering schools in China. He earned his bachelors degree in Mechanical Engineering from the same university in June 1999. In summer 2001, Mr. Wang moved to the United States and pursued advanced education first at the Colorado School of Mines in Golden, Colorado, and later at the University of Missouri-Columbia. He received the degree of Master in Science from the University of Missouri-Columbia in August, 2003. The following fall, Mr. Wang started his doctoral program in the Department of Mechanical and Aerospace Engineering at the University of Missouri-Columbia. Mr. Wang is a member of the American Society of Plastics Engineers, the American Institute of Aeronautics and Astronautics, and the Sigma Xi Scientific Research Society. Mr. Wang also served as a journal reviewer for the Journal of Applied Polymer Science.